

**Low-Energy Electron Impact Fragmentations  
of the Polycyclic Aromatic Hydrocarbon  
Anthracene**

Melissa Anne Dunne

A thesis submitted for the degree of Masters of Science



Department of Experimental Physics  
National University of Ireland Maynooth  
Maynooth, Co. Kildare

October 2017

Head of Department  
Professor J. Anthony Murphy

Research Supervisor  
Dr. Peter J. M van der Burgt

# Contents

<b>Abstract</b> .....	<b>iii</b>
<b>Acknowledgements</b> .....	<b>iv</b>
<b>1 Introduction and Background</b>	
1.1 What are Polycyclic Aromatic Hydrocarbons?.....	1
1.2 Why research PAHs? .....	3
1.3 Collision Studies with Anthracene.....	6
1.3.1 Electron Impact Studies .....	6
1.3.2 Photon Impact Studies .....	8
1.3.3 Ion Impact Studies .....	9
1.4 Research at Maynooth.....	11
<b>2 Mass Spectrometry</b>	
2.1 Overview of Mass Spectrometry.....	12
2.2 Mass Spectrometry Using Mass Filters .....	15
2.2.1 Quadrupole Mass Filter.....	15
2.2.2 Magnetic Sector Mass Filter .....	17
2.3 Mass Spectrometry Using Traps .....	19
2.3.1 Quadrupole Ion Trap.....	19
2.3.2 Penning Ion Trap.....	21
2.4 Time-of-Flight Mass Spectrometry.....	22
2.4.1 Linear Time-of-Flight Mass Spectrometry .....	22
2.4.2 Reflectron Time-of-Flight Mass Spectrometry.....	25
2.5 Ionisation Techniques in Mass Spectrometry .....	28
2.5.1 Fast Atom Bombardment Ionisation .....	28
2.5.2 Matrix-Assisted Laser Desorption/Ionisation .....	30
2.5.3 Electrospray Ionisation.....	32
2.5.4 Electron Ionisation .....	33
<b>3 Instrumentation and Setup</b>	
3.1 Overview of the experiment.....	36
3.1.1 Vacuum System.....	37
3.1.2 Expansion Chamber .....	41
3.1.3 Interaction Chamber.....	42
3.1.4 Time-of-Flight Tube.....	43
3.1.5 Interlock System.....	45
3.2 The Electron Gun and Faraday Cup.....	46
3.3 The Microchannel Plate Detector.....	49

<b>4</b>	<b>Interfacing, Data Acquisition and Data Analysis</b>	
4.1	Introduction .....	52
4.2	Pulsing and Timing .....	52
4.3	Amplification and Discrimination of Detector Pulses .....	55
4.4	Multichannel Scaler .....	56
4.5	Data Acquisition Software .....	57
4.5.1	The Electron Gun .....	57
4.5.2	Acquiring Mass Spectra .....	57
4.5.3	Gaussian Peak Fitting Program .....	59
4.5.4	Appearance Energy Program .....	63
<b>5</b>	<b>Experimental Results</b>	
5.1	Introduction .....	65
5.2	Anthracene Mass Spectrum .....	65
5.3	Gaussian Peak Fitting and Ion Yield Curves .....	70
5.3.1	Groups 1 and 2 .....	70
5.3.2	Groups 3, 4 and 5 .....	72
5.3.3	Groups 6 and 7 .....	74
5.3.4	Groups 8, 9, 10 and 12 .....	76
5.3.5	Groups 11 and 13 .....	79
5.3.6	Group 14.....	84
5.4	Appearance Energies.....	85
<b>6</b>	<b>Conclusion.....</b>	<b>93</b>
	<b>References .....</b>	<b>94</b>
	<b>Appendix .....</b>	<b>107</b>



## Abstract

The aim of the study undertaken for this Masters of Science thesis was to investigate the fragmentation processes induced by low-energy electron impact with anthracene. This research is relevant in the study of low-energy electron interactions with molecules in gaseous environments, including potentially in the interstellar medium where secondary electrons may be produced by UV-irradiation of interstellar dust grains.

An effusive, molecular beam of anthracene, generated in a resistively heated oven, is crossed with a beam of low-energy electrons to form positively charged fragments. A reflectron time-of-flight mass spectrometer with a microchannel plate detector is used to mass-resolve and detect the fragment ions.

A multichannel scaler card is used for acquiring single mass spectra. Data acquisition is controlled by LabVIEW code, which ramps the electron impact energy from 0 to 100 eV in 0.5 eV steps, acquires mass spectra as a function of electron impact energy, and adds each mass spectrum to the data that has already been accumulated. The full data set consists of a two-dimensional array of ion yield as a function of time-of-flight and of electron impact energy. Ion yield curves of most of the fragment ions have been determined by fitting groups of adjacent peaks in the mass spectra with sequences of normalized Gaussians. This is done using in-house LabVIEW software. The appearance energies for these fragments have been determined.

The groups of fragments containing 8 to 13 carbon atoms provide evidence for hydrogen rearrangements during fragmentation, involving the retention or loss of one or two additional hydrogen atoms. Groups of fragments with 6 and 7 carbon atoms clearly show the presence of doubly-charged fragments. We see broadened peaks in the lower-mass groups with 1 to 4 carbon atoms, which may be due to energetic charge-separation fragmentations of doubly-charged anthracene.

## **Acknowledgements**

I wish to extend my sincerest gratitude to the staff and postgraduate students of the Department of Experimental Physics in N.U.I. Maynooth, whose helpful, open-door approach has been evident since the start of my undergraduate degree. I am particularly thankful to have had Dr. Peter van der Burgt as my supervisor. His consistent availability, patience, dedication and motivation have made this research my most enjoyable and valuable undertaking to date.

# 1 Introduction and Background

## 1.1 What are Polycyclic Aromatic Hydrocarbons?

Polycyclic aromatic hydrocarbons (PAHs) are stable organic compounds consisting entirely of hydrogen and carbon. They are composed of multiple aromatic rings, which incorporate  $\sigma$  bonds and delocalised  $\pi$  electrons between carbon atoms. The term 'aromatic' has come to define molecules that have a system of delocalised  $\pi$  electrons that yield molecular stability.

Benzene, molecular formula  $C_6H_6$ , is the hexagonal configuration of six carbon atoms, and as such is the simplest hydrocarbon. In regular PAHs of rings containing six carbon atoms, the carbon bonding involves  $sp^2$  atomic orbitals, resulting in a planar structure. The stability of benzene, and therefore PAHs, is partially caused by the delocalisation of  $\pi$  electrons, which occurs when electrons form hybrid orbitals that are more energetically desirable than their atomic orbitals. This concept is called orbital hybridisation and is used to explain the shift in orbital energy that occurs through the formation of bonds.

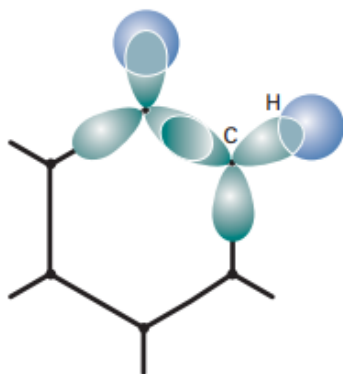


**Figure 1.1** An image depicting the C-C and C-H  $\sigma$  bond network in benzene. The  $\sigma$  framework is formed by the overlapping of  $sp^2$  hybrids [1].

The ground state electron configuration of carbon,  $1s^2 2s^2 2p^2$ , indicates that a carbon atom can only form two bonds, not four. This issue is revised by introducing the concept of orbital hybridisation, making it feasible for the 2s and 2p orbitals to combine by advancing a 2s electron to a 2p orbital. These electrons have mixed s-p wavefunctions. This is possible as the energy gap between these orbitals is quite small. Due to the spherical symmetry of the 2s orbital, it is the  $2p_x$  and the  $2p_y$  orbitals that dictate the direction of the hybridised orbital. The  $sp^2$  orbitals directions are separated by  $120^\circ$ , giving the benzene ring its planar shape [1].

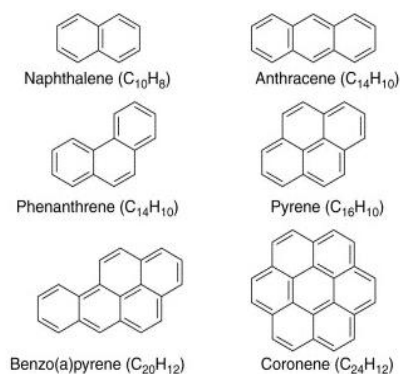


**Figure 1.2** The structure of some of the smallest PAHs [2].

The two 2p electrons in a carbon atom must occupy different orbitals, where the available orbitals are  $2p_x$ ,  $2p_y$ , and  $2p_z$ . The electrons occupy  $2p_x$  and  $2p_y$ , so the carbon configuration can be written as  $1s^2 2s^2 2p_x^1 2p_y^1$ . When introducing orbital hybridisation, one of the 2s electrons is promoted to the  $2p_z$  orbital, leading to a configuration of the form  $1s^2 2s^1 2p_x^1 2p_y^1 2p_z^1$ . This indicates that a carbon atom has four unpaired electrons in separate orbitals, and is capable of forming four bonds.

The electron in the  $2p_z$  orbital, however, is not used in forming a  $\sigma$  bond with the hybrid orbitals, and so the carbon atom can form three in-plane  $\sigma$  bonds with a hybrid of a neighbouring carbon atom or a hydrogen 1s electron. The six  $2p_z$  orbitals associated with benzene, one for each carbon atom present, form a  $\pi$  electron system in which bonds are created through the overlapping of orbital lobes and  $\pi$  electrons exist in molecular orbits that surround the whole ring. It seems that orbital hybridisation is a more energetically favourable condition for benzene as if it has 6 unhybridized electrons, only three double bonds could be formed, whereas delocalisation leads to equal bonding between all neighbouring carbon atoms, accommodating all  $2p_z$  electrons in  $1\pi$ ,  $2\pi$  and  $3\pi$  orbitals. This provides benzene, and thus PAHs, with their stability and aromaticity [1].

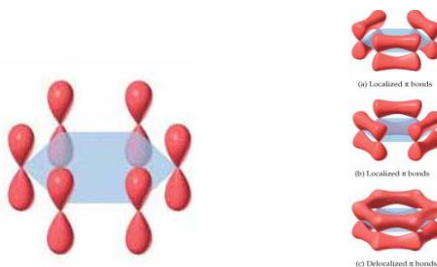


**Figure 1.3** Each carbon atom has an unhybridized 2p orbital that lies perpendicular to the molecular plane (left). These 2p orbitals can be used to make C-C localised  $\pi$  bonds. This can be done in two ways, shown in (a) and (b) (right). The smearing out, or delocalization, of the three  $\pi$  bonds can be seen in (c) (right) [3].

PAHs are mainly formed on Earth through pyrolytic processes such as the incomplete combustion of organic matter in the processing of coal and crude oil [4]. PAHs are considered to be abundantly present in the interstellar medium as the infrared spectra of almost all interstellar objects are dominated by strong, broad emission features characteristic of the vibrational modes of PAHs [5, 6].

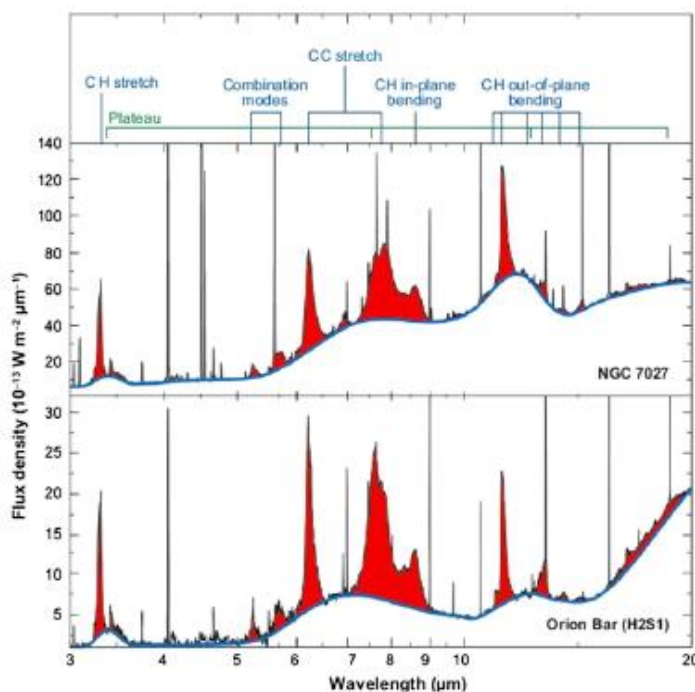


**Figure 1.4** The midinfrared spectra of the photodissociation region in the Orion bar and in the planetary nebula NGC 7027 with assignments of the vibrational modes of PAH molecules labelled at the top of the spectra [6].

In the laboratory, PAHs exist as yellow, white or colourless crystals with a faint and aromatic odour. They are usually solid at room temperature, highly hydrophobic, and very soluble in organic solvents. They have high melting and boiling points and low vapour pressures. Theoretically, the number of possible PAHs is very large but few have been synthesised in the laboratory, confining most of the research into PAHs to the smaller ring systems [4].

## 1.2 Why research PAHs?

PAHs are very prevalent in our terrestrial environment due to their production in industry, through the burning of industrial and municipal waste, and through smoking, among other sources. PAHs exhibit various levels of toxicity and due to their stability, they can build

up and remain in environments for a long time. This prevalence has led to much research into the environmental and carcinogenic effects of these compounds [7 – 13].

However, in Maynooth, our curiosity to study PAHs is guided by their abundance in the interstellar medium, and by the essential role that they play in explanations of the interstellar infrared emission bands [14, 15]. Research directed at how and where PAHs can form and combine can lead us to better understand elements of star formation and the factors that guide the production of organic molecules, and some essential elements of the basic molecules for life, in space. Carbon, the main constituent of PAHs, is the fourth most abundant element in the universe by mass, and forms many diverse organic compounds. PAHs and PAH derivatives are generated in the outflows of carbon and hydrogen rich stars and can be seen in many different environments in space, in meteorites, and in asteroidal and cometary dust [16]. PAHs that have lost hydrogen atoms become more reactive and are more likely to capture carbon atoms during collisions. These conditions encourage hydrocarbon growth, and analysis of interstellar PAHs indicates that they make up approximately 20% of all cosmically available carbon [17], and are the most complex molecules identified in space.

Due to their relatively non-volatile nature, it is expected that PAHs in the interstellar medium freeze out into ices where they form ice layers on the surface of dust grains in dense interstellar clouds. When these ices are exposed to high energy radiation, they undergo reactions which can cause the generation of a variety of compounds. If the PAHs are contained within water ices and then interact with charged particles or UV photons, oxygen-addition reactions can lead to the formation of aromatic ethers, alcohols and ketones, which are found in carbon rich meteorites. Aromatic ketones are of astrobiological interest as they contain a class of compounds known as quinones, which are known to play essential roles in many biochemical reactions in living organisms on Earth [17].

Many celestial objects have specific infrared emission features, and the collective term for these features is the unidentified infrared emission bands, or UIR bands. Duley and Williams proposed in 1981 [14] that some of the emission bands detected in the interstellar medium occurred at frequencies characteristic of different vibrational modes of large PAH molecules. It is now thought that large, partially hydrogenated PAH cations are the carriers of the UIR bands.  $H_n$ -PAHs, PAH molecules that carry an excess hydrogen atom on at least one of their carbon atoms, can also be produced in the outflows of carbon

rich stars, or when regular PAHs that are frozen into ices containing other hydrogen atoms are irradiated [18].

Though normally bonded PAHs have a planar structure, the addition of excess hydrogen to a carbon atom converts the atom to  $sp^3$  tetrahedral bonding, resulting in deformation of the molecule. This deformation causes the molecule to produce an infrared spectrum that indicates a combination of aromatic and aliphatic bonding. Infrared spectra taken for various regions of the interstellar medium indicate anharmonicity, implying the source of the emission is highly vibrationally excited; a state in which PAHs are found to be very stable. This excitation is caused by the absorption of UV photons which distribute energy throughout the molecules, resulting in the vibration of their constituent atoms and thus molecular distortions [15]. After excitation, the PAH molecule quickly relaxes back to its non-vibrating state by converting this vibrational energy into infrared energy. In this process, one UV photon has been transformed into many infrared photons, making PAHs very distinguishable in the interstellar medium due to their IR emission.

The spectra contain strong, broad emission features accompanied by many weaker bands perched on a broad plateau with a continuum sharply rising towards longer wavelengths; spectral features characteristic of PAHs. Due to this, PAH molecules can be used to trace important processes in the interstellar medium by observing their rotational and vibrational transitions through rotational-vibrational spectroscopy [19].

The presence of the UIR bands in a variety of objects suggests a ubiquitous presence of PAHs in the interstellar medium. The abundance of interstellar PAHs is calculated to be  $2 \times 10^{-7}$  with respect to hydrogen [15]. Due to their abundance, PAHs dominate the temperature and charge balances of the interstellar medium [20] and contribute to star formation by catalysing the formation of  $H_2$  [21]. The influence PAHs have over the conditions of various environments in the interstellar medium makes for a very interesting area of research.

The topic of this thesis is the fragmentation of anthracene via low-energy electron impact. Anthracene is a tricyclic PAH of molecular formula  $C_{14}H_{10}$ . It was identified in the interstellar medium by the University of Texas and the Instituto Astrofísica de Canarias (IAC) in 2010 [22] in the direction of Cernis 52 in the constellation Perseus. The irradiation of ice on interstellar dust grains by UV light and cosmic rays causes chemical reactions that lead to the formation of many molecular species. This irradiation also leads

to the release of many secondary electrons that induce further reactions [23] which lead to the creation of complex molecules such as anthracene. Section 1.3 will outline collision studies that have been conducted using anthracene.

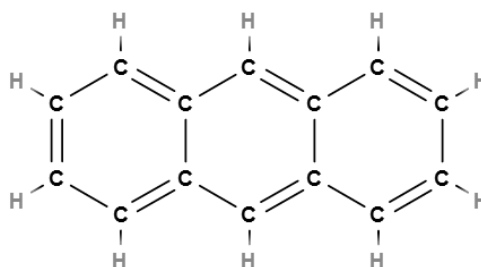


**Figure 1.5** The structure of anthracene [24].

## 1.3 Collision Studies with Anthracene

### 1.3.1 Electron Impact Studies

An electron impact study of anthracene was performed by Wacks and Dibeler in 1959 [25], where they measured a mass spectrum for anthracene and the appearance potentials of the singly and doubly charged anthracene molecule. Spectra of anthracene had not been published prior to their paper. They stated that with anthracene, about 45% of the total ionisation is attributable to the parent ion and 20% to the multiply charged ions. Table 1.1 shows their mass spectrum for anthracene.

$m/e$	OOO	$m/e$	OOO
36	...	86	1.8
37	...	87	3.1
37.5	...	87.5	1.1
38	0.7	88	9.4
38.5	...	88.5	2.0
39	3.9	89	15.6
		98	1.8
49	...	99	1.9
50	4.2	100	1.8
51	3.5	101	2.5
52	0.9	102	1.0
		125	0.7
		126	1.9
61	1.2	127	0.9
62	3.3	128	1.2
63	5.5	129	...
63.5	...		
64	0.6	139	1.4
64.5	...		
		149	1.2
		150	4.8
		151	7.4
73	...	152	7.6
74	2.8	153	1.0
74.5	...		
75	4.9	174	1.4
75.5	0.9	175	2.6
76	13.2	176	14.8
76.5	1.5	177	6.0
77	1.6	178	100.0
78	0.5	179	14.5
79	...	180	1.2

**Table 1.1** The mass spectrum of anthracene at 70 eV from Wacks and Dibeler [25].

They obtained the first and second ionisation potentials for benzene, naphthalene, anthracene and phenanthrene. Tables 1.2 displays their values.

Compound	a	Electron impact			Calculated	
		Compound	a	Present work	Group equiv.	SCF Reference 26
Benzene	9.3 <sub>4</sub>	Benzene	27.0	26.4	25.3	26.77
Naphthalene	8.2 <sub>6</sub>	Naphthalene	...	22.7	22.7	22.91
Anthracene	7.5 <sub>5</sub>	Anthracene	...	21.1	20.4	20.73
Phenanthrene	8.0 <sub>3</sub>	Phenanthrene	...	23.1	21.5	22.23

**Table 1.2** The first ionisation potentials (left) of the four simplest PAHs, including anthracene, and their second ionisation potentials (right) [25].

In 1964, Kuroda [26] determined the ionisation energy of anthracene from charge-transfer spectra. The value obtained was 7.42 eV.

In 1968, Dougherty and Weisenberger obtained a negative ion mass spectrum for anthracene [27], as shown in Table 1.3.

Relative intensity	
m/e	Anthracene <sup>d</sup>
12	11.0
24	17.0
25	20.5
26	100.0
27	2.0
36	3.6
48	2.2
49	6.6
50	7.3
60	0.1
61	0.5
62	0.4
66	0.9
72	4.7
73	0.6
74	2.0
79	
84	0.6
96	2.0
97	1.8
121	0.9
127	2.3
128	2.8
129	0.7
145	1.4
177	1.0
178	3.5
179	2.4
180	1.0

**Table 1.3** The negative ion mass spectrum of anthracene at 70 eV from Dougherty and Weisenberger [27].

Shushan and Boyd [28] have measured fragment ion mass spectra of anthracene ions in isolation and in the presence of helium as a collision gas. Both were measured at 70 eV electron impact. Mathur et al. [29] have measured doubly-charged ion spectra of anthracene and have determined the appearance energies of some doubly charged ions.

Kingston et al. [30] have measured the mass spectra of singly-charged ions produced by doubly- and triply-charged anthracene molecules at 70 eV electron impact. They have observed that the preferred routes for charge separation of doubly-charged anthracene ions lead to the singly-charged fragments  $\text{CH}_3^+$ ,  $\text{C}_2\text{H}_2^+$  and  $\text{C}_3\text{H}_3^+$ . They have also determined the double and triple ionization energies of anthracene, and propose several different fragmentation schemes which will be briefly discussed in Chapter 5.

### 1.3.2 Photon Impact Studies

At a fixed photon energy of 40.8 eV, Hagan and Eland [31] have produced a PEPICO pair spectrum of anthracene via photoionization using filtered HeII radiation. The spectrum illustrates that the most important reactions here involve one small and one large ionic fragment. The intensity of  $\text{C}_2\text{H}_n^+$  fragments is 29.1%, and the intensity of  $\text{C}_3\text{H}_3^+$  is 40.1%, relative to all ions in the pair spectrum for anthracene.

Photoionization studies of anthracene- $\text{d}_{10}$  have been performed by Jochims et al. [32, 33]. They obtained an effective ionisation energy of 7.45 eV. They used the electron storage ring BESSY in Berlin, with a 1 m normal incidence monochromator equipped with a 1200-line  $\text{mm}^{-1}$  grating ( $\text{Al/MgF}_2$ ) and a 1 m Seya-Namioka type normal incidence spectrometer from Bird & Tole.

In 1994, Tobita et al. [34] determined the single and double ionisation appearance potentials of 21 PAHs by measurement of photo-ion yield curves using a synchrotron radiation source. Analogous measurements were made by electron impact on 3 of the PAHs. Both measurements included anthracene- $\text{d}_{10}$ . For the photon-impact measurements, singly- and doubly-charged photo-ion yield curves were measured using monochromatized synchrotron radiation from the electron storage ring BESSY in Berlin. The results showed a photon impact appearance energy of 7.46 eV and a double ionisation potential of 19.6 eV for anthracene- $\text{d}_{10}$ . The ratio of the double to single ionisation potential for photon ionisation was 2.63. The electron impact double ionisation potential for anthracene- $\text{d}_{10}$  was presented as 21.1 eV, and the ratio for the double to single ionisation potential for electron ionisation was 2.83. Differences of up to 4 eV were observed between the potentials for double ionisation from the two techniques.

Robson et al. [35] performed a study of the laser-desorption of anthracene in intense laser fields, using 80 fs, 800 nm laser pulses at an intensity of  $1.5 \times 10^{15} \text{ W cm}^{-2}$ . Figure 1.6

shows the identification of doubly and triply charged fragments in their anthracene mass spectra.

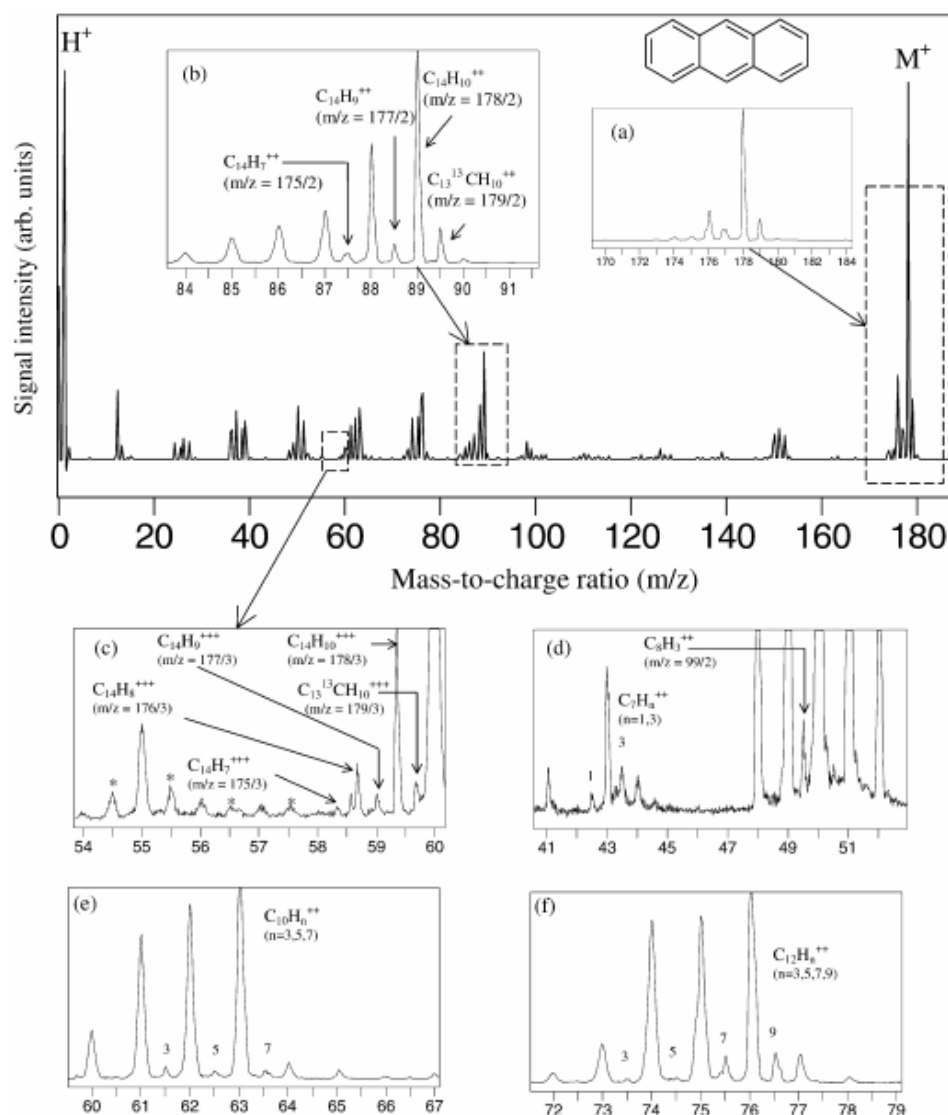


**Figure 1.6** ToF mass spectra of anthracene in intense laser fields showing doubly and triply charged fragments. Robson et al. [35].

### 1.3.3 Ion Impact Studies

In 2012, Reitsma et al. [36] presented an experimental and theoretical study of the energy-dependent fragmentations of anthracene after double electron transfer to a 5 keV proton. The excitation energies leading to the prominent dissociation and fission channels of the molecular dication were determined. The study concluded that the fragmentation of  $C_{14}H_{10}^{2+}$  is dominated by  $C_2H_2$  emission at 10.2 eV, and that H and 2H/ $H_2$  are emitted at 4 eV and 14 eV, respectively, with  $H_2$  emission favoured over 2H emission. They also

concluded that the emission of  $C_3H_x^+$  dominates over the emission of  $C_2H^+$ , with excitation energies of 12.9 eV and 13.6 eV, respectively.

In 2012, Brédy et al. [37] reported on the fragmentation of anthracene molecular ions,  $C_{14}H_{10}^{r+}$ , as a function of the parent ion initial charge  $r = 1 - 4$ . In this study, neutral anthracene molecules in the gas phase were ionised and excited in collisions with  $Ar^{8+}$  ions at 40 keV. Their results indicate that the evaporation and fragmentation pathways are highly competitive, while fragmentation dominates for the  $C_{14}H_{10}^{3+}$  parent ion, and that the observation of stable  $C_{14}H_{10}^{r+}$  ( $1 \leq r \leq 3$ ) ions is explained by electron capture at large distances from the target.  $C_3H_3^+$ ,  $C_3H_2^+$ ,  $C_4H_3^+$ ,  $C_2H_2^+$  and  $C_2H_3^+$  are the main light products of the processes seen in this study. Their mass spectra can be seen in Figure 1.7.

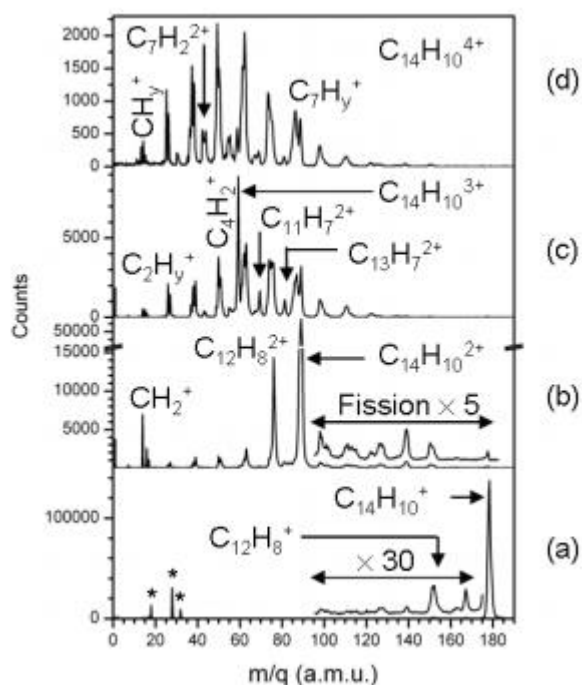


**Figure 1.7** Mass-over-charge spectra of anthracene ions differentiated by the charge  $r$  of the parent ions  $C_{14}H_{10}^{r+}$  from Brédy et al. [37].

In 2014, Postma et al. [38] produced a study on the response of anthracene upon keV  $H^+$  and  $He^{2+}$  impact using high-resolution time-of-flight mass spectrometry. Mass spectra were obtained for 30 keV  $He^{2+}$  interactions with anthracene, with the strongest peak being that of  $H^+$ . There was also a strong signal from the  $C_2H_2^+$  cation. Multiply charged collision products were formed, and the anthracene trication, the triply charged parent ion, occurred for both of the projectiles. A number of dication fragments (doubly charged fragments) were also observed, such as  $C_5H^{++}_m$  ( $m = 2, 3$ ) and  $C_7H^{++}_m$  ( $m = 0 - 4$ ).

## **1.4 Research at Maynooth**

The purpose of the research described in this thesis was to study electron impact fragmentation of anthracene. We have measured mass spectra for positive ions produced by low-energy electron impact on anthracene using a reflectron time-of-flight mass spectrometer. The electron impact energy has been varied from 0 to 100 eV in steps of 0.5 eV. Ion yield curves and appearance energies for most of the fragment ions have been determined.

Chapter 2 presents an overview of the principles of mass spectrometry and a description of some mass spectrometry techniques, including the time-of-flight technique used in this research. Chapter 3 and 4 contain a description of the apparatus used in this study, and the LabVIEW software used for data acquisition and data analysis, respectively. The results are presented in Chapter 5, which also contains a comparison with earlier results and a discussion of possible fragmentation processes.

## 2 Mass Spectrometry

### 2.1 Overview of Mass Spectrometry

Mass spectrometry is a dynamic technique used for the analysis of molecules. It is performed at low pressure, typically  $10^{-3}$  -  $10^{-6}$  Pa, and can provide both qualitative and quantitative information on ions produced from sample molecules. With this technique, typically only a small amount of the sample is required to deduce its structural characteristics, abundances and mass. Applications of mass spectrometry include the structural determination of compounds and the identification of unknown species. This information is obtained by observing the fragmentation pathways of product ions, and by determining the fragment ions of the compounds, respectively. To allow for the product ions to be separated and resolved, their mass to charge ratio,  $m/z$ , is calculated, requiring that the sample be ionised before detection can occur [39].

Mass spectrometers can be adjusted for many different ionisation techniques, and modified to produce either positive or negative ions for detection, depending on the applied fields within the spectrometer and the settings of the detector used. If the mass spectrometer is prepared to separate and resolve positive ions, it would be necessary to alter the electrical potentials and reversed the electric and magnetic fields within the mass spectrometer to prepare it for negative ion detection [40].

Mass spectrometry will mainly produce ions of charge  $\pm 1$  as more energy is required to remove additional electrons from a singly-charged ion. Since ions are resolved based on their  $m/z$  value, the peaks representing these ions in mass spectra will be placed at the mass number associated with that ion. However, multiply-charged ions do occur with this method, for example, with anthracene. If the mass values of these ions are not divisible by the number of charge states they have, the ions will have non-integer  $m/z$  values [41].

The main steps in the methodology of mass spectrometry are executed in a high vacuum setting, necessary to prevent the ions from undergoing collisions with molecules unrelated to this process before detection. Without this procedure, intermolecular collisions may occur, causing the ions to sustain further fragmentation, or to enter undesired deflection paths. Due to this, any mass spectra obtained under these circumstances would be an inaccurate representation of the characteristics of the sample [42].

Five stages can be distinguished in this technique: insertion, ionisation, acceleration, deflection and detection. For the insertion stage, it is necessary that the sample molecules enter the instrument without disturbing the high vacuum environment. Typically, samples are introduced to the apparatus in one of two ways: direct infusion or direct insertion. Direct infusion utilises a form of capillary so the sample may be entered as a fluid, whereas direct insertion employs a probe to insert the sample as a solid [43]. Ionisation can be achieved via multiple methods, and the technique chosen is largely dependent on the phase of the sample during spectrometry, as well as the efficiency of particular techniques on certain species which is related to internal energy transfer [44]. The ionisation stage is necessary because particles that are electrically charged, rather than electrically neutral, can be manipulated by electric and magnetic fields inside the mass spectrometer [45].

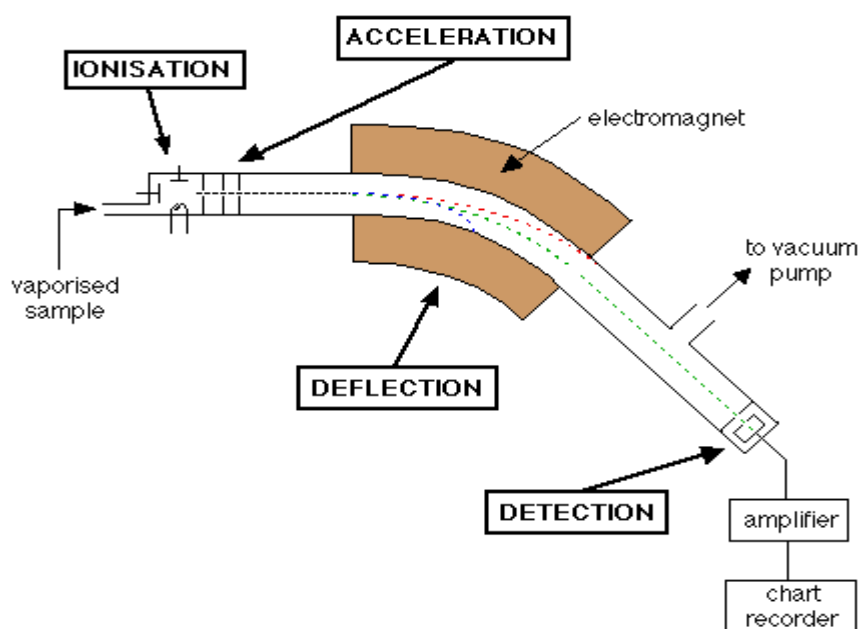


**Figure 2.1** A labelled schematic of a generic mass spectrometer setup [46].

The first ion formation that occurs is that of the molecular ion, which is a neutral sample molecule that has lost/gained one electron, or has undergone proton abstraction, and so carries a charge of  $\pm 1$ . Its mass is that of the sample molecule plus/minus the mass of the particle gained/removed. Due to this, the molecular ion peak is the peak with the greatest  $m/z$  value. As the sample molecules contain distinct atoms that represent the constituents of the sample, the molecular ion is comprised of the most common isotopes of those distinct atoms, also accounting for any changes in mass due to loss or gain of particles [47].

Once ionisation has occurred, the interaction volume contains a mixture of positive and negative ions, as well as many neutral molecules. Statistically, very few ions will be produced relative to the amount of sample used [48]. These products must be separated to allow the desired ions to travel on to the mass analyser and detector, and for the removal of any unwanted ions and neutral products left behind. Thus, an extraction system is in place to appropriately separate these products. A charged plate called a repeller, as well as the charged surfaces of the ionisation chamber itself, repel the desired ions from the interaction volume, while at the same time attracting and neutralising the unwanted product ions. Any unwanted yield is then removed by the vacuum system. A charged plate referred to as an extractor, as well as ion-focussing plates used to focus the exiting ions, carry a charge that is attractive relative to the desired ions. All of these plates have a circular aperture at their centre and are placed at the exit of the chamber. The desired yield is attracted to the plates, due to their relative potential, and accelerated through the plates and on to the next stage of the process [49].

The next stage is the mass analyser section of the mass spectrometer, where the desired ions are accelerated into a magnetic field. The magnetic and electric fields exert forces on charged particles that pass through them, causing the ion paths to be deflected by an amount that is dependent on their mass-to-charge ratio. The direction of the ions is adjusted by the magnetic field, while their speed is increased or decreased by the electric field. Particles of smaller mass, as well as those carrying more charge, will experience greater deflections [50]. Those of the same mass-to-charge ratio will be given the same velocity and so will undergo the same amount of deflection, whereas those with different mass-to-charge ratios are given different velocities, and as such will take different times to travel their trajectory. If the velocities and paths of each one of the ions is known, their masses may be calculated, allowing the mass analyser to sort them based on their mass-to-charge ratio. Within electric and magnetic fields in a vacuum, and for ion velocities much lower than the speed of light, the laws that govern the motion of the ions are Newton's Second Law of Motion and the Lorentz Force Law:

$$\mathbf{F} = m\mathbf{a} \tag{1}$$

$$\mathbf{F} = Q(\mathbf{E} + \mathbf{v} \times \mathbf{B}) \tag{2}$$

where  $\mathbf{F}$  is the net force acting on the charged particle,  $m$  is the mass of the particle,  $\mathbf{a}$  is the particles acceleration,  $Q$  is the ionic charge ( $Q = ze$ ),  $\mathbf{E}$  is the electric field and  $\mathbf{v} \times \mathbf{B}$  is a vector cross product where  $\mathbf{v}$  represents the ion velocity and  $\mathbf{B}$  is the applied magnetic

field. As both of the above equations are equal to the net force acting on the ions, they can be equated to produce an expression that describes the classical motion of the ions. For  $v \ll c$ :

$$\left(\frac{m}{Q}\right) \mathbf{a} = \mathbf{E} + \mathbf{v} \times \mathbf{B} \quad (3)$$

From this expression, it can be seen that the motion of the ions is evaluated in terms of their  $m/z$  values, and as such this equation is the basis of operation for mass analysers used in mass spectrometry [51].

The detection stage begins once the ions, now sorted by their  $m/z$  values, flow from the mass analyser to the detector. Detectors used in mass spectrometry measure a particular quality of the ions present and utilise the measurements to allow for the calculation of the abundance of each distinct ion. It will detect the ions electrically, typically recording the current produced due to ions striking the detector. There are various detectors that can be used in mass spectrometry such as faraday cups, electron multipliers and microchannel plate detectors to name a few. It is often necessary for the chosen detector to considerably amplify the recorded signal as, at a particular time, the number of ions reaching the detector can be quite low [52]. The detection results are mass spectra displaying the relative abundance of detected ions as a function of mass-to-charge ratio. Once mass spectra have been obtained, depending on the resolution of the mass spectrometer, information about the samples chemical composition, structure, and its constituent's abundances and isotopes can be determined [53]. The following sections will present an overview of mass spectrometry using mass filters, which filter sample ions based on their  $m/z$  values, and ion traps, used to trap charged particles. The theory for the design of time-of-flight mass spectrometers will also be presented.

## **2.2 Mass Spectrometry Using Mass Filters**

### **2.2.1 Quadrupole Mass Filter**

A quadrupole mass filter is a type of mass analyser, used in mass spectrometry, that is composed of four parallel, cylindrical rods acting as electrodes. In a quadrupole mass spectrometer, a quadrupole is employed to separate, or “filter”, sample ions based on their mass-to-charge ratio. This is not done through the use of magnetic fields, but instead through the use of alternating electric fields that surround the rods. Each diametrically

opposite rod is coupled electrically, where one pair of opposing rods has an applied potential given by:

$$(U + V \cos \omega t) \quad (4)$$

and the second pair of opposing rods has an applied potential given by:

$$-(U + V \cos \omega t) \quad (5)$$

Here,  $U$  represents a DC offset voltage and  $V \cos \omega t$  represents an AC radio frequency voltage. The determination of which ions will reach the detector relies on the ratio of these voltages. Depending on the value of this ratio, only ions of a certain  $m/z$  will pass through the quadrupole and be detected. This is due to the voltages affecting the trajectory of ions along the flight path. Only ions whose trajectories remain stable within the oscillating fields surrounding the rods will pass through the filter. All other ions are expelled from their initial paths due to the instability of their trajectories and collide with the rods, discharging on impact. This information allows the operator of the spectrometer to select a particular applied voltage that would permit the detection of ions of a specific mass-to-charge ratio, or to select a range of applied voltages to scan through to detect a range of  $m/z$  values. A mass spectrum can then be produced by varying the applied voltage on the rods and observing the corresponding detected ions for each variation [54]. Thus, the resolution of the quadrupole is determined electronically through the selection of the applied voltage values.

The positive DC potential is applied to the rods situated in the x-z plane, and the negative DC potential is applied to the rods in the y-z plane of the quadrupole, as shown in Figure 2.2. Discussing the detection of cations, as the DC field is positive in the x direction of the rods, the field acts as a high pass mass filter, compelling ions of high mass to the centre of the quadrupole. These ions will then pass through the quadrupole without colliding with the rods along the x direction. Thus, the applied DC voltage focuses the ions. However, the varying AC potential applied in this direction has a greater effect on low-mass ions than heavier ions, producing unstable trajectories. Due to this, the DC potential focuses higher mass ions, and the lower mass ions are kept in phase with the AC potential. Here, the ions energy increases due to the energy in the field, causing the low-mass ions to oscillate with increasing amplitude until they are discharged on collision with one of the rods [54].

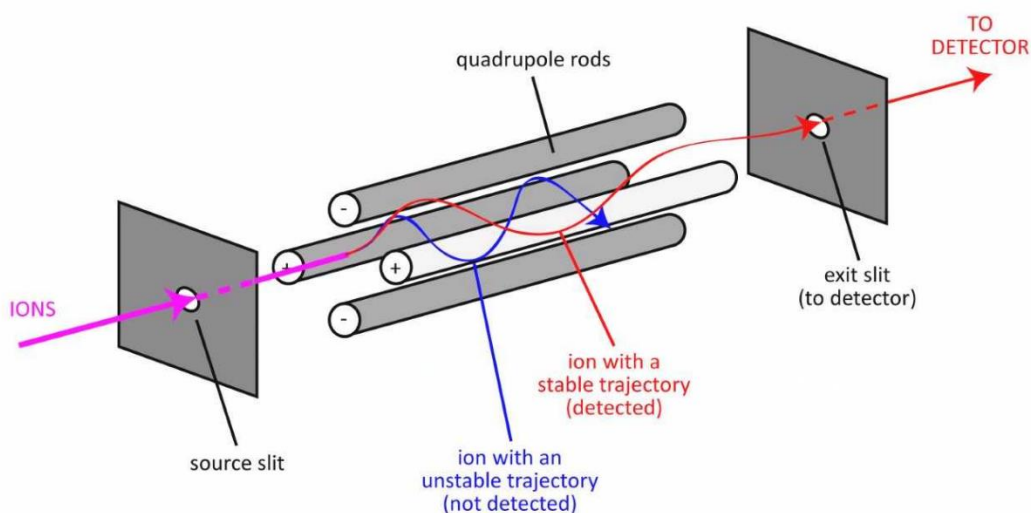


**Figure 2.2** A quadrupole mass filter [55].

For fragmentation studies, multiple quadrupoles can be used in series in order to determine structural characteristics of compounds. An example of this is a triple quadrupole mass spectrometer. The first quadrupole is used as a mass filter, allowing an ion of known mass to pass through. In the second quadrupole, which is used as a collision cell, the ion is broken down into fragments via collision-induced dissociation. The third quadrupole is then used to scan the  $m/z$  range produced due to the fragments, allowing the intensity of each fragment to be obtained and thus, the structural characteristics of the ion can be determined [56]. Quadrupoles can also be used in hybrid mass spectrometers which use multiple devices for the separation of ions. Typically, magnetic sectors are used alongside quadrupole mass analysers due to the magnetic sectors high resolution and accuracy capabilities. Also, the resolution of a quadrupole mass filter is enhanced when a magnetic field is applied to it [57].

### 2.2.2 Magnetic Sector Mass Filter

A magnetic sector mass filter is a mass analyser that uses a magnetic field to separate ions according to their mass-to-charge ratio. For an ion to reach the detector, it must travel along a curved path of a specific radius within the magnetic field, where both the force of the applied magnetic field and the centrifugal force act on the ion. In a magnetic sector mass spectrometer, a strong electric field is used to accelerate the product ions through a narrow slit, focussing them into a beam. The velocity of each ion is determined by the acceleration voltage and the  $m/z$  of the ion. The ions then enter the magnetic sector where,

due to their charge, they are deflected by a magnetic field applied perpendicular to the direction of their motion [58, 59].

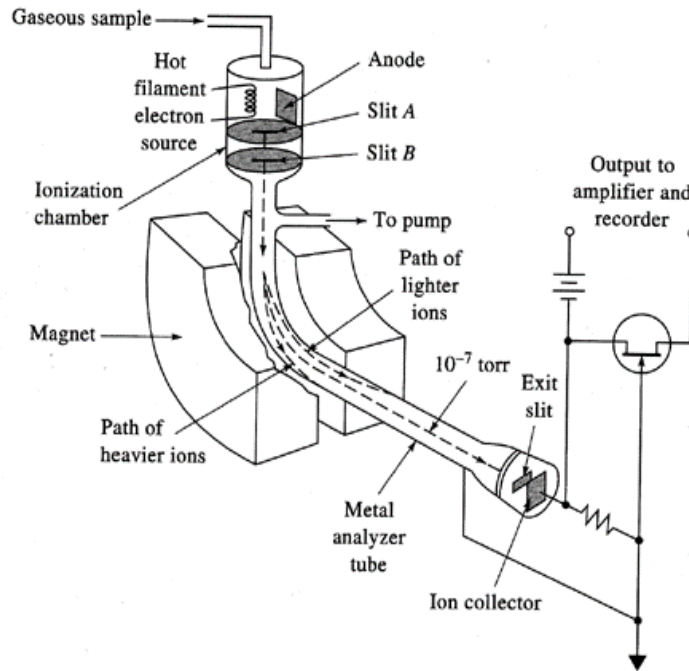


**Figure 2.3** A magnetic sector mass spectrometer [60].

Each ion is deflected to a circular path of radius  $r$  which is dependent on the momentum of the ion, its charge, the acceleration voltage  $V$  and the magnetic field strength  $B$ . This is shown in the following formula [58]:

$$\frac{m}{z} = \frac{B^2 r^2}{2V} \quad (6)$$

The greater an ions momentum, the larger the radius of the path it traverses. Only ions of a particular mass-to-charge ratio will reach the detector for a specific selection of the radius, magnetic field strength and acceleration voltage. Ions of the same  $m/z$  value follow trajectories of identical radius within the magnetic field [61]. Ions with  $m/z$  values differing from that specified to reach the detector will collide with the walls of the flight tube and discharge.

If the magnetic field strength is gradually varied while the acceleration voltage and the radius of trajectory are held constant, ions of different masses will traverse paths of equal radius within the magnetic field. All ions will then reach the detector sequentially, and a mass spectrum will be produced. If the magnetic field strength is set to zero and is gradually increased to its maximum value, it would be expected that the ions with the

most charge and least momentum will reach the detector first, whilst ions with the least charge and the most momentum will reach the detector last [59].

It is not typical to vary the acceleration voltage whilst keeping the magnetic field strength constant as this can affect ion focussing, producing a decrease in ions reaching the detector. The acceleration voltage is fixed at a value that constitutes optimum sensitivity for the system, which is determined by the rate of sampling of the ion beam. The sensitivity of the system is also influenced by the scanning speed, i.e. the rate of change of the magnetic field strength. A higher scan speed permits less ions of a certain  $m/z$  value to reach the detector, whereas a lower scan speed can increase the sensitivity of the device by permitting more time for ion current integration at each  $m/z$  value [62]. The sensitivity of a magnetic sector is also affected by the range of available magnetic field strength values, resulting in larger and larger systems being produced to increase the performance of the device [63].

A magnetic sector used on its own is a single-focussing device. Here, ions that traverse a trajectory within the flight tube have a kinetic energy distribution that is centred around a mean energy value. Magnetic sectors are capable of higher resolving power and a greater mass range than quadrupole instruments, but the kinetic energy distribution can restrict its resolving power. Often, a magnetic sector is used in series with another focussing device, such as an electric sector, to produce a double-focussing instrument. Ions are then separated according to their mass and energy, greatly improving the resolving power [62].

## **2.3 Mass Spectrometry Using Traps**

### **2.3.1 Quadrupole Ion Trap**

A quadrupole ion trap is a type of trapping analyser used to confine charged particles in changing electric fields. This type of trap is also called a Paul ion trap in honour of Wolfgang Paul who co-invented the trap with Hans Georg Dehmelt. These ion traps are produced using DC and radio frequency AC electric field configurations [64], allowing the use of the trajectory stability of the ions to separate them according to their mass-to-charge ratio. These traps can be used as wide range mass spectrometers due to their mass selective instability. They use resonance ejection for isolation and activation of the ions. They are also used as ion storage devices [65]. They can store ions by generating a trapping potential well that can confine gaseous ions for certain periods of time. This

trapping potential is formed when a variable potential is applied to the ion traps electrode rods, which can be adjusted so that only ions of a particular mass will travel through the electrodes and reach the detector [66].

Static electric fields cannot be used to trap an ion in all the directions necessary here. However, alternating electric fields can be used to produce an average trapping force in all required directions. These alternating fields are generated by switching the confining and non-confining directions of the field at a radio frequency whose rate is faster than the time it would take the charged particle to escape the ion trap [67].

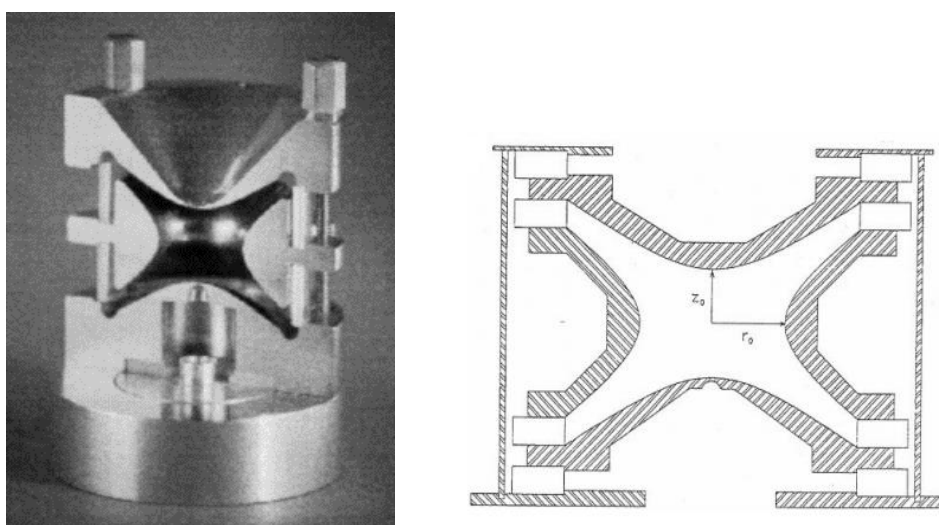


**Figure 2.4** A photograph and schematic of a quadrupole ion trap [68].

The trap consists of three metal electrodes: two identical hyperbolic electrodes, called end-cap electrodes, and a hyperbolic ring electrode placed halfway between the end-cap electrodes. The foci of the end-cap electrodes face each other. The first electrode has an entrance aperture, and the second an exit aperture, to allow particular ions to pass through to the detector. The space between the three electrodes contains an AC and DC electric field configuration, where all the ions that enter through the entrance aperture, regardless of their mass, will be trapped on a three-dimensional trajectory around the saddle point produced. The ions, usually all of the same charge, will repel each other when inside the trap, causing their trajectories to expand as a function of time. By gradually increasing the radio frequency potential on one of the three electrodes, ions will then be expelled from the trap based on their  $m/z$  values. Ions of different mass-to-charge ratios will successively exit the trap and impinge on a detector, creating a mass spectrum [69].

To decrease ion loss in this method, the trap typically contains helium gas. Helium is used to reduce the kinetic energy of the ions and contract their trajectories toward the centre of

the ion trap. This occurs due to momentum-dissipating collisions between the ions and the helium particles [70].

### 2.3.2 Penning Ion Trap

The Penning ion trap, named after F.M. Penning, is a trapping analyser employed for precision mass measurements of ions. It utilises a homogeneous axial magnetic field to restrict ion movement radially, and an inhomogeneous quadrupole electric field to restrict axial ion movement. This confines the ions three-dimensionally, thus trapping them [71].

The basis for the use of Penning ion traps in mass spectrometry is that the frequencies of motion for an ion within the trap are dependent on the ions mass [72], and single ions can be confined within the trap due to their sensitivity to the electric and magnetic field configuration. The uniform magnetic field is superimposed along the axis of the trap, and the non-uniform electric field is superimposed on the magnetic field. This is accomplished using the electrode setup of a quadrupole ion trap.

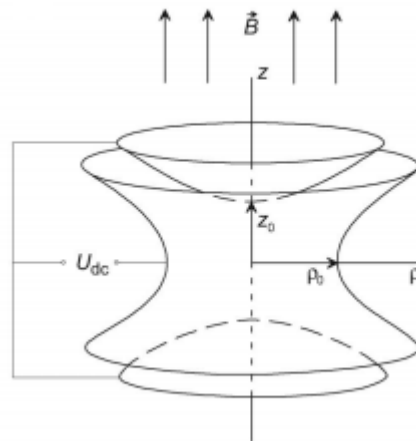


**Figure 2.5** A schematic of a Penning Ion Trap, consisting of two end electrodes and a hyperbolic ring electrode [73].

Ions enter the trap through the entrance aperture of the first electrode. This focuses the ions, producing an ion beam. In the magnetic field of the trap, the ions are forced into cyclotron motion, travelling in a circular orbit around the axis of the field. This motion has a frequency called the cyclotron frequency,  $f_c$ , given by [74]:

$$f_c = \frac{qB}{2\pi m} \quad (7)$$

which is proportional to both the magnetic field strength and the mass-to-charge ratios of the ions. Due to this, the cyclotron frequency is a means of measuring the ion mass-to-charge ratio.

The ions within the electric and magnetic field combination of the trap move in complex, epicyclic orbits in the radial plane, and undergo harmonic oscillations within the axial plane of the field. These oscillations are detected by an external detector held at a low temperature to allow for higher precision. The amplitude of this motion decreases as it reaches thermal equilibrium with the low temperature detector [75]. The magnetic field strength is adjusted in order to resonantly excite ions of a particular mass, expelling them from the trap. The resolution of the trap depends on the coherent interaction times of the ions with the alternating magnetic field.

The mass range for Penning ion traps is given by the strength of the applied fields. The mass range can be large once the trapped ions move within the range of stability of the trap [72]. The two main methods used to determine the cyclotron frequencies of ions are the time-of-flight-ion-cyclotron-resonance method, and a method in which the image current induced by oscillating ions in the trap electrodes is measured [74].

## **2.4 Time-of-Flight Mass Spectrometry**

### **2.4.1 Linear Time-of-Flight Mass Spectrometry**

Time-of-flight mass spectrometry is a method of mass spectrometry that primarily depends on the time taken for an ion to travel the length of the flight tube portion of the mass spectrometer to determine its  $m/z$  value. The flight times can be converted to mass-to-charge ratios once the ions begin their flight with the same kinetic energy. In this way, time-of-flight mass analysers are unlike scanning devices, such as magnetic sectors, as they principally rely on temporally discrete measurements which can be converted to represent corresponding mass-to-charge values.

In 1955, Wiley and McLaren published a paper presenting a design for a pulsed electron-impact time-of-flight mass spectrometer. In this spectrometer, ions are formed in a pulsed electron-impact source from which they are then extracted and directed down an evacuated linear flight tube to a detector. The ions are accelerated towards the flight tube by a potential difference applied between an electrode in the ionisation region and an electrode that leads into the flight tube. This is first-order energy focusing, which allows

control of the focal point. It is used to compensate for the velocity spread of the ions, ensuring each ion has the same kinetic energy upon entering the field-free drift region [76]. Thus, lower mass ions will have greater velocities and reach the detector in shorter flight times than larger mass ions. The ions traversing the flight tube will then have a distribution of flight times in which the time of flight of an ion varies with the square root of the  $m/z$  of the ion. This allows a spectrum of ion abundance versus arrival time to be acquired, and a mass spectrum can be obtained from this by converting the arrival times into mass-to-charge values. This is done using the following equation relating flight time to  $m/z$  [77]:

$$\sqrt{\frac{m}{z}} = \frac{\sqrt{2eV}}{L} t \quad (8)$$

where  $e$  is elementary charge,  $V$  is the acceleration voltage,  $L$  is the length of the flight path and  $t$  is the time taken to traverse the flight path. Using  $A$  to represent the constant  $\frac{L}{\sqrt{2eV}}$  and  $B$  to represent a constant which is added to correct for a small offset in ion start times, it follows that:

$$t = A\sqrt{\frac{m}{z}} + B \quad (9)$$

$$\frac{m}{z} = (Ct + D)^2 \quad (10)$$

where  $C=1/A$  and  $D=-B/A$ .

The derivative of equation (8) produces an equation describing the resolution of a time-of-flight analyser:

$$\frac{1}{z} dm = \left(\frac{2eV_s}{L^2}\right) 2t dt \quad (11)$$

$$\frac{m}{dm} = \frac{t}{2dt} \quad (12)$$

$$\frac{m}{\Delta m} = \frac{t}{2\Delta t} \approx \frac{L}{2\Delta x} \quad (13)$$

where  $m$  and  $t$  are the mass and flight time of the ion,  $\Delta m$  and  $\Delta t$  are the peak widths at half maximum on the mass and time scales,  $L$  is the length of the flight tube and  $\Delta x$  is the diameter of an ion bundle travelling towards the detector.

Primarily, the mass resolution of a time-of-flight analyser is limited by the spatial and energy resolution of the device. The initial spatial and energy distributions present in time-of-flight spectrometers can cause a large time-spread for ions of the same  $m/z$ . Ions that have the same mass-to-charge ratio but different initial positions and/or kinetic energies would reach the detector at slightly different times, resulting in peak broadening. The better a time-of-flight analyser is at reducing this time spread, the higher its mass resolution.

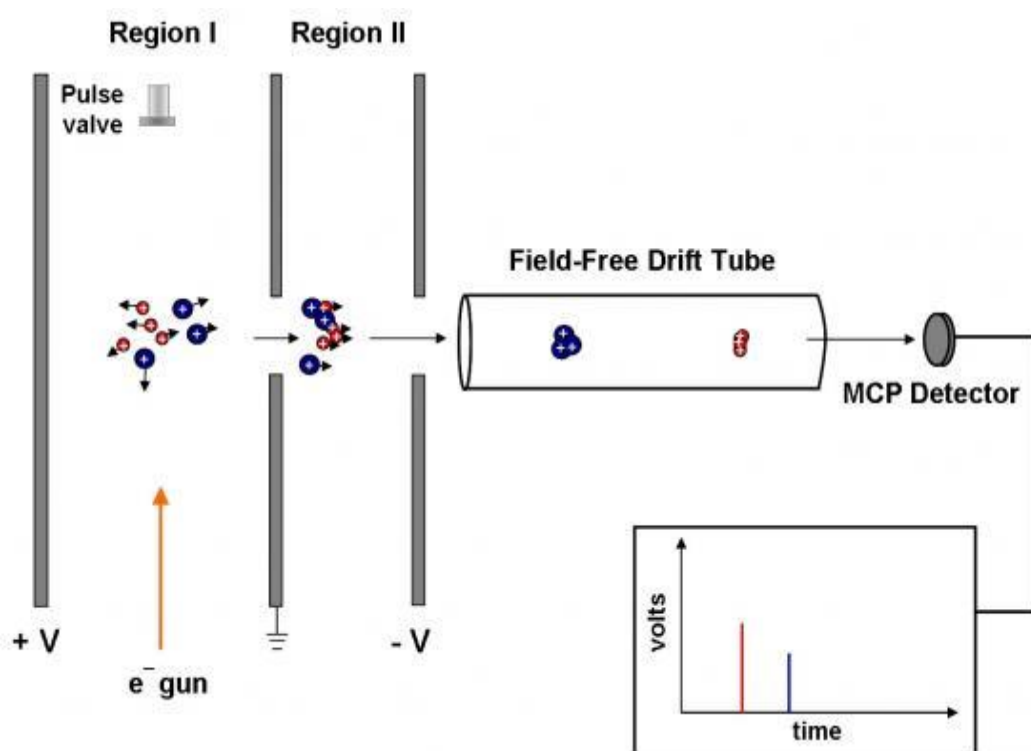


**Figure 2.6** Image of the pathway taken by positive ions in a time-of-flight mass spectrometer [78].

Equation (13) also shows how the mass resolution of a time-of-flight analyser is proportional to both the flight time and the flight path. Lengthening the flight tube would increase the flight path, though too long a flight path would increase ion scatter and ion packet expansion. Decreasing the acceleration voltage would increase the flight time, except too low an acceleration voltage can reduce the sensitivity of the analyser. The values of these parameters should be selected to provide as high a sensitivity and resolution as possible [79].

The use of non-scanning devices such as time-of-flight analysers allows for increased data acquisition speeds as a full mass spectrum can be produced in microseconds for each acceleration pulse. This allows the operator to observe variations in relative ion intensities as the source conditions are modified. Time-of-flight analysers also permit simplified

spectrometer construction as their operation is primarily dictated by electronic circuits, rather than the precise alignment of components to obtain stable electric and magnetic fields [77].

#### **2.4.2 Reflectron Time of Flight Mass Spectrometry**

In this research, a reflectron time-of-flight mass spectrometer built by R.M. Jordan Company was used. The design of the reflectron time-of-flight mass spectrometer, first proposed by Mamyrin in 1972, contains a pulsed ion source, an ion extraction and acceleration region, a field-free drift region, a reflector and an ion detector. This section will detail his work.

Reflectrons have an increased path length relative to a standard time-of-flight mass spectrometer, though the dimensions of the spectrometer are similar, and the reflector, which works as an ion mirror, uses a static electric field to deflect the ions back in the opposite direction. This way, the ions traverse the field-free region a second time. Second-order focusing of the flight time of the ions is achieved by using the reflector, which gives the reflectron an improved mass resolution [80]. Linear time-of-flight spectrometers only achieve first-order focussing.

As groups of ions move through the field-free space within a mass spectrometer, the differences in ion velocity causes the group to expand. For ions with the same  $m/z$  but different initial velocities, the introduction of a reflector into the time-of-flight system compensates for the kinetic energy spread, thus decreasing the spread in flight times. The more kinetic energy an ion has, the further it will penetrate into the reflector field and the longer its path to the detector will be. The result is that ions with slightly larger velocities will remain in the reflector field for longer, and so will reach the detector at the same time as slower moving ions with the same mass-to-charge ratio.

In order to accomplish second-order focussing of the ion flight times, an additional space with a retarding electric field is positioned in front of the reflecting system. The detector is found at the source end of the flight tube as the ions are detected after deflection has occurred [80].

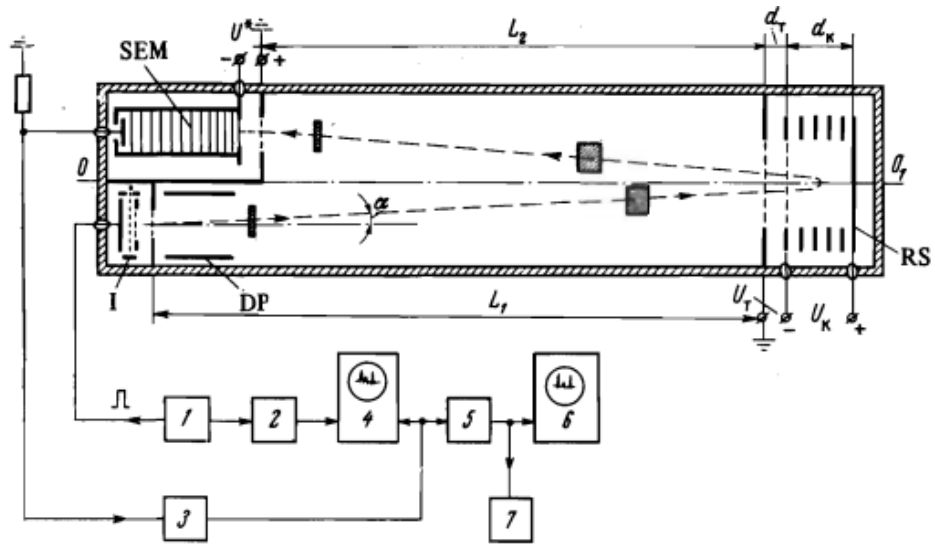


**Figure 2.7** Diagram of mass spectrometer from Mamyrin et al. [80].

As discussed in section 2.4.1, equation (13) indicates that the mass resolution of a time-of-flight mass spectrometer may be improved by increasing the flight path. However, in a linear time-of-flight mass spectrometer, the thickness of ion groups arriving at the detector is given by:

$$\Delta l \approx LT_d \sqrt{\Delta U} \quad (14)$$

where  $\Delta U$  is the initial energy spread of the ions, and  $L$  is the length of the flight tube. The flight time of the ions,  $T_d$ , is expressed as:

$$T_d \sim \frac{1}{\sqrt{U}} \quad (15)$$

taking  $U$  to be the ion energy in the flight tube. Equation (14) demonstrates the dependence of the thickness and flight time of ion groups on the initial energy spread of the ions within the group. For the standard time-of-flight arrangement, though an increase in flight time can increase the mass resolution, a corresponding increase in the expansion of the ion groups will result in a reduction in the resolution.

For the reflectron arrangement, however, the mass resolution of the spectrometer increases with the length of the flight path. Due to the reflector, the flight time of ions from source to detector is then given by [80]:

$$T_0 \sim \sqrt{U} \quad (16)$$

Increasing the flight times of higher velocity ions produces ion groups which reach the detector with a thickness close to their initial thickness before moving through the field-free drift region.

In 2001, Mamyrin published his research into increasing the flight times of ions exiting the source with higher energies using decelerating electric fields. He describes ions entering a decelerating field whose potential increases as  $U = ax^2$ , where  $a$  is constant and  $x$  is the position of the beginning of the field. For an ion of energy  $qU$ , the time taken to stop the ion within the decelerating field is given by [81]:

$$t = \int_0^{x_{max}} \frac{dx}{\sqrt{\frac{2q(U - ax^2)}{m}}} = \frac{\pi}{2\sqrt{\frac{2qa}{m}}} \quad (17)$$

where  $x_{max} = \sqrt{\frac{U}{a}}$ , denoting the position at which the ion stops. Equation (17) indicates that the ion flight time within this field, given by  $2t$ , is independent of the initial velocity of the ion, and thus the resolution of the reflectron is independent of kinetic energy spread. The expression for the ion time-of-flight in a reflectron is given as [81]:

$$t = A_0 \left[ \frac{A_1}{\sqrt{k}} + A_2(\sqrt{k} - \sqrt{k-p}) \right] = A_0 F \quad (18)$$

where  $k$  is the ratio  $U/U_0$ , the mean ion energy is  $qU_0$ , and  $qU$  is the ion energy corresponding to the ion velocity components which are parallel to the instrument axis:

$$k_0 = 1$$

$$p = \frac{U_b}{U_0} \quad (19)$$

$$A_0 = \frac{4d_r}{\sqrt{2qU}} \frac{U_0}{U_r} \quad (20)$$

$$A_1 = \frac{L_1 + L_2}{4d_r U_0} \quad (21)$$

$$A_2 = \frac{d_b U_r}{d_r U_b} \quad (22)$$

where  $U_b$  is the potential difference in the space  $d_b$ ,  $U_r$  is the potential difference in the space  $d_r$ , and  $L_1$  and  $L_2$  are the lengths of the flight paths in the field free drift space and the reflecting field [81].

## **2.5 Ionisation Techniques in Mass Spectrometry**

The diversity of the ions obtained in mass spectrometry is dependent on the ionisation process chosen, and on the characteristics of the components of the sample. In the ion source of a mass spectrometer, preceding analysis, sample molecules must undergo ionisation. A variety of ionisation techniques are available in mass spectrometry, and the internal energy transferred in the process is significant when selecting an ionisation method. There are both hard and soft ionisation techniques, where those defined as hard are chiefly high energy processes that cause excess fragmentation, and modes defined as soft yield less energy transfer, principally producing molecular ions as opposed to fragment ions [45]. With more energy transferred, the excess energy can prompt the destruction of chemical bonds in molecular ions, causing the production of fragment ions. As such, hard ionisation can provide much information on the structural form and formation of compounds, whereas soft ionisation, producing molecular ions, can provide information on the characteristics of compounds, such as molecular mass and composition [82].

This section contains a description of three soft ionisation methods, Fast Atom Bombardment (FAB), Matrix-Assisted Laser Desorption/Ionisation (MALDI) and Electrospray Ionisation (ESI), and one hard ionisation method used in mass spectrometry, Electron Ionisation (EI).

### **2.5.1 Fast Atom Bombardment Ionisation**

Fast Atom Bombardment (FAB) is a soft ionisation technique, yielding low level fragmentation, in which a beam of high energy atoms is used to desorb ions from a surface. This method is typically used for compounds of high molecular weight, those that are thermally and/or energetically labile, and for polar and ionic compounds whose characteristics cannot be exemplified using other ionisation techniques [83].

This approach is performed under vacuum, and for a sample to be analysed using this method it must first be dissolved in a solution known as a matrix, such as glycerol or thioglycerol [84], though the matrix chosen is dependent on whether the sample under

analysis is soluble in the solution. These solutions are used as a defensive environment for the analyte, and as such are non-reactive chemicals that absorb much of the incident energy imparted to the solution by the atom beam [85], while continuously replenishing the sample for desorption [86]. Due to their underactivity, matrix ions will not subject sample ions to undesired chemical reactions, and the presence of the matrix reduces the amount of deterioration the analyte could undergo due to collisions with high energy particles, which would rapidly reduce the yield of secondary ions [87]. Often, a matrix modifier such as trifluoroacetic acid is also added to increase the production of positive ions.

Once the sample-matrix solution has been prepared, it is placed on a metal target surface and bombarded with a beam of energetic atoms, mainly inert atoms or ions of Argon or Xenon, at an energy between 1 and 10 keV [83]. The atoms are ionised before impact, via electron ionisation, in the first chamber of the mass spectrometer. These ions are then collimated and accelerated into the second section of the spectrometer, containing neutral Argon or Xenon atoms. Here, charge and energy exchange occur between the ions and the neutral atoms, wherein the ions are neutralised, transforming from accelerated ions to accelerated atoms.

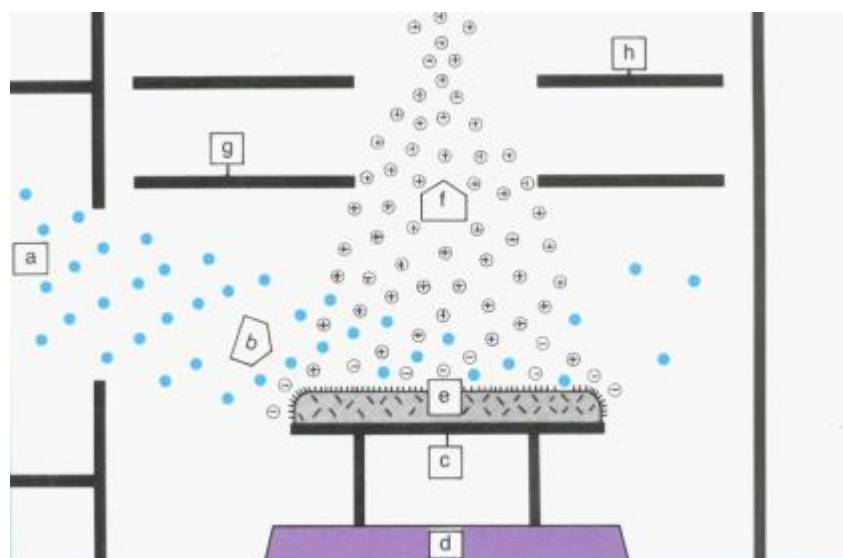


**Figure 2.8** Schematic diagram of a FAB ion source from Barber et al.1982. (a) atom gun; (b) atom beam; (c) metal sample holder; (d) end of probe; (e) sample in low volatility solvent; (f) ion beam; (g) ion extraction plate; (h) lens system leading to mass analyser [83].

Once having exited the second chamber, the atoms are passed through an electric field, increasing their kinetic energy, enter the sample chamber and collide with the sample-matrix solution on the target surface. They then impart their energy to the solution during

interaction, ionising the sample [88]. This causes a momentary but sizable surge in thermal energy. This energy then spreads through the sample, causing some of the sample molecules to dissociate from the mixture in the form of ions, fragments and neutral particles [89]. These products are desolvated in the process, entering the gas phase [90], and any enduring ions will be discharged as the products pass between electrodes in order to be extracted and focussed into the mass analyser of the mass spectrometer.

Both protonated and deprotonated molecules are produced, mostly intact, with little to no fragmentation [89]. The mass spectra produced from FAB contain peaks representing matrix cluster ions, positive ( $M^+$ ) or negative ( $M^-$ ) sample ions, depending on the mode of the mass spectrometer, and ions of any matrix modifiers that have been added to the solution, as well as few fragment ions [92].

### **2.5.2 Matrix-Assisted Laser Desorption/Ionisation**

MALDI is another form of soft ionisation used in mass spectrometry. Its relevance is due to its effectiveness in analysing large, non-volatile, and thermally labile biological and organic molecules, such as proteins. In 1987, Tanaka et al. [93] used an “ultra fine metal plus liquid matrix method” to ionise large biomolecules. Tanaka was the first to demonstrate the abilities of laser technology in the analysis of biomolecules, and shared one half of the Nobel Prize in Chemistry in 2002 with John B. Fenn for his work in mass spectrometry.

MALDI is an effective technique for the generation of non-fragmented gas phase ions, which are produced via the addition or loss of one or more protons. The MALDI process begins with sample preparation, where the compound under analysis is dissolved in, or coated with, a UV absorbent, organic matrix solution. Matrixes typically used in this technique used in this ionisation method are picolinic acid, 3-hydroxypicolinic acid and  $\alpha$ -cyano-4-hydroxycinnamic acid. The sample-matrix combination is then applied to a metal plate, where the matrix begins to dry and crystallise, entrapping the sample within the matrix, and as such the matrix and sample are co crystallised [94]. The analyte molecules are then embedded throughout the matrix so that they are completely isolated from one another. The result is a ‘solid solution’ deposit of analyte doped matrix crystals. The number of matrix molecules widely exceeds those of the analyte, thus separating the analyte molecules and thereby preventing the formation of sample clusters that inhibit the appearance of molecular ions.

The second occurs under vacuum conditions inside the source of the mass spectrometer. Here, a pulsed laser irradiates the solid solution by inducing rapid heating of the crystals. The laser should produce ns pulses, which can be done using a UV laser, such as a nitrogen laser, and frequency tripled Nd:YAG lasers [95]. The energy from the laser accumulates in the solid solution through excitation of the matrix molecules, causing localised sublimation, ablation and ionisation of the matrix-analyte solution.

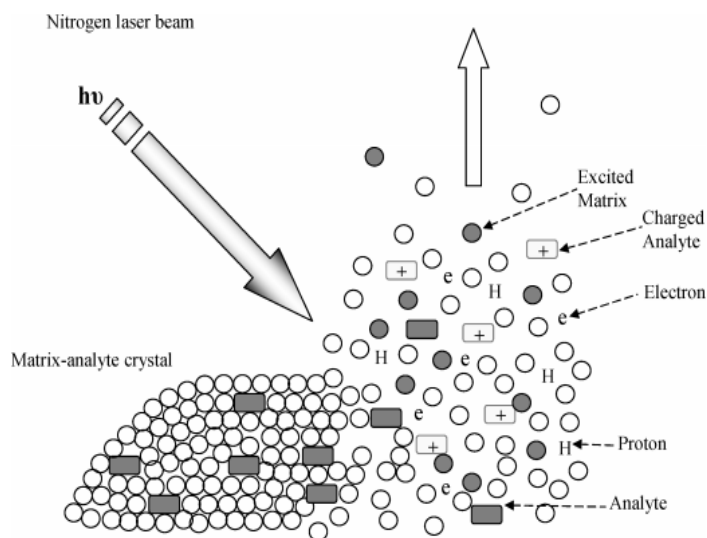


**Figure 2.9** MALDI ionisation process [94].

During ablation of the crystal surface, a hot plume of gases containing neutral, ionised, protonated and deprotonated matrix molecules is generated. The most widely accepted ion formation mechanism in MALDI involves the ionisation of sample molecules via proton transfer in the solid phase before desorption, or gas phase proton transfer in the hot plume of gases. Ion formation occurs between two electrodes which use an electrostatic field to direct the ions towards the mass analyser, where the ions are separated based on their mass-to-charge ratio [96].

The ability of MALDI to create both singly and doubly charged ions is dependent on the choice of matrix and the intensity and voltage of the laser. MALDI spectra mainly contain monocharged molecular species produced by protonation in positive ion mode (though analytes that are not easily protonated can be cationised instead), usually by adding a small amount of alkali, copper or silver cations to the sample. Strong production of parent and fragment matrix ions and some multiply charged ions can also be observed.

A disadvantage of the technique is that the reproducibility and quality of the mass spectra have a strong dependence on sample preparation. Each laser pulse ablates a few layers of the solid solution at the point where the laser irradiates, causing variations in the shot-by-

shot spectrum [94]. However, improving the homogeneity of the mixture will yield better reproducibility. As the efficiency of MALDI is independent of the chosen analyte's size and absorption ability, and because of the pulsed nature of the technique, MALDI is a popular choice for use with time-of-flight analysers.

### **2.5.3 Electrospray Ionisation**

Electrospray Ionisation (ESI) is a soft ionisation technique used in mass spectrometry for the analysis of macromolecules (e.g. proteins). Ions are produced using an electrospray: an apparatus that employs a high voltage applied to a liquid to create a fine aerosol. This technique is particularly effective for large molecules as it overcomes the tendency of these molecules to fragment when ionised, resulting in little fragmentation being visible in the mass spectra.

ESI is performed at atmospheric pressure and involves the use of electrical energy to transfer ions present in the liquid phase into the gas phase before they undergo analysis. Ion formation in ESI involves extensive desolvation, so the solvents used in ESI typically contain water mixed with a volatile organic compound such as dichloroethane or tetrahydrofuran. A solution containing the volatile organic solvent and the chosen analyte is diffused by electrospray into a fine aerosol, which enters the mass spectrometer through a small capillary tube carrying a potential difference of approximately 3000 V. This capillary tube can be heated to aid desolvation. The droplets are then highly charged as they enter a strong electric field in the presence of a flow of warm nitrogen which further assists desolvation [97].

The solvent evaporates from the charged droplets, decreasing their size and leading to their deformation as the electrostatic repulsion of the like charges overcomes the surface tension of the droplets. The surface charge density of the droplets increases until they become unstable and undergo Coulomb fission, breaking up into many smaller, more stable droplets [98]. To reduce the primary droplets size in order to create smaller, more stable secondary droplets, acetic acid and other compounds that increase the conductivity of the solution are added to it. These compounds are also used as a supply of protons, aiding ionisation. These secondary droplets then undergo further desolvation and, subsequently, further Coulomb fission. The electric field strength inside the charged droplets increases to a point where ions at the surface of the droplets are ejected into the gas phase [97].

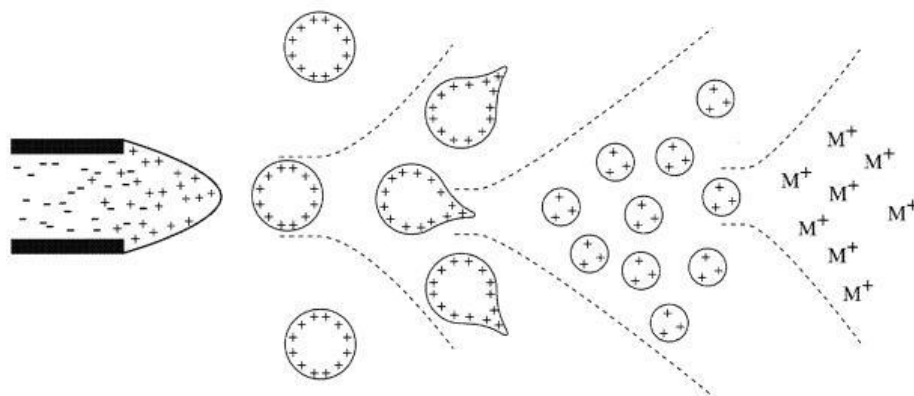


**Figure 2.10** The mechanism of electrospray ionisation [97].

Here, the analyte molecules are not fragmented, but rather turned into smaller and smaller droplets, creating desolvated molecules with extra protons. A skimmer is used to sample these multiply charged ions, which are then accelerated into a mass analyser, such as a quadrupole analyser, before mass spectra can be produced. As ESI produces multiply charged ions, the ions  $m/z$  is reduced compared to singly charged ions, increasing the range of the mass analyser and thus, allowing mass spectra for large molecules to be obtained [99]. As there is little fragmentation achieved with this technique, the molecular ion is always observed. However, little structural information about the molecule can be obtained from the simple mass spectra this technique produces.

#### 2.5.4 Electron Ionisation

Electron ionisation (EI) is a hard ionisation technique in which the electrically neutral molecules of the sample are ionised by a beam of energetic, bombarding electrons, producing ions. As the bond dissociation energies of the compounds analysed using EI are smaller than their ionisation energies, this method provides enough energy for substantial fragmentation of the molecular ion. It is these fragment ions that are separated and detected in order to produce a mass spectrum. Due to the high degree of fragmentation, this technique yields highly detailed mass spectra that can provide important information for structural characterisation and identification of compounds. The molecular weight of the compound can be determined from the fragment ions.

EI occurs in a small chamber within the mass spectrometer. The sample to be analysed must enter the chamber in the gas phase, and the neutral analyte molecules are then streamed into the chamber perpendicular to the electron beam. The electrons are produced through thermionic emission from a heated tungsten filament, and are accelerated through

an electron aperture at a potential difference of between 50 and 70 V, where the incident energy of the electrons is proportional to the potential difference.

At approximately 70 eV, the de Broglie wavelength of the incident electrons is equal to the length of the bonds formed in organic compounds, maximising energy transfer to the sample molecules, and thus, maximising fragmentation. The molecular ion can remain intact, or its molecular bonds can be broken by sufficiently energetic electrons. This can cause such a degree of fragmentation that, with some molecules, the molecular peak cannot be seen in the mass spectra. Above 70 eV, the ionisation efficiency of this technique begins to decrease. The de Broglie wavelength of the incident electrons becomes too small, and the molecules become “transparent” to the electrons [100]. When two or more fragments are produced from the breaking of a chemical bond, the fragment with the lowest ionisation potential typically retains the charge [101].

Once ionisation has occurred, the product ions within the source chamber are repelled by a repeller electrode at the source entrance, and are attracted by an extractor plate at the mass analyser side of the mass spectrometer. This is done to accelerate the ions onto the acceleration region, and thus the mass analyser. The extractor plate is maintained at ground potential so each ion enters the mass analyser with the same kinetic energy. An anode is placed directly opposite the electron aperture to intercept and attract the electron beam after it has passed through the source chamber [102].

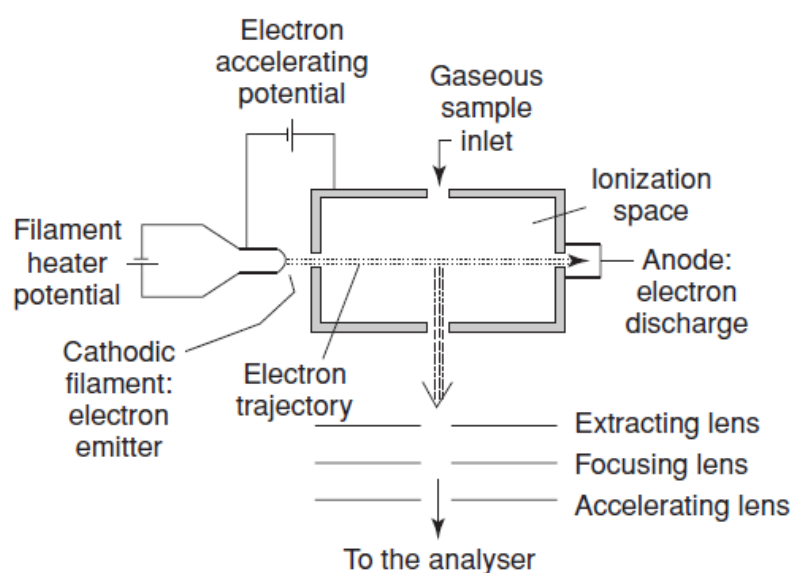


**Figure 2.11** A labelled diagram of an electron ionisation source [101].

Since the ionisation energy range for most organic compounds is much less than the electron energies used in EI, this technique may transfer enough energy to surmount the second and third ionisation energies of analyte molecules. This can lead to the presence of doubly and triply charged fragments in EI mass spectra, although it is not always possible to identify these fragments. The spectra tend to exhibit both molecular and fragment ions, with their ratio depending on the energy required to break the samples molecular bonds. EI is often used with time-of-flight mass spectrometry to obtain the appearance energies of ions and neutral molecules, as well as the ionisation potentials of molecules. It is a reproducible method and high ionisation efficiency can be achieved, though the overall efficiency of the technique depends on the sample's ionisation cross section [102]. Some configurations will use a collimating magnet that surrounds the source chamber, causing the electrons to take a helical trajectory which can also increase the ionisation efficiency. EI is the ionisation method used in this research, and our electron gun and ion source are described in Chapter 3.

## 3 Instrumentation and Setup

### 3.1 Overview of the experiment

The purpose of this chapter is to discuss the instrumentation used in this research. The arrangement contains three vacuum chambers:

- the expansion chamber, in which the oven vaporises anthracene powder to be converted to a molecular beam of anthracene
- the interaction chamber, where a pulsed electron beam is used to ionise molecules of anthracene
- the time-of-flight tube, which contains the reflectron time-of-flight mass spectrometer and the microchannel plate detector.

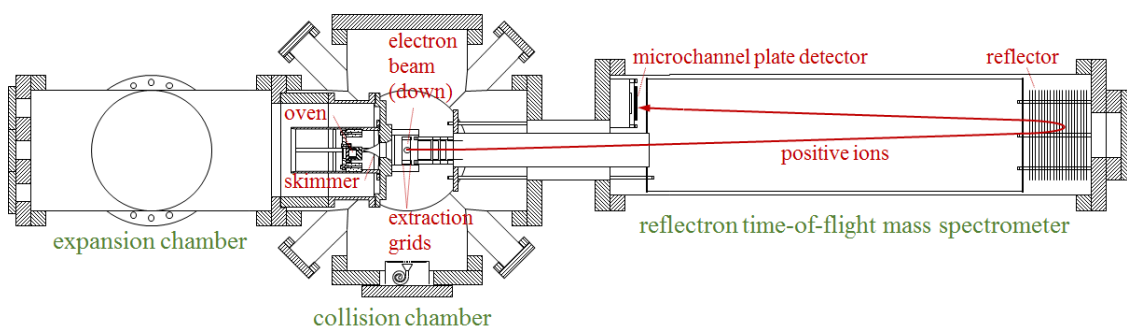


**Figure 3.1** A labelled schematic of the set up used in the research discussed in this thesis.

A vapour of anthracene, produced in a resistively heated oven, exits a small capillary in the oven's casing, and is fed into the expansion chamber where it expands in a plume. A conical skimmer, separating the expansion and the interaction regions of the instrument, then extracts the forward segment of the plume into the interaction chamber. An electron gun is mounted within the interaction chamber, at  $90^\circ$  to the molecular beam.

After ionisation has occurred, extraction grids within this region extract product ions into the time-of-flight tube, as seen in Figure 3.1. The electric field of the reflector, situated at the end of the flight tube, reflects the ions down the length of the flight tube once again, and they are then detected by a microchannel plate detector.

All three chambers are vacuum-sealed together and held on a movable aluminium support. This lets the chambers be separated to allow access to the interior of the system.

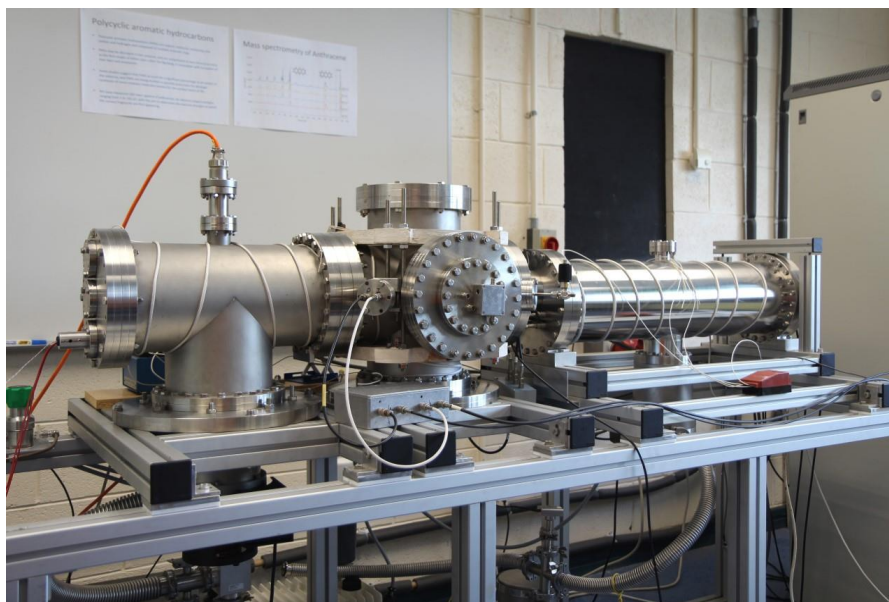


**Figure 3.2** A photograph of the set up used in this research.

### **3.1.1 Vacuum System**

This experiment is performed under high vacuum conditions to prevent reactions between sample molecules and substances external to this research. Evacuation of the chambers is required to prevent molecules, such as air molecules, from interacting with the sample and contaminating the chamber. As such, five vacuum pumps are employed to obtain a sufficient vacuum throughout the apparatus. This vacuum system consists of three turbomolecular pumps and two rotary vane pumps.

A turbomolecular pump is a vacuum pump built to achieve high vacuum conditions by imparting momentum to gas molecules via a high-speed rotor. These pumps have a rotor that collides with molecules entering the pump, and drives them through the pump towards an outlet, creating a vacuum [103]. Due to their design, turbomolecular pumps are incapable of pumping against atmospheric pressure, making it necessary to couple them with a rotary vane pump.

A rotary vane pump is a type of positive displacement pump, which works by displacing a fixed volume of trapped fluid from the pumps suction pipe and into its discharge pipe using an expanding cavity. These pumps are used to initially evacuate the system to a low enough pressure that the turbomolecular pump can start pumping. Once pumping, the rotary vane pump acts as a support pump, maintaining a sufficiently low pressure at the outlet of the turbomolecular pump [104].

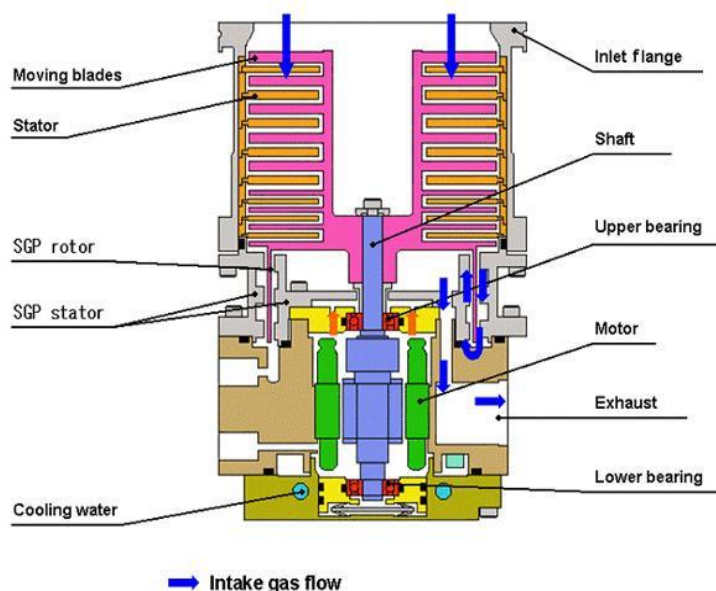


**Figure 3.3** A labelled cross section of a turbomolecular pump [105].

The expansion chamber is held under vacuum by a Leybold Turbovac 360 turbomolecular pump, coupled with an Alcatel OME 40 S rotary vane pump, keeping this region at a pressure of  $4.4 \times 10^{-6}$  mbar when the oven is in operation. The interaction chamber and the time-of-flight tube each have their own Leybold Turbovac 361 turbomolecular pump, both coupled with the same Leybold Trivac D25B rotary vane pump, with these regions kept at a pressure of  $1.7 \times 10^{-8}$  mbar. Each chamber is also vacuum-sealed using copper gaskets and/or Viton O-rings.

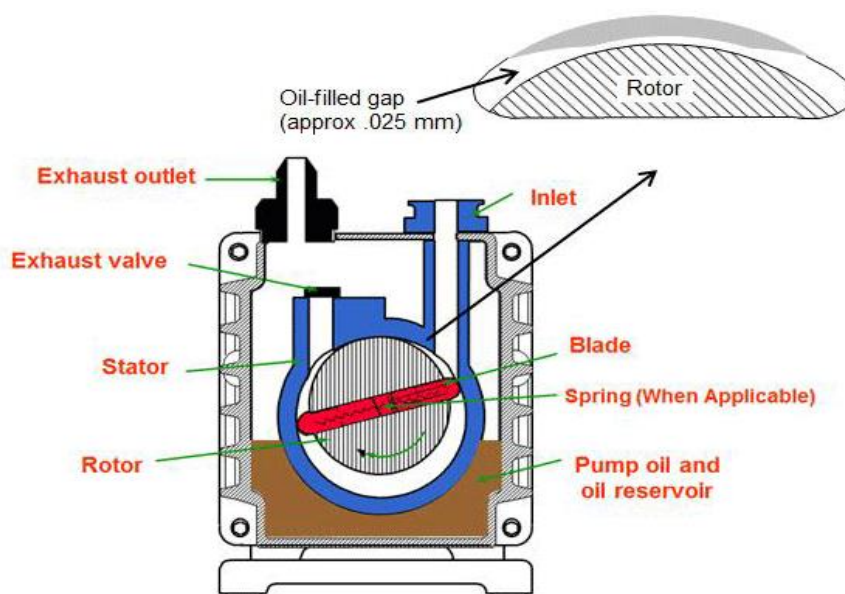


**Figure 3.4** A labelled cross section of a rotary vane pump [106].

It is necessary to continuously monitor the pressure of these regions when the apparatus is in operation in the event that a pump fails to function, or the efficiency of a pump is

beginning to decrease over time. Thus, a pressure-monitoring system was constructed for the experiment, consisting of:

- two Arun Microelectronics UHV Bayard-Alpert AIG17G Ionisation Gauges,
- two Arun Microelectronics PVU Pirani Gauges,
- two Arun Microelectronics PGC2 Pressure Gauge Controllers.

An ionisation gauge is installed at the expansion chamber of the experiment, and a Pirani gauge is connected to its backing pump, with both gauges being read by one of the pressure controllers. The other ionisation gauge and Pirani gauge are installed at the interaction chamber and at the chambers backing pump, respectively, with both these gauges being read by the second pressure controller. The gauges monitor the pressure in their respective regions, and the pressure controllers display the measurements obtained by the gauges.

Ionisation gauges are used as measuring devices in low pressure vacuum systems, and work by indirectly measuring pressure via the detection of gas ions. These gauges are constructed as a triode, which is a vacuum tube containing three electrodes; a heated cathode, a helical grid and a collector plate.

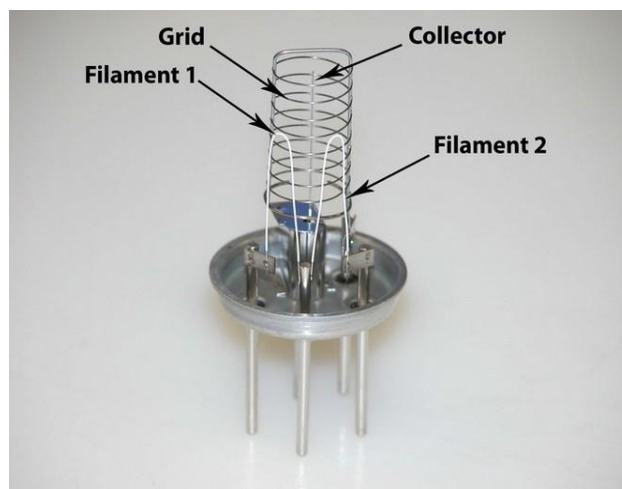


**Figure 3.5** A labelled image of a nude ion gauge [107].

The cathode filament creates an electron current by thermionically emitting electrons, which are then attracted to the grid electrode by a positive potential. Many of the electrons produced pass through the grid, causing them to interact with gas molecules within the system being monitored. This causes the ionisation of a few of these molecules, producing positive gas ions that become attracted to the anode plate, which the ion current can be taken from. The ion current permits a gas pressure measurement to be taken as the current

in the anode is proportional to the rate of ionisation. Ionisation is less likely to occur in the presence of very few molecules, where the number of molecules is dictated by the vacuum state of the system. The less gas ions that are detected, the lower the gas density within the system, therefore the rate of ionisation is a function of the pressure within the system. At constant pressure, the absolute gas pressure can be determined from the current on the collector [108].

Pirani gauges are another form of gauge that utilise indirect pressure measurements in vacuum arrangements, in this case using thermal conductivity to perform them. The Pirani gauge used in his research is constructed as a metal tube containing a heated metal filament that acts as one arm of a Wheatstone bridge. The gauges used in this research have been connected to the fore pumps of the regions being monitored.

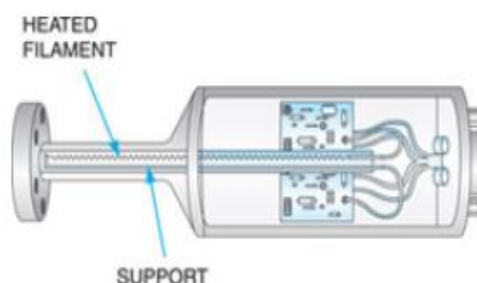


**Figure 3.6** A labelled diagram of a Pirani gauge [109].

The filament will lose some of its heat as molecules inside the glass tube collide with the filament, and the more molecules that are present, the more heat the filament will lose. This heat loss lowers the resistance of the filament, unbalancing the bridge. The number of molecules present is a function of the gas pressure the pump is holding the system at. The lower the gas pressure, the more gradually the filament will lose heat as less molecules will be present in the tube, and the more slowly the resistance of the filament will decrease. At constant temperature and voltage, a measurement of the heat lost by the filament is an indirect measurement of the gas pressure in that region of the system [110].

The two pressure controllers then display a pressure measurement for these regions of the experiment and the user can toggle the display to view the ionisation gauge reading or the Pirani gauge reading.

### 3.1.2 Expansion Chamber

The expansion chamber is the section of the experiment in which the molecular beam of anthracene is generated using a resistively heated oven. The expansion chamber is held under vacuum by a Leybold Turbovac 360 turbomolecular pump, backed by an Alcatel OME 40S rotary vane pump, and is held at a pressure of  $7 \times 10^{-8}$  mbar with the oven off, and  $4.4 \times 10^{-6}$  mbar with the oven on.

The oven in which anthracene is converted to a vapour can be seen in Figure 3.7 mounted in a top hat arrangement within the expansion region. Its dimensions are: diameter of 22 mm; length of 27 mm; base diameter of 34 mm. It contains a Thermocoax SEI 10/100 heater and is constructed from copper and covered by a copper casing. A 0.5 mm diameter capillary in the casing enables the beam of anthracene to exit the oven, and enter a cone-shaped, electroplated skimmer, which separates the expansion chamber from the interaction chamber.

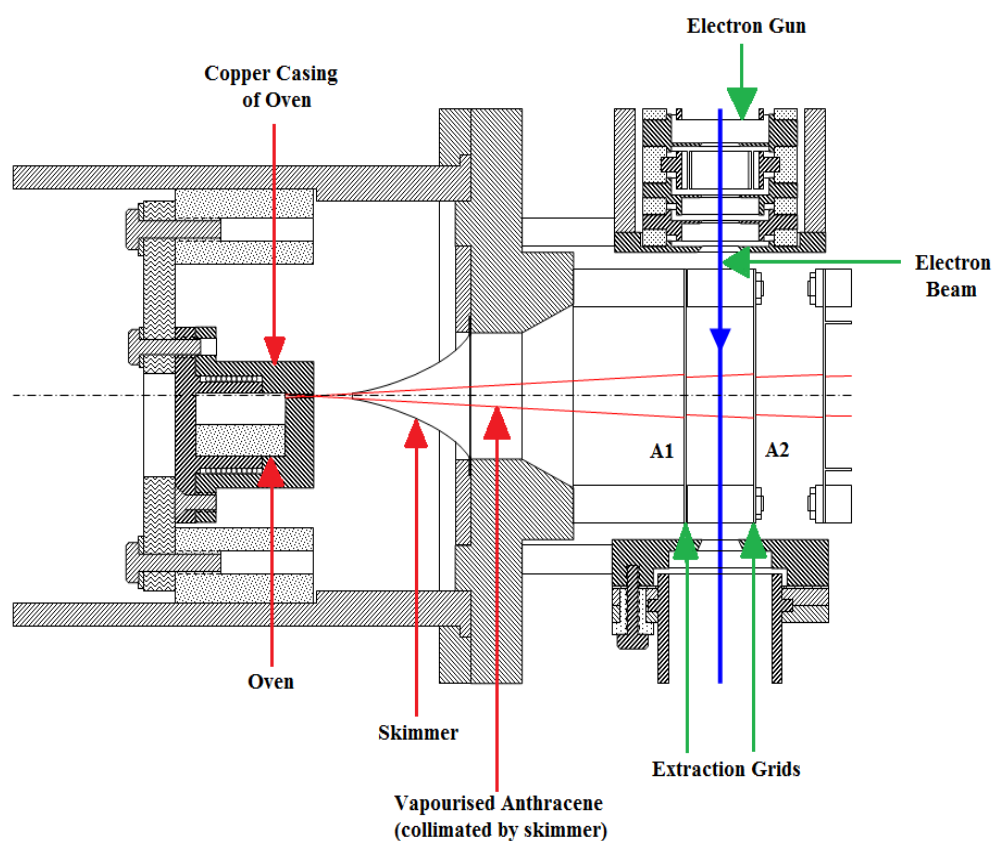


**Figure 3.7** A labelled schematic of the expansion chamber and the interaction chamber used in this research.

Its cone shape allows for collimation of the beam as it enters the interaction chamber, whilst enabling the skimmer to avert divergent molecules. An Omron E5CK PID

controller is used to control the temperature of the oven. For anthracene, this temperature is 180° Celsius. The Omron controller maintains this temperature by continuously switching the current through the oven's heater on and off once the pre-set temperature has been reached.

### 3.1.3 Interaction Chamber

Within the interaction chamber, the anthracene molecules are ionised, via electron ionisation, using a pulsed electron beam. It is here that the fragment ions of the PAH are produced. This chamber is held at a pressure of  $2.5 \times 10^{-8}$  mbar by a Leybold Turbovac 361 turbomolecular pump, backed by a Leybold Trivac D25B rotary vane pump. Here, the molecular beam of anthracene interacts with a beam of electrons. These electrons are created using an electron gun, mounted on the top hat. The section in which the anthracene beam and the electron beam interact is called the interaction region, found between two extraction grids labelled A1 and A2, at +100 V and 0 V respectively.

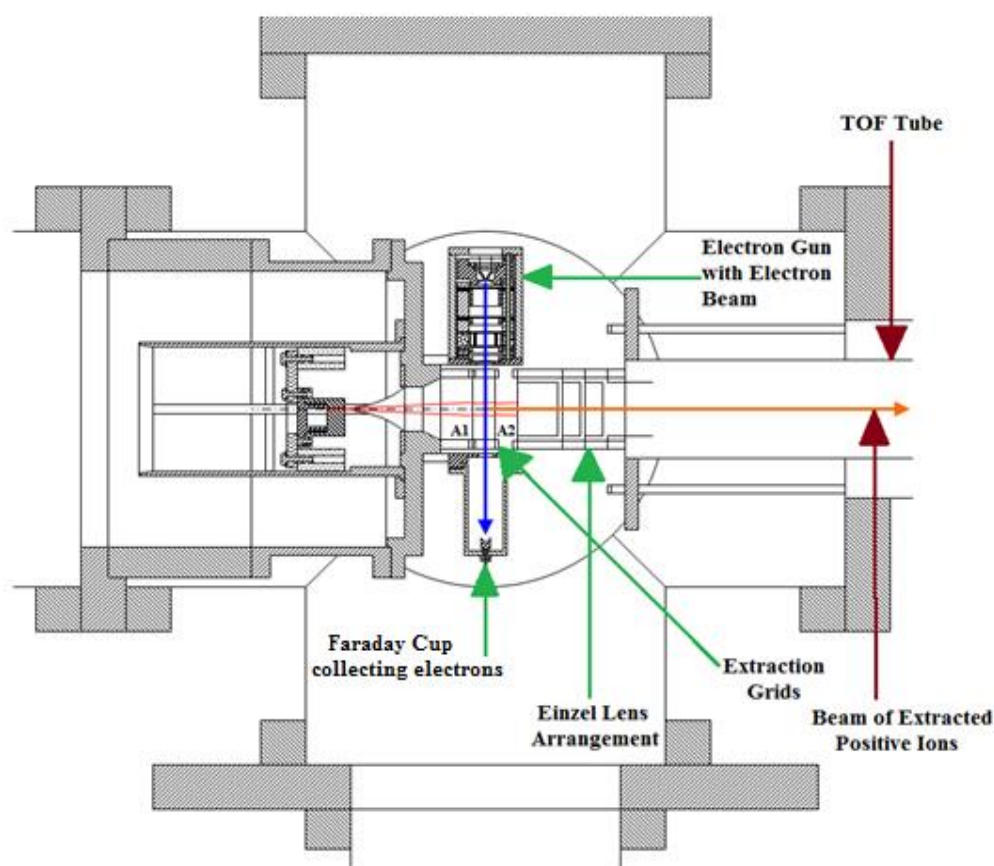


**Figure 3.8** A labelled schematic of the interaction chamber, and a segment of the TOF tube, used in this research.

Mounted below the electron gun is a Faraday cup, consisting of both an inner and an outer cup. The electron beam passes through the ionisation region and is collected by the Faraday cup. It is desirable for the ratio of the current on the inner cup to that on the outer cup to be maximised to obtain optimal focus and alignment of the electron beam.

To extract the fragment ions produced, extraction grid A1 is pulsed. To achieve this, A1 is dropped from +100 V to 0 V just before the electron beam is pulsed. There is then no field between the extraction grids. Once the electron beam has been pulsed and there are fragment ions within the interaction region, A1 is raised to +100 V, causing the positively charged fragments to be repelled into the time-of-flight region. The electron pulse width is 0.3  $\mu\text{s}$  and there is a 50 ns delay between the end of the electron pulse and the rise of the extraction pulse to prevent the electrons from being deflected before they reach the Faraday cup.

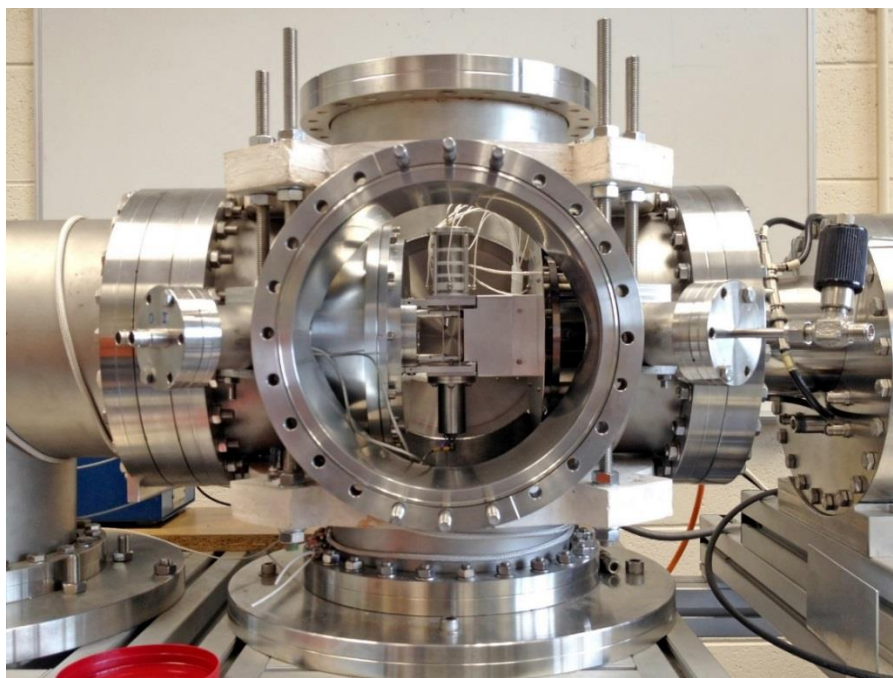


**Figure 3.9** A photograph of the interaction chamber.

### **3.1.4 Time-of-Flight Tube**

The time-of-flight tube is the section of the apparatus that contains the reflectron time-of-flight mass spectrometer (RTOFMS) and the microchannel plate detector (MCP). Here, the detection of the reaction products occurs. The reflectron used in this work is manufactured by R.M. Jordan Company in California. A Leybold Turbovac 361 turbomolecular pump and a Leybold Trivac D25B rotary vane pump are used to maintain the vacuum in this tube at  $1.7 \times 10^{-8}$  mbar.

Due to the pulsing of the extraction grid in the interaction chamber, the product ions are accelerated into an einzel lens to focus the ion beam as it enters the time-of-flight tube. The einzel lens contains three electrodes; the first and third electrode are held at  $-1200\text{ V}$ , and the second electrode is held at a potential of  $-1400\text{ V}$ . This second voltage is labelled  $V_{\text{focus}}$ , as its purpose is to focus the ion beam.

It is necessary that the product ions undergo a slight deflection before traversing the entire flight path, as the MCP detector is not centrally located. This deflection is obtained using the deflection voltages  $XY1 = -1200\text{ V}$  and  $XY2 = -1140\text{ V}$  to guide the ion beam. The liner of the tube, which is insulated from the exterior chamber of the tube, is also held at a potential of  $-1200\text{ V}$ .

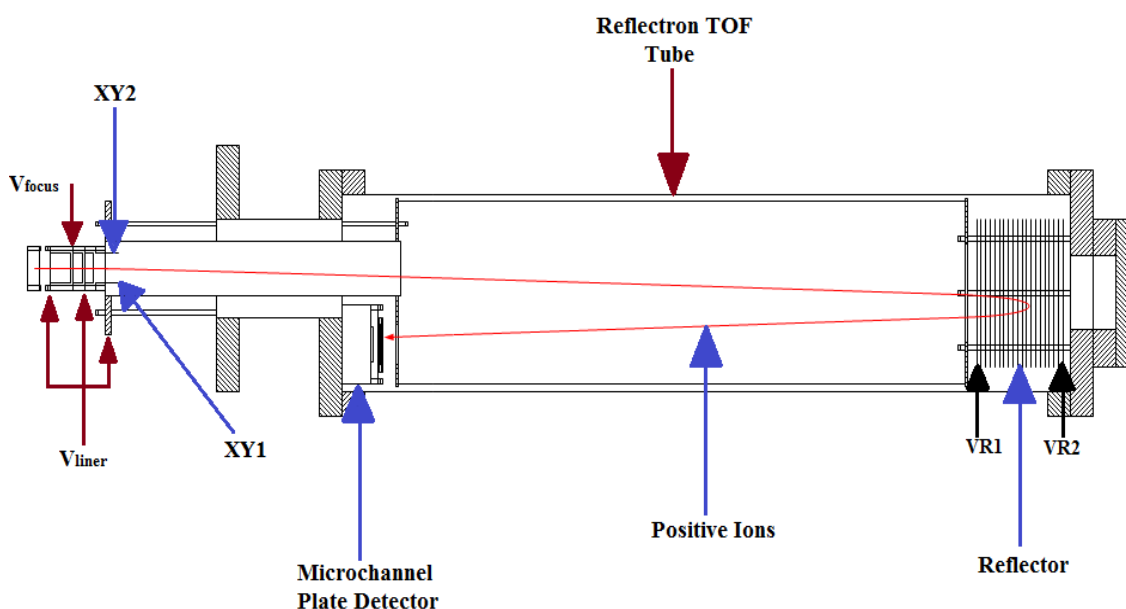


**Figure 3.10** A labelled schematic of the reflectron TOF tube, and voltages on the einzel lens.

Once the ions pass through the flight tube, they enter the reflector. Essential for providing second order focussing of the time of flight of the ions, the reflector voltages  $VR_1$  and  $VR_2$  are set to  $-390\text{ V}$  and  $+87\text{ V}$ , respectively. A series of plates with voltages provided by a resistor divider network ensures that the electric field strength is uniform across the entire reflector. The uniform electric field of the reflector works as an ion mirror, reflecting the ions that enter the field back through the time-of-flight tube.

Opposite the reflector, the microchannel plate detector is mounted at the end of the flight path of the ions. A description of this detector is given in section 3.3.

### **3.1.5 Interlock System**

An interlock box is employed in this research to prevent the system undergoing damage in the event a component was to fail, or if a power outage were to occur. Under such circumstances, it would be necessary for the mass spectrometer and its associated components to shut down, and to not automatically restart when power is restored. An example would be if a high vacuum was not maintained due to a rotary vane pump malfunctioning. This could cause oil from the pump to enter the system, contaminating the equipment and affecting the results.

To ensure the safety of the instrumentation, five pieces of equipment are interlocked in the setup: the three turbo molecular pump controllers and two pressure controllers. Five switches are found on the front panel of the interlock box, each representing one controller. The switches can be set to 'Interlock' or 'Override'. The pump controllers monitor the pumping state of the turbomolecular pumps, pressure controller 1 monitors the pressure at the expansion chamber by reading an ionisation gauge on top of the chamber and a Pirani gauge on the fore line of the chamber, and pressure controller 2 monitors the pressure at the interaction chamber and the flight tube in the same manner. If a turbomolecular pump malfunctions, or an ionisation gauge or Pirani gauge detects too high a pressure in the system, the interlock box will trip and power will be cut to all interlocked devices.

To pump-down the system, all switches on the front panel of the interlock box must be in the override position as the initial pressure would be high enough to trip the interlock box. The fore pumps must first be turned on to pump against atmospheric pressure and the turbomolecular pumps can be turned on once the pressure is low enough for them to pump against. After a short time, the ionisation gauges can be turned on, and once the pressure is lower than the trip pressure, all the trip switches may be placed in the interlock position.

To turn off the system, the trip switches for the turbomolecular pumps must first be switched to the override position before the pumps can be turned off. This is necessary as the pressure will become higher once the pumps are no longer pumping, and so would trip the other interlocked devices. The pressure controllers must then be overridden before the ionisation gauges can be turned off, though it is not necessary to turn off the Pirani gauges as they can withstand atmospheric pressure.

In case of an emergency, the power button on the front panel of the interlock box should be switched to the off position, cutting power to the entire system. If the power in the building were to trip, the solid-state relays in the interlock box would also trip.

### 3.2 The Electron Gun and Faraday Cup

The electron gun is mounted in a top hat arrangement within the interaction chamber, at a 90° angle to the molecular beam. It incorporates a filament holder, a deflection system to control the movement of the beam, and a series of lens elements required for beam focussing, as seen in Figure 3.11 and 3.12.

The tungsten filament of the gun is centred in the gap of the grid element and is supplied a current of 2 A. Electrons are then released from the heated filament through thermionic emission. Using an external power supply, the potential of the filament holder grid,  $V_{\text{grid}}$ , is selected to be slightly negative relative to the potential of the tip of the filament. This potential difference produces a weak electric field that represses electron divergence caused by the filament. The electrons then form a beam before entering the focussing and deflecting segments of the gun.



**Figure 3.11** A photograph of the interaction region, showing the electron gun and Faraday cup arrangement.

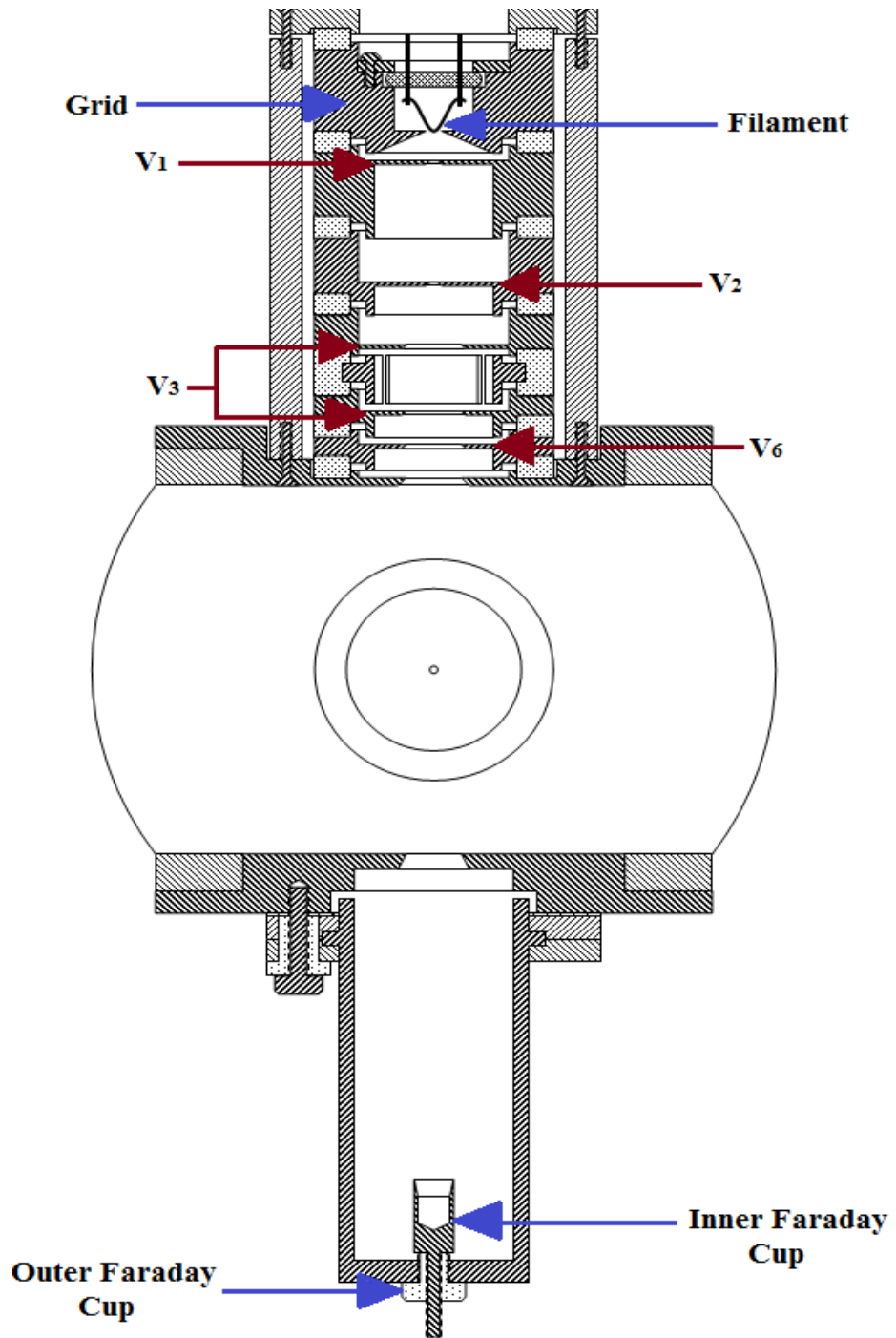


**Figure 3.12** A labelled schematic of the electron gun and faraday cup arrangement in the interaction chamber.

Four electrode lens elements were integrated into the electron gun arrangement to allow the electron beam to be finely focussed. Each lens element is produced from molybdenum, and is insulated from the other lens elements using Macor spacers. The lens element voltages,  $V_1$ ,  $V_2$ ,  $V_3$ , and  $V_6$ , are variable, permitting the operator to adapt the focus of the beam through variations of these four voltages.

Potentiometers protrude from the front panel of the box to permit variation of the voltages, and voltage test points are also found on the front panel so the voltages can be measured with a voltmeter. A KEPCO APH 500M power supply supplies 300 V to the potential divider network. The deflection system requires  $\pm 24$  V to operate, which is provided using two Vxl Power Limited EPSD 15/200C AC-DC converters.

<b>Electron Gun Voltages</b>			
<b>V<sub>grid</sub></b>	-24.9 V	<b>V<sub>filament</sub></b>	2.85 V
<b>V<sub>1</sub></b>	46.1 V	<b>I<sub>filament</sub></b>	2.245 V
<b>V<sub>2</sub></b>	205.7 V	<b>DX<sub>1</sub> / DX<sub>2</sub></b>	$\pm 7.36$ V
<b>V<sub>3</sub></b>	32.4 V	<b>DY<sub>1</sub> / DY<sub>2</sub></b>	$\mp 11.59$ V
<b>V<sub>6</sub></b>	37.2 V	<b>V<sub>incident</sub></b>	100 V
<b>Inner Faraday Cup</b>	6.3 nA	<b>Outer Faraday Cup</b>	0.2 nA

**Table 3.1.** A table of the voltages associated with the electron gun and Faraday cups.

To set the voltages for the lens elements, an electron gun voltage box was used. This feature enables each of the electron gun voltages to be user selected through an array of potential dividers.

The deflection system of the gun was implemented to permit steering of the electron beam, allowing it to be finely aligned with the molecular beam and the Faraday cup. For the beam deflection, a series of four deflection plates, DX<sub>1</sub>, DX<sub>2</sub>, DY<sub>1</sub> and DY<sub>2</sub>, were mounted in the focussing lens element labelled V<sub>3</sub>. Variations of the voltages on these plates result in different orientations of the electron beam.

The electron impact energy is controlled by an individual external programmable KEPCO APH 500M power supply, and is programmed using a LabVIEW interface that increases the incident energy, V<sub>incident</sub>, in 0.5 eV increments, from 1-100 eV.

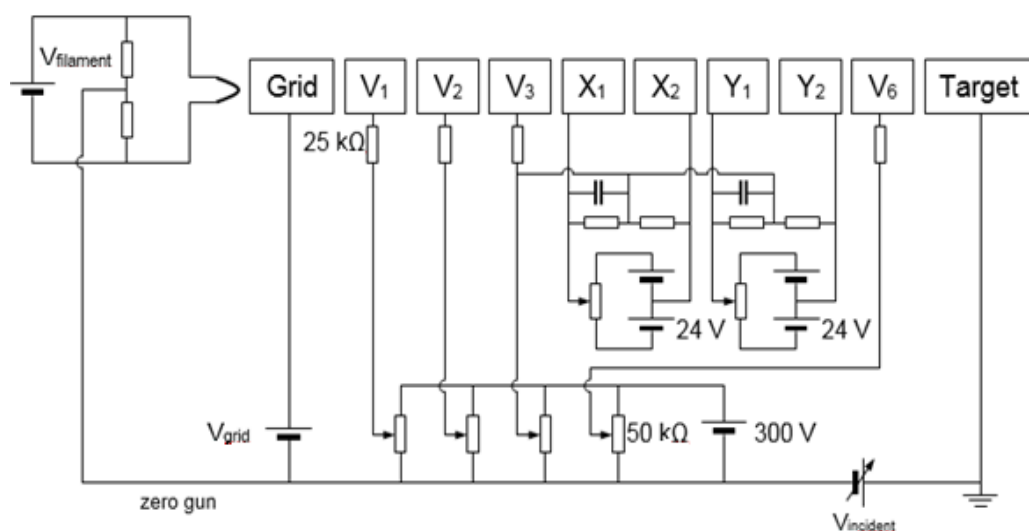


**Figure 3.13** A labelled schematic of the electron gun voltage box.

A Faraday cup, seen in Figures 3.11 and 3.12, is mounted below the interaction region. It contains both an inner cup and an outer cup, held at +40 V and +10 V respectively. This component collects the electrons after they pass through the molecular beam. Each cup has a Keithley 610C ammeter connected to it to measure its current as a function of electron impact energy. This permits the collimation of the electron beam to be monitored. For collimation to be optimal, the current on the inner cup should be maximised and the current on the outer cup minimised. A LabVIEW VI is used for recording the currents on the inner and outer Faraday cups as a function of electron impact energy.

### 3.3 The Microchannel Plate Detector

A microchannel plate (MCP) detector is employed in this research for the detection of positive ions as it has a direct sensitivity to charged particles. MCP detectors are flat plates produced from leaded glass, where their flat design aids in minimising the time spread of the incident ions. The plates contain multiple microscopic channels, approximately  $10^7$  of them, directed from one face of each plate to the other within a strong electric field. Each channel is a dynode electron multiplier of diameter between 10 and 100  $\mu\text{m}$ , and is positioned within the plate at an angle of approximately  $8^\circ$  from normal, relative to the surface. This angle ensures that an ion entering any channel will collide with the wall of the channel, producing a cascade of electrons. The cascade occurs because the channels are coated in a metallic alloy such as nichrome, causing them to emit secondary electrons when impacted. The rate of secondary electron emission is dependent on the velocity with which the ion strikes the surface with no electrons released if this velocity does not exceed

some threshold value. This coating also creates parallel electrical contact between the channels, turning the faces of the MCP into low resistance electrodes [111].

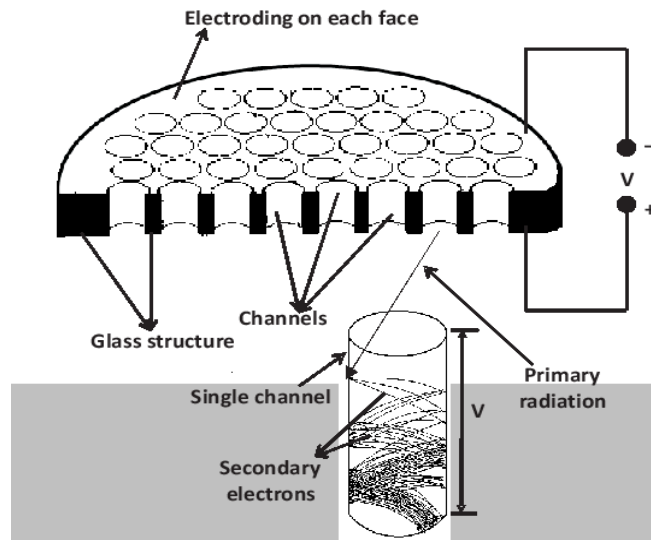


**Figure 3.14** A schematic of a segment of an MCP [112].

As the electrons produced in the cascade collide with the channel walls, the cascade gets larger and more electrons are produced, propagating the length of the channel and amplifying the initial signal. The amount of amplification the signal undergoes is determined by the strength of the electric field the channels are placed in, determined by the voltage difference between the top and the bottom surface of the plate, and by the geometry of the plate [113].

The  $8^\circ$  tilt on the channels is also required to minimise positive ion feedback, which prevents an MCP containing straight channels from producing the gains that a single curved electron multiplier can. As the cascade of electrons becomes greater along the length of the channel, it can cause adsorbed atoms from the channel walls, or rest gas atoms, to become ionised. The ions produced by these atoms can acquire enough energy to release electrons from the channel walls themselves, causing a second cascade. The MCP bias then drives all the electrons produced towards the detector, including those generated in the second cascade, thus distorting the measurement. Tilting the microscopic channels against the direction of the electric field assists in reducing this phenomenon, as well as the use of shorter channels [114].



**Figure 3.15** A photograph of the detector used in this research.

Once the MCP has detected an ion, it must neutralise before the next incoming ion can produce a cascade. The time it takes an MCP to neutralise is referred to as the MCP dead time. This can become an issue if an incoming ion impacts the detector wall before neutralisation has occurred. The ion will therefore not be detected, and saturation of the MCP can ensue due to the output current no longer being proportional to the incident intensity. However, saturation effects can be lessened by using low resistance MCPs [115].

The number of MCPs used, and their potential, affects the gain of the detector [116]. It can be necessary to adopt more than one MCP to achieve the gain required for detecting individual particles, thus two MCPs in chevron arrangement are used in this research.

The detector is biased with a voltage of  $-3800\text{ V}$ . A voltage divider network divides the potential across two plates in such a way that  $VD_1 = -1672\text{ V}$  is the potential held by the front of the first plate,  $VD_2 = -912\text{ V}$  is the voltage applied to the back of the first plate and to the front of the second plate, and  $VD_3 = -180\text{ V}$  is the potential held by the front of the second plate. When an ion hits one of the microchannels, it starts a cascade of electrons that propagates through the channel. As the electrons emerge from the channels of the second plate, they hit a metal anode and produce a small current pulse that can be detected.

## 4 Interfacing, Data Acquisition and Data Analysis

### 4.1 Introduction

This chapter contains a description of the hardware, software and analysis procedures required to obtain mass spectra, ion yield curves and appearance energies for fragment ions. Time-of-flight spectrometry requires precise pulsing of the electron gun, the ion extraction into the mass spectrometer, and the multichannel scaler to record accurate mass spectra.

The pulsing sequence used in this research is described in section 4.2. The amplification and discrimination of the pulses produced by the microchannel plate detector is discussed in section 4.3. The time calibration of the multichannel scaler used for collecting single mass spectra is described in section 4.4.

A total of seven LabVIEW programs are used for setting the electron gun, for acquiring mass spectra and for obtaining ion yield curves and appearance energies. These programs are displayed in section 4.5.

### 4.2 Pulsing and Timing

For this research, the width and delay of the electron gun pulse, the ion extraction pulse and the multichannel scaler trigger must be precisely set with respect to each other for an accurate mass spectrum to be produced. A DG535 Digital Delay Generator from Stanford Research Systems is used to provide these precise widths and delays, and is employed here to trigger pulsing and data acquisition. The delay generator produces a trigger pulse, T0, four precisely-timed delay channels A, B, C, and D, and four independent pulse channels AB,  $\overline{AB}$ , CD and  $\overline{CD}$ . The delay channels can be delayed from 0 to 1000 ns, and the delay resolution for each channel is 5 ps. The delay generator can provide four pulse shapes; TTL, ECL, NIM or VAR level pulses. The pulses can be set to be delivered into 50  $\Omega$  or high impedance loads, and can be set normal or inverted.

Delays can be set for A, B, C and D, but not the width, see Figure 4.1. The widths of AB and CD can be set by adjusting the delays of A and B, and C and D. The delays can be triggered either internally using the internal rate generator, or externally using an external source. All generator channels are pulsed relative to T0 as it signifies the start of a timing cycle, which can also be triggered internally or externally. The first delay from the

independent pulse channels determines the leading edge of the pulse, and the second delay specifies the trailing edge. Delay channels can be set relative to T0 and to each other.

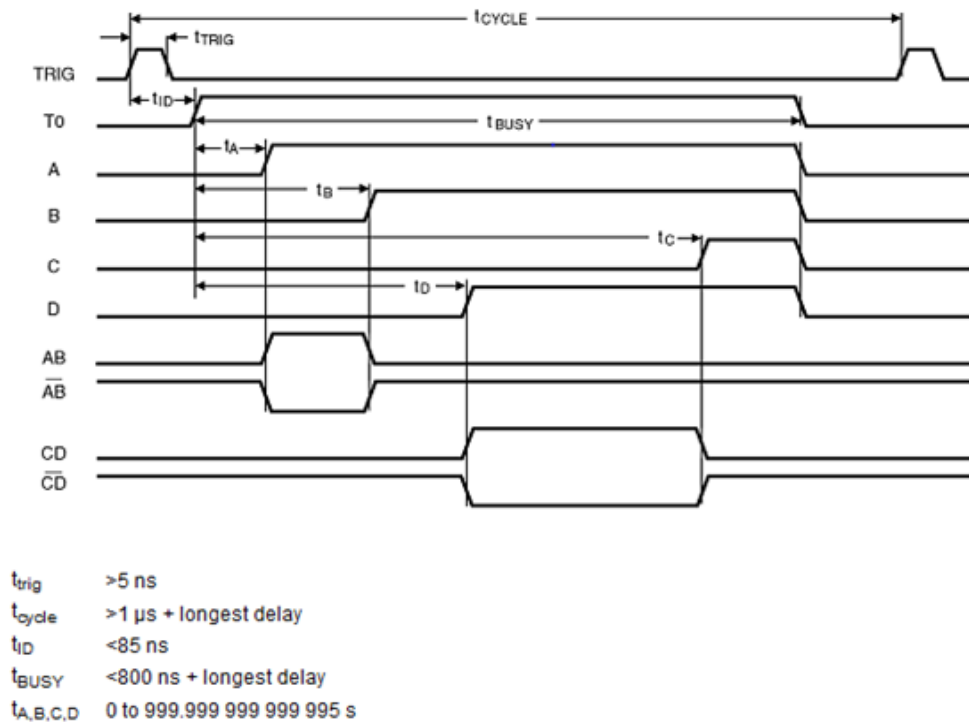


**Figure 4.1** The DG535 digital delay generator timing diagram [117].

Here, when the delay at A is adjusted, the output of B is carried with it, allowing for A and B to establish a pulse for which the width is held fixed as the delay is varied. This example also indicates that the AB output will deliver a 1.37  $\mu\text{s}$  pulse, and the CD output will deliver a 0.1  $\mu\text{s}$  pulse. For the DG535 Digital Delay Generator, 800 ns after the delays have timed out, all four channels A, B, C and D will return low, despite the delay values chosen. This signifies that the delay generator is prepared to start a new timing cycle. AB and CD will go high during the time interval between their associated channels, and  $\overline{AB}$  and  $\overline{CD}$  will return pulses of identical timing and inverted amplitude. The delay values can be set using a menu interface on the delay generator [117]. The delay and pulse settings used in this research are shown in Table 4.1;

<b>A</b>	=	<b>T0</b>		
<b>B</b>	=	<b>D</b>	+	<b>0.27 <math>\mu\text{s}</math></b>
<b>C</b>	=	<b>A</b>	+	<b>1.00 <math>\mu\text{s}</math></b>
<b>D</b>	=	<b>C</b>	+	<b>0.10 <math>\mu\text{s}</math></b>

**Table 4.1** The delays on A, B, C and D used in this research.

Applying these settings, CD is used to pulse the electron gun, AB is used to switch the extraction voltage off and on, and B is used to trigger the start of the multichannel scaler. To avoid noise in the first few channels of the multichannel scaler, the B pulse is delayed by  $1 \mu\text{s}$ , as seen in Figure 4.2, using an ORTEC 416 A Gate and Delay Generator.

As the pulses provided by the digital delay generator are standard TTL pulses, two remote pulsers are used to generate pulses of the correct amplitude. The inputs for each of the remote pulsers are 12 V in order to power the circuit, a base voltage, a pulse voltage and a TTL input pulse. The outputs of both remote pulsers are seen in Figure 4.2.

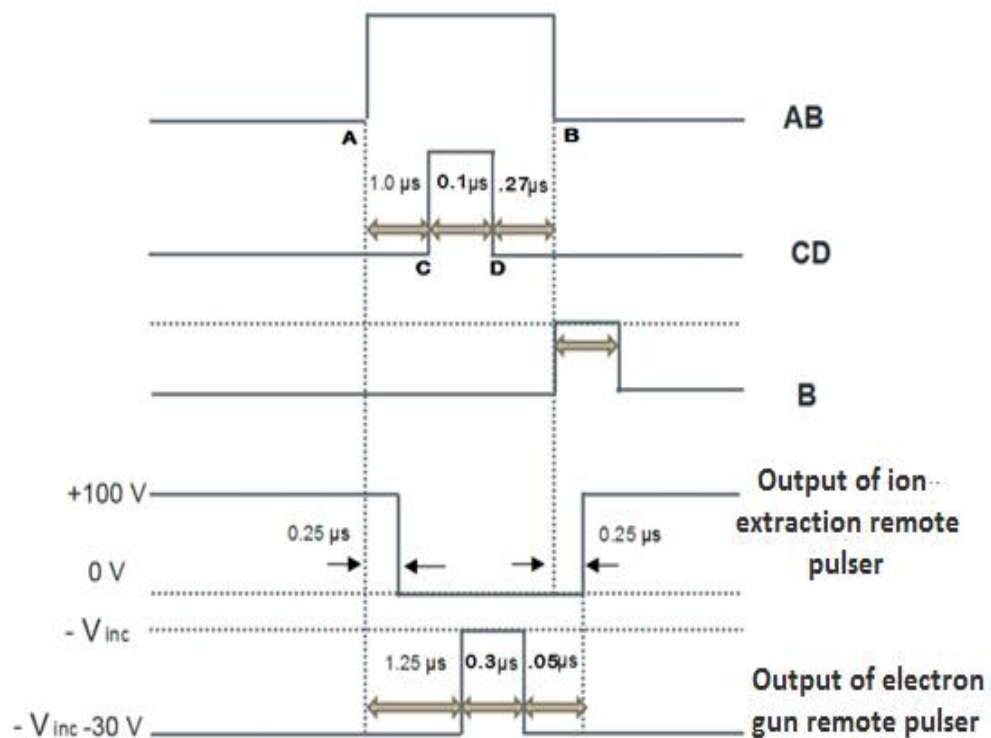


**Figure 4.2** The DG535 timing diagram corresponding to this experiment.

In this experiment, particles in the expansion chamber pass through a skimmer, enter the collision chamber, and are situated between two extraction plates. The first extraction plate, A1, is held at  $+100 \text{ V}$  for most of the duration of the experiment to allow for continuous extraction. Before ionisation can take place, A1 must be brought to ground. The electron gun is pulsed  $1 \mu\text{s}$  later and ionisation occurs.

The pulsing of the electron gun is provided by the electron gun remote pulser, and requires a Farnell L30B stabilised power supply to set the bias voltage, a Farnell E30/2 power supply to provide the pulsed voltage, a 12V input to power the unit, and an input for the

CD pulse to trigger the unit. Once the unit is triggered, the grid element voltage of the electron gun,  $V_{\text{GRID}}$ , is pulsed. Before pulsing,  $V_{\text{GRID}}$  is held at -30 V, relative to the zero of the gun, preventing electrons from entering the gun. Once pulsing begins,  $V_{\text{GRID}}$  becomes less negative, electrons enter the electron gun and ionisation takes place in the interaction region. With a 0.1  $\mu\text{s}$  input pulse, the electron gun remote pulser produces an output pulse with a width of 0.3  $\mu\text{s}$ .

After 0.05  $\mu\text{s}$ , the extraction voltage is returned to +100 V by the ion extraction remote pulser. The restoration of the extraction voltage is provided by an extraction pulser unit connected to A1. This unit is triggered by the AB output of the delay generator, and requires DC voltage supplies to define low and high limits for AB, a 12 V supply to power the unit, and a trigger pulse to time AB. When the extraction voltage is restored to +100 V, the positive fragment ions are extracted into the time-of-flight tube.

### **4.3 Amplification and Discrimination of Detector Pulses**

The signal produced by the microchannel plate detector when an ion hits it must be amplified and discriminated before data acquisition can occur. To do this, the signal is passed into an ORTEC 9327 1-GHz Amplifier and Timing Discriminator which is suitable for use with the millivolt signals produced by microchannel plate detectors such as the detector used in this experiment. It can handle pulses in the height range of 0 to -30 mV, or from 0 to -150 mV full scale, and in the width range of 250 ps to 5 ns. It has a 1 GHz bandwidth to reduce the noise and rise time contributions to timing jitter on the detector pulses. The device has an LED that indicates when the pulse amplitude has exceeded the limit of the amplifier [118].

To eliminate the noise from the signal, the discriminator level of the ORTEC 9327 is manually adjusted at the front of the device [118]. In this experiment, the discriminator level was set at -0.0247 mV. This threshold value was selected by monitoring the background signal between the mass peaks of a single mass spectrum. The discriminator puts out a logic pulse when the input signal meets the threshold value [119]. This pulse is connected to the STOP input of the multichannel scaler.

## 4.4 Multichannel Scaler

The multichannel scaler (MCS) card used in this research is the 7886S Multichannel Scaler Card by FAST ComTEC. It is a PC card used to accumulate time-of-flight spectra by counting incoming pulses in successive time channels. The card can accept one event in every channel and can handle up to 2 GHz of peak count rates. It has a dynamic range of up to  $2^{37}$  channels, enabling sweeps of 68.7 s with a time resolution of 430 ps/channel [120].

The inputs and outputs on the MCS card are STOP IN, START IN, ABORT IN, SYNC OUT and DIGITAL IN. The card also has a THRESHOLD ADJUST screw that allows the discriminator level of the START, STOP and ABORT pulses to be varied. The B output of the DG535 is connected to START IN of the MCS card, triggering it to start scanning. The multichannel plate detector output is connected to the input of the amplifier and timing discriminator, and NIM OUT of the ORTEC 9327 is connected to the STOP IN of the MCS card. This ensures that the signal from the detector can be registered as a count at the relevant binning location of the MCS card.

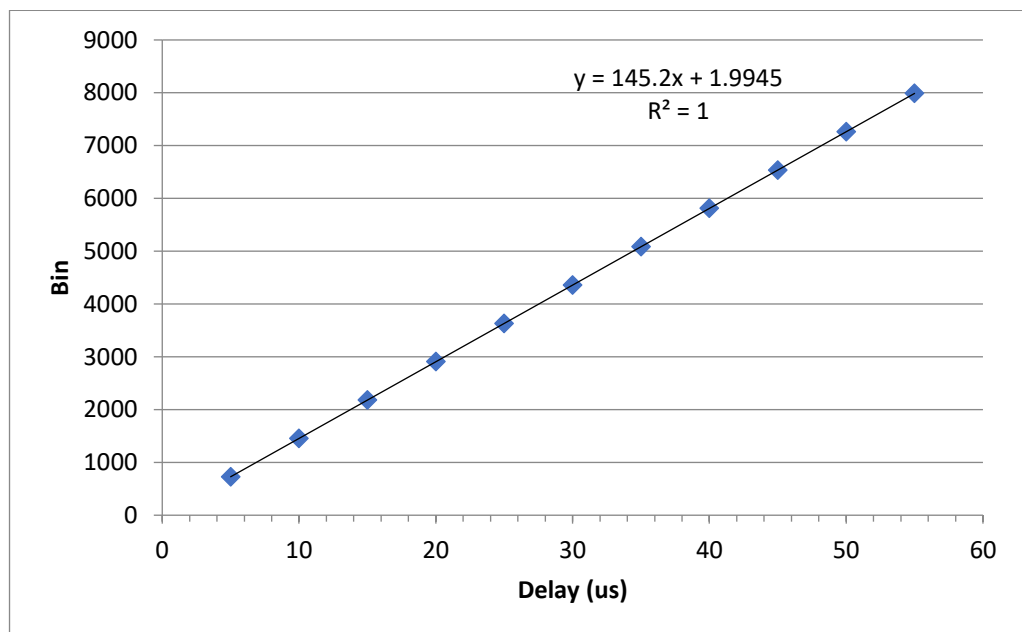


**Figure 4.3** Calibration plot for the MCS card.

The DG535 Digital Delay Generator is also used to calibrate the MCS. The card uses a phase-locked loop oscillator that is set to 2 GHz, assuring the time resolution of each channel is less than 500 ps. However, this frequency can vary, so the digital delay generator is used as an external reference by which to calibrate the time per channel,

where the accuracy of the delay generator is 5 ps. A start and a stop pulse were sent from the delay generator to the card and the delay in the pulses was varied over 55  $\mu\text{s}$  in steps of 5  $\mu\text{s}$ . The corresponding bin number was recorded, and Figure 4.3 was produced.

The best fit line was drawn through these points and the slope was found to be  $145.2003 \pm 0.0002$  bins/ $\mu\text{s}$ , yielding a time resolution of  $430.4400 \pm 0.0005$  ps/channel. For the measurements on anthracene, a bin width of 64 channels was used, corresponding to  $27.54816 \pm 0.00003$   $\mu\text{s}/\text{bin}$ .

## **4.5 Data Acquisition Software**

### **4.5.1 Electron Gun**

Two LabVIEW programs are used to check the correct operation of the electron gun. The program *set-gun-V-myDAQ.vi* is used to set the electron impact energy at a fixed value so that the voltages on the lens elements can be adjusted for optimum Faraday cup current. A control potential between 0 and 5 V is sent to the KEPCO APH500 programmable power supply that controls the electron impact energy (see section) and the program permits the user to view if the output voltage from the power supply is within this range. The control potential is supplied by a National Instruments myDAQ data acquisition device that uses LabVIEW-based software.

The second program, *gun-test-myDAQ.vi*, was developed to test the operation of the gun when the electron impact energy is varied. The program plots the total current on the Faraday cup as a function of electron impact energy by measuring the current on both the inner and outer cup. The myDAQ is used to set the electron impact energy and to measure the current on the cup. The plot is displayed on the front panel of the program, along with controls to allow the user to select the start voltage, end voltage, step size, and the delay between energy values.

### **4.5.2 Acquiring Mass Spectra**

Two LabVIEW-based programs are used to obtain accurate mass spectra. The program *getspectrum-3-5.vi* was developed by Dr. Peter van der Burgt and Dr. Marcin Gradziel to acquire a single mass spectrum which can be viewed in real-time. The program records and displays data from the MCS card and an assessment of the condition of the card, system and data can be done before multiple scans are initiated. We are able to use

LabVIEW-based programs to interact with the MCS card due to a modification to the code provided by Fast ComTEC to access the functions and settings of the card. This modification was performed by Dr. Marcin Gradziel. The program consists of a node to initialise the card and a node that handles the measurement of data. The latter reads in four user-selected values from the front panel: time range (number of channels), bin width (number of bins per channel), update timeout and number of sweeps. A sweep is a record collected following a single trigger of the MCS. The number of completed sweeps can be viewed via an indicator on the front panel and once all sweeps are complete a time of flight spectrum is obtained. The spectrum can then be saved to a text file by selecting the Save button on the front panel.

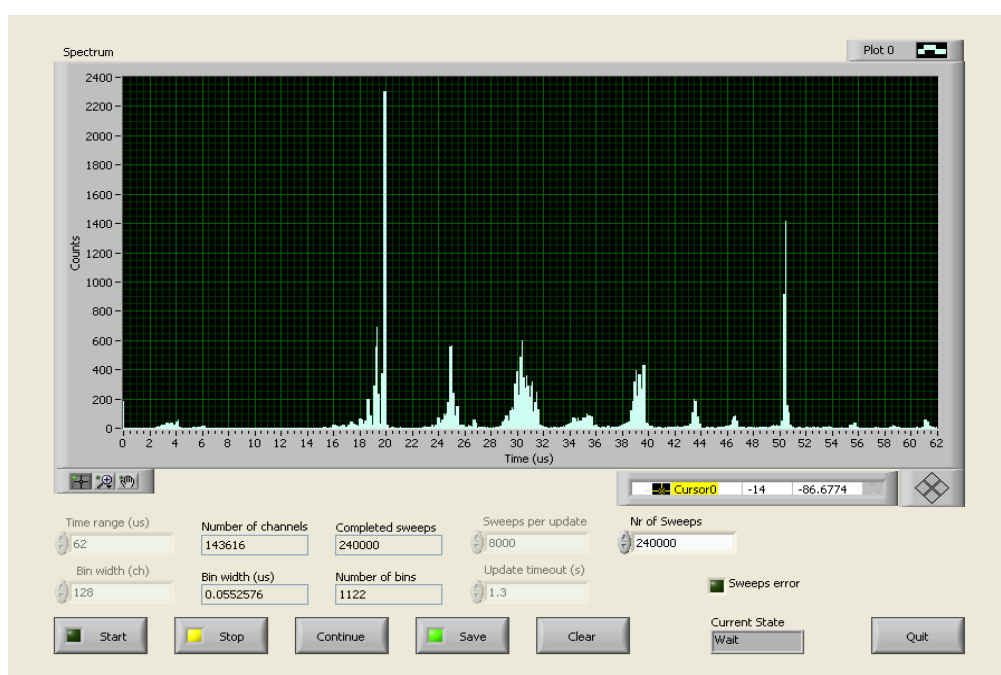


**Figure 4.4** Screenshot of the front panel of getspectrum-3-5.vi. The compound shown is cytosine.

The second program, *Spectra-vs-E-v7.vi*, was developed by Gerard Barrett [121], and the modified MCS card files were supplied by Dr Marcin Gradziel. The program is used to acquire multiple mass spectra as a function of impact energy by recording data from the MCS card and sequentially producing mass spectra as the impact energy is incremented. A delay of 2 s was introduced after each energy increment to allow the gun to stabilise. In this experiment, 200 mass spectra of 240,000 sweeps each were obtained with an electron pulse rate of 8 kHz.

Figure 4.5 shows the front panel of the program, which displays the real-time accumulation of mass spectra. Controls permit the user to access MCS card settings such

as time range, number of sweeps and bin width. Indicators show the current state of the card. There are also controls for the number of cycles, the starting and stopping energy and the energy step size. A cycle involves a single pass through all the electron impact energies. The number of cycles accumulated was 23, where each cycle contains multiple sweeps of the MCS card at a specific impact energy.

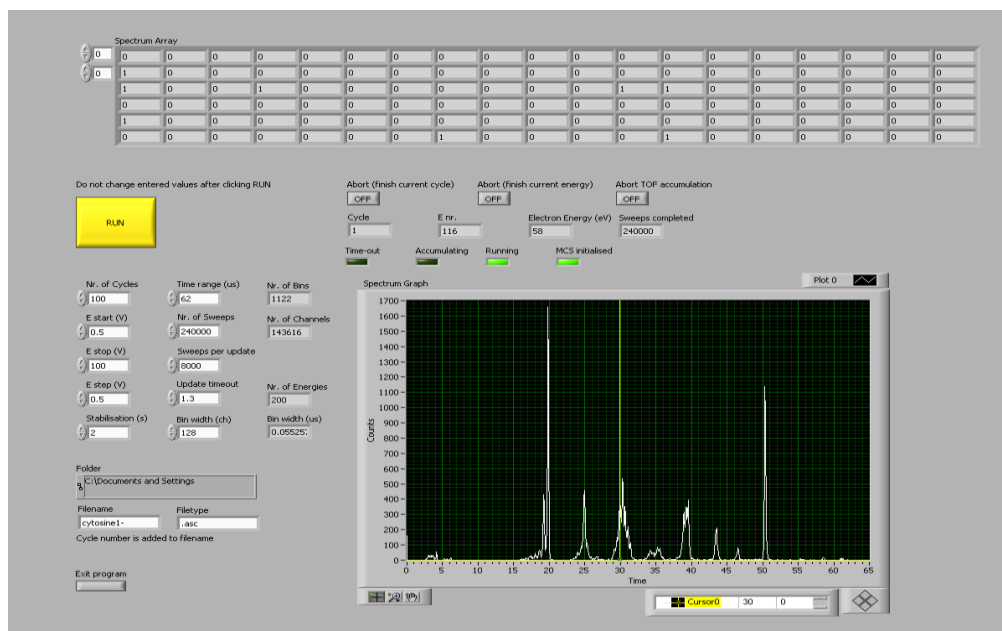


**Figure 4.5** Screenshot of the front panel of Spectra-vs-E-v7. The compound shown is cytosine.

At the end of each cycle, a 2D array of mass spectra as a function of impact energy is written to a file. The accumulation of these cycle files enables ion yield curves to be produced for each fragment and the inspection of yields of specific masses at specific impact energies as a function of cycle number. Further, we can use these measurements to observe time-dependent effects that occur during the experiment, such as a decrease in intensity of the molecular beam.

### 4.5.3 Gaussian Peak Fitting Program

Ion yield curves are curves which display the fragmentation sequences of fragments in the mass spectra as a function of incident energy. When analysed, they can provide information about the fragmentation pathways and processes occurring in the formation of each fragment. It is necessary to accurately calculate the peak area of a fragment before its ion yield curve can be produced. Dr Peter van der Burgt has developed two LabVIEW VIs, *Gaussians2.vi* and *Gaussians-ab2.vi*, which calculate the areas of series of adjacent mass peaks in the mass spectra by fitting them with a sequence of normalised Gaussians.

The first program uses a single width,  $a$ , for all of the peaks in the group, whereas the second program allows the use of two different widths  $a$  and  $b$ .

The programs use the Levenberg-Marquardt algorithm to determine a set of parameters that best fits the set of input points. The best fit is expressed by a non-linear function and the input data is extracted from the output file of *Spectra-vs-E-v7.vi* which is a 2D array of ion yields as a function of impact energy and bin number. For each set of adjacent peaks, the part of the mass spectrum associated with that set is extracted and loaded into the program.

The sequence of normalised gaussians in *Gaussians2.vi* is given by the following formula:

$$f(x) = \sum_{i=1}^n \frac{C_i}{a\sqrt{\pi}} \exp\left(-\left(\frac{x-p-\Delta_i}{a}\right)^2 + d\right) \quad (23)$$

where  $C_i$  is the area of peak,  $a$  is the peak width,  $x$  is the bin number and  $p$  is the position of the largest peak in the group.  $\Delta_i$  is the difference between the position of a peak  $i$  and the position of the biggest peak ( $\Delta_i$  is zero for the biggest peak in the group) and  $d$  is the background. The normalising factor  $\frac{1}{a\sqrt{\pi}}$  assures that the area under a single gaussian is 1. Figure 4.6 shows the front panel of the program.

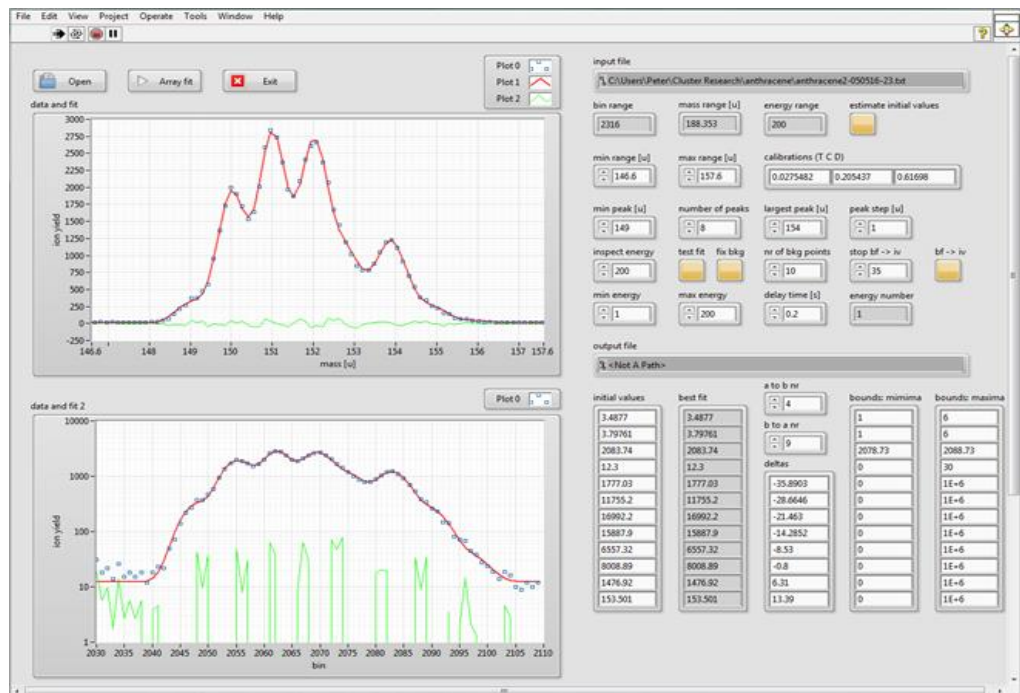


**Figure 4.6** Screenshot of the front panel of Gaussians-ab2.vi. Input file is for anthracene.

Before fitting can begin, the user must select inputs for the following controls and arrays:

<b>Min and max range controls</b>	These controls are used to select the mass range in the mass spectra to be fitted.
<b>Min peak control</b>	The user selects the mass of the first peak on the left so the program will fit the correct number of peaks at the correct mass values.
<b>Number of peaks control</b>	The user selects the number of peaks to be fitted within the chosen mass range.
<b>Largest peak control</b>	The atomic mass of the peak in the mass range with the highest abundance at 200 eV is selected here. This is to aid with convergence at lower impact energies.
<b>Peak step control</b>	This control allows the user to select the mass unit separation between each Gaussian. This can be adjusted for fitting first, second and third integer masses
<b>Inspect energy control</b>	Before fitting, the inspect energy control is set to the highest energy value. Then, when the fitting begins, the program iteratively performs fits for successively lower energies. This control also allows the user to view the fit result at a specific energy when the fitting program is not running.
<b>Nr of bkg points control</b>	This control allows the user to select a specific number of points that the program will use to calculate the average background. The program then selects

	that number of points from those with the lowest ion yield.
<b>Min energy control</b>	The user sets the energy that the fitting stops at with this control.
<b>Max energy control</b>	The user sets the energy that the fitting begins at with this control.
<b>Delay time control</b>	This control is used to reduce the speed with which the program steps through the electron energies, allowing the user to inspect each fit in real time.
<b>Initial values array</b>	<p>The inputs for this array are the estimates of the peak areas, the position of peak <i>i</i>, the background, and the width(s) of the peaks in the mass range. The array size will depend on the number of peaks to be fit, which is set using the number of peaks control.</p> <p>These array values are updated to the values in the <i>best fit</i> parameters array, which This array stores the best fit values for each electron impact energy in an array that contains all of the best fit parameters. This array is then saved to a file when the program completes all fits. This file contains the data used to produce ion yield curves for each group of peaks in succession, for all electron impact energies.</p> <p>When the <i>estimate initial values</i> control is selected, the program will estimate the values for the <i>initial values</i> array.</p>

<b>Stop bf -&gt; iv controls</b>	These controls permit the user to select an impact energy below which the parameters in the initial parameters array remain constant, and are not updated to the best fit parameters, which are calculated by the program. This can delay convergence issues during fitting.
----------------------------------	--

The values of  $\Delta_i$  for each peak in the mass range are held in the *deltas* array, whose values are calculated by the program when the *test fit* control is selected. However, the user can manually make minor adjustments to the values (typically much less than 1 u) before fitting in order to slightly improve the fit.

Due to the low yield and background count at lower impact energies, convergence problems near threshold may occur. The user may need to redo the fits near threshold over a smaller energy range and reduced the number of peaks where required. It is also possible to give *a*, *b* and *p<sub>i</sub>* fixed values. If a fit fails to converge, the user can view this and reset the fit with altered fit variables that will assist with convergence.

#### 4.5.4 Appearance Energy Program

To establish the appearance energy of each fragment, a LabVIEW program, *Onsets.vi*, was developed by Dr Peter van der Burgt. A file containing all the ion yield curves is read in to this program and the user can select which ion yield curve to fit and the range of data points near threshold to use in the fit. A tab structure allows the fittings of 1, 2 or 3 onsets. This is done using the Levenberg-Marquardt algorithm. For a single onset, the measured curve was fit using the function  $P(E)$ , which assumes a power law to describe the threshold behaviour, convoluted with a Gaussian function to represent the electron beam resolution:

$$P(E) = \int_{-\infty}^{\infty} f(\varepsilon)g(E - \varepsilon)d\varepsilon + d \quad (24)$$

$$f(\varepsilon) = 0 \quad \text{if } \varepsilon \leq E_1$$

$$f(\varepsilon) = c(\varepsilon - E_1)^p \quad \text{if } \varepsilon > E_1$$

$$g(\varepsilon) = \frac{1}{a\sqrt{\pi}} \exp\left(\frac{-\varepsilon}{\sigma}\right)^2$$

For two onsets

$$\text{if } \varepsilon > E_2$$

$$f(\varepsilon) = c_1(\varepsilon - E_1)^{p_1} + c_2(\varepsilon - E_2)^{p_2} \quad (25)$$

where  $E_1$  and  $E_2$  are the onsets,  $\sigma$  is the Gaussian beam width,  $d$  is the background,  $c$  is the scaling factor and  $p$ ,  $p_1$  and  $p_2$  are power values.

Figure 4.7 shows the front panel of the program. Here, starting values for the variables are user selected. Controls for the minimum and maximum energy number that can be displayed in the plots are present as a visual aid to the selection of the fit parameters. The uncertainty of each parameter and the uncertainty of the entire fit can also be viewed via indicators. Once the curve has been fit, the model data, as well as the input data, can be saved to a text file which can be used to generate a graph if needed.

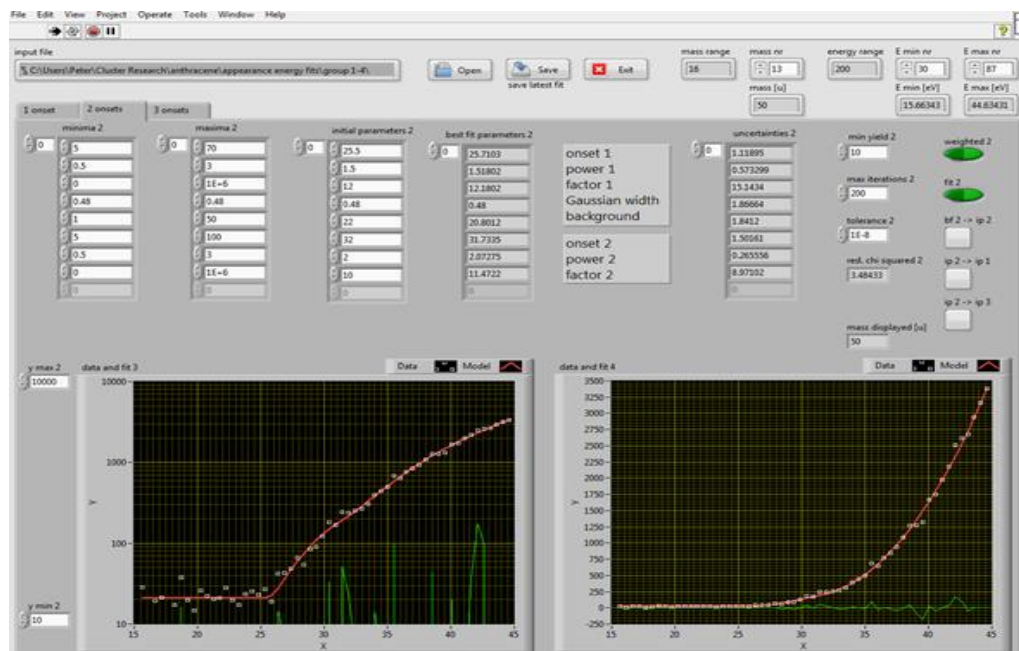


**Figure 4.7** Screenshot of the front panel of Onsets.vi. Input file is for anthracene.

## 5 Experimental Results

### 5.1 Introduction

This chapter will look at the experimental data obtained for anthracene during this research. A discussion of the peaks, peak assignments and possible fragments associated with our mass spectrum is presented in Section 5.2 of this chapter. For each group, the fit with Gaussians and their ion yield curves are displayed and examined in Section 5.3. The appearance energies for a number of fragment ions of sufficient yield have been determined and are displayed in an appearance energy graph in Section 5.4. In the remainder of this chapter, we will identify groups of peaks by the number of carbon atoms contained in the fragments.

### 5.2 Anthracene Mass Spectrum

Figure 5.1 shows the main groups in our mass spectrum for anthracene, and Figure 5.2 shows our entire mass spectrum.

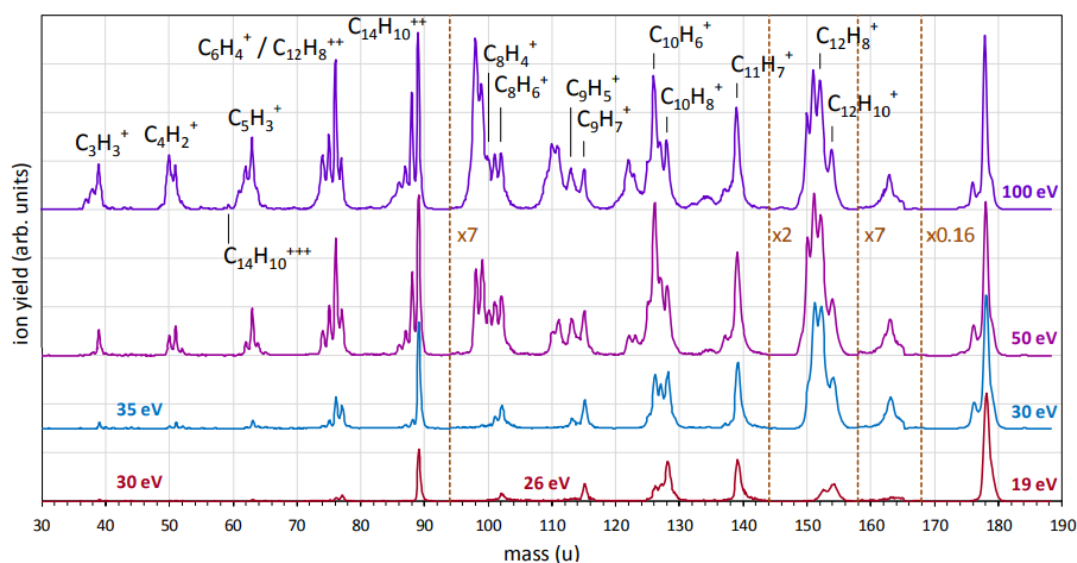


**Figure 5.1** The main groups in our mass spectrum for anthracene.

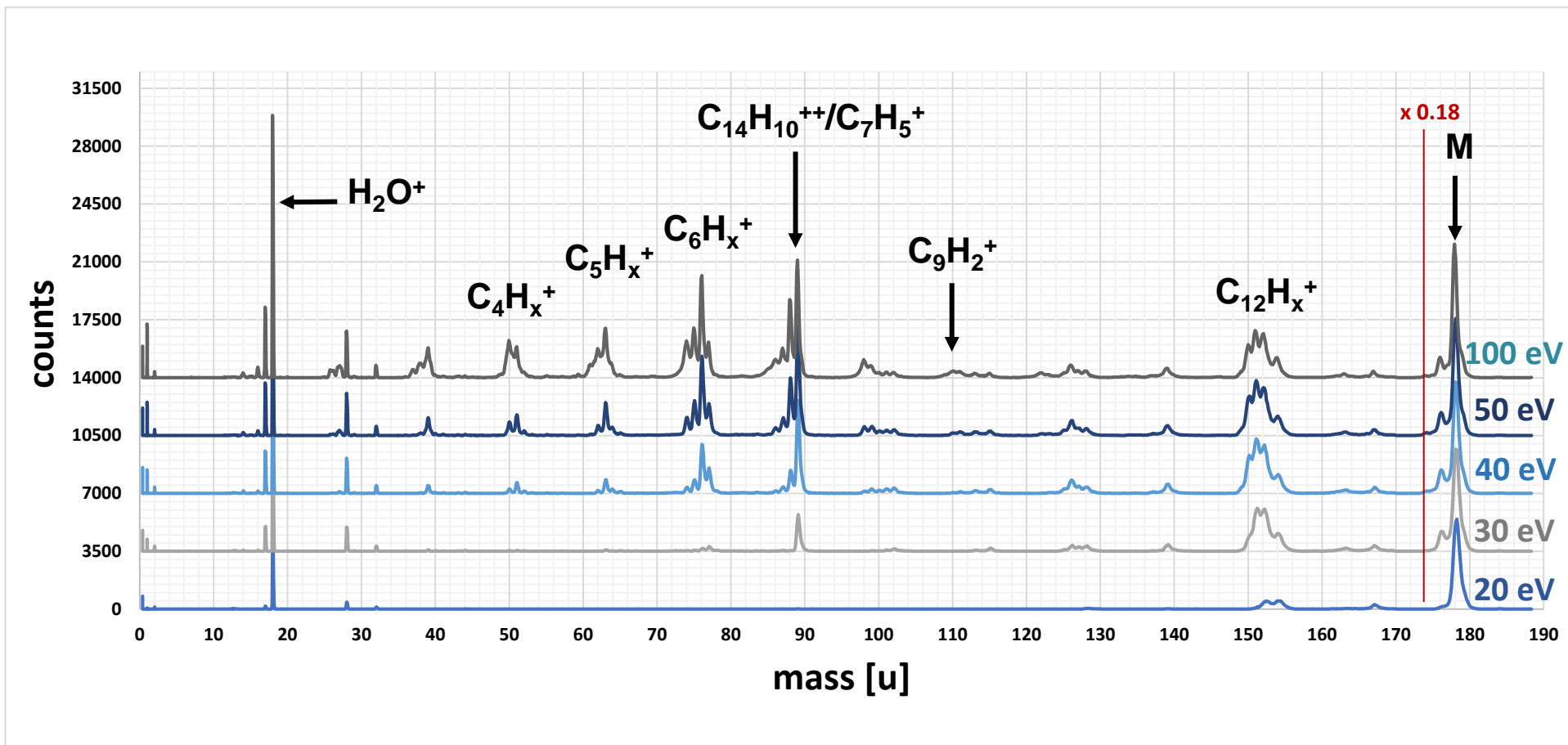


Figure 5.2 Our mass spectrum for anthracene.

Group No.	Mass Range	Identified Peaks [u]	Possible Fragments
Group 1	12 – 15 u	12 13 15	C <sup>+</sup> CH <sup>+</sup> CH <sub>3</sub> <sup>+</sup>
Group 2	25 – 32 u	26 27 28 29 32	C <sub>2</sub> H <sub>2</sub> <sup>+</sup> C <sub>2</sub> H <sub>3</sub> <sup>+</sup> N <sub>2</sub> C <sub>2</sub> H <sub>5</sub> <sup>+</sup> O <sub>2</sub> <sup>+</sup>
Group 3	36 – 41 u	36 37 38 39 40 41	C <sub>3</sub> <sup>+</sup> C <sub>3</sub> H <sup>+</sup> C <sub>3</sub> H <sub>2</sub> <sup>+</sup> C <sub>3</sub> H <sub>3</sub> <sup>+</sup> C <sub>3</sub> H <sub>4</sub> <sup>+</sup> C <sub>3</sub> H <sub>5</sub> <sup>+</sup>
Group 4	49 – 53 u	49 50 51 52 53	C <sub>4</sub> H <sup>+</sup> C <sub>4</sub> H <sub>2</sub> <sup>+</sup> C <sub>4</sub> H <sub>3</sub> <sup>+</sup> C <sub>4</sub> H <sub>4</sub> <sup>+</sup> C <sub>4</sub> H <sub>5</sub> <sup>+</sup>
Group 5	59.33 – 65 u	59.33 61 61.5 62 62.5 63 63.5 64 64.5 65	C <sub>14</sub> H <sub>10</sub> <sup>3+</sup> C <sub>5</sub> H <sup>+</sup> C <sub>10</sub> H <sub>3</sub> <sup>2+</sup> ? C <sub>5</sub> H <sub>2</sub> <sup>+</sup> C <sub>10</sub> H <sub>5</sub> <sup>2+</sup> ? C <sub>5</sub> H <sub>3</sub> <sup>+</sup> C <sub>10</sub> H <sub>7</sub> <sup>2+</sup> ? C <sub>5</sub> H <sub>4</sub> <sup>+</sup> C <sub>10</sub> H <sub>9</sub> <sup>2+</sup> ? C <sub>5</sub> H <sub>5</sub> <sup>+</sup>

**Table 5.1** The groups of peaks, and possible fragments associated with groups 1 to 5.

Groups 1, 2, 3, and 4 are composed of broadened peaks. Because the peaks are well separated, ion yields were obtained by summing over the appropriate bin ranges. Groups 3 and 4 were fitted using third integer masses, although the yield of these groups is too high to have primary contributions from triply charged fragments. Ion yield curves for these groups were determined by adding the third-integer yields to the integer yields. For instance, the 38.67 u and the 39.33 u yields were added to the 39 u yield to obtain the 39 u ion yield curve. Although group 5 was fitted using half-integer masses, the peaks within this group may well be broadened peaks that do not have any contribution from doubly ionised fragments. This group does, however, have a very weak peak at 59.333 u, indicating the presence of the anthracene trication.

Group No.	Mass Range	Identified Peaks [u]	Possible Fragments
Group 6	73 – 78 u	73 74 74.5 75 75.5 76 76.5 77 77.5 78	$C_6H^+$ $C_6H_2^+$ $C_{12}H_5^{2+}$ $C_6H_3^+/C_{12}H_6^{2+}$ $C_{12}H_7^{2+}$ $C_6H_4^+/C_{12}H_8^{2+}$ $C_{12}H_9^{2+}$ $C_6H_5^+/C_{12}H_{10}^{2+}$ $C_{11}^{13}CH_{10}^{2+}$ $C_6H_6^+$
Group 7	84 – 90 u	84.5 85 85.5 86 86.5 87 87.5 88 88.5 89 89.5 90	$C_{14}H^{2+}$ $C_7H^+$ $C_{14}H_3^{2+}$ $C_7H_2^+$ $C_{14}H_5^{2+}$ $C_7H_3^+/C_{14}H_6^{2+}$ $C_{14}H_7^{2+}$ $C_7H_4^+ / C_{14}H_8^{2+}$ $C_{14}H_9^{2+}/C_{13}^{13}CH_8^{2+}$ $C_7H_5^+/C_{14}H_{10}^{2+} (/C_6^{13}CH_4^+ /C_{13}^{13}CH_9^{2+})$ $C_{13}^{13}CH_{10}^{2+}$ $C_7H_6^+$
Group 8	96 – 104 u	97 98 99 100 101 102 103	$C_8H^+$ $C_8H_2^+$ $C_8H_3^+$ $C_8H_4^+$ $C_8H_5^+$ $C_8H_6^+$ $C_8H_7^+/C_7^{13}CH_6^+$
Group 9	107 – 117 u	109 110 111 112 113 114 115 116	$C_9H^+$ $C_9H_2^+$ $C_9H_3^+$ $C_9H_4^+$ $C_9H_5^+$ $C_9H_6^+$ $C_9H_7^+$ $C_9H_8^+$

**Table 5.2** The groups of peaks, and possible fragments associated with groups 6 to 9.

Groups 6 and 7 were fitted using Gaussians at half-integer masses because these groups appear to contain contributions from doubly ionised fragments. Group 7 may contain singly-charged fragments with 7 carbon atoms and doubly-charged fragments with 14 carbon atoms. The yield ratios for 89.5 u and 89 u and for 77.5 u and 77 u indicate that

the largest contributions to the ion yields in these groups come from doubly charged fragments, see discussion in section 5.3.3.

Group No.	Mass Range	Identified Peaks [u]	Possible Fragments
Group 10	119 – 130 u	120 121 122 123 124 125 126 127 128 129	$C_{10}^+$ $C_{10}H^+$ $C_{10}H_2^+$ $C_{10}H_3^+$ $C_{10}H_4^+$ $C_{10}H_5^+$ $C_{10}H_6^+$ $C_{10}H_7^+$ $C_{10}H_8^+$ $C_{10}H_9^+/C_9^{13}CH_8^+$
Group 11	133 – 141 u	133 134 135 137 138 139 140	$C_{11}H^+$ $C_{11}H_2^+$ $C_{11}H_3^+$ $C_{11}H_5^+$ $C_{11}H_6^+$ $C_{11}H_7^+$ $C_{11}H_8^+/C_{10}^{13}CH_7^+$
Group 12	148 – 156 u	149 150 151 152 153 154 155	$C_{12}H_5^+$ $C_{12}H_6^+$ $C_{12}H_7^+$ $C_{12}H_8^+$ $C_{12}H_9^+$ $C_{12}H_{10}^+$ $C_{11}^{13}CH_{10}^+$
Group 13	161 – 165 u	161 162 163 164	$C_{13}H_5^+$ $C_{13}H_6^+$ $C_{13}H_7^+$ $C_{13}H_8^+$
Group 14	174 – 180 u	174 175 176 177 178 179 180	$C_{14}H_6^+$ $C_{14}H_7^+$ $C_{14}H_8^+$ $C_{14}H_9^+$ $C_{14}H_{10}^+$ $C_{13}^{13}CH_{10}^+$ $C_{12}^{13}C_2H_{10}^+$

**Table 5.3** The groups of peaks, and possible fragments associated with groups 10 to 14.

All peaks in groups 8 to 14 are exclusively due to single charged fragments. The peak of highest yield in group 8 is at 98 u, and the peak with the lowest appearance energy here

is at 102 u. A peak at 115 u in group 9 points to the occurrence of hydrogen rearrangement, which will be discussed in more detail in section 5.3.4.

Similarly, peaks at 128 u and 129 u in group 10 suggest hydrogen rearrangement. The largest peak in group 10 is at 126 u, indicating the fragment  $C_{10}H_6^+$ . The peak of highest yield in group 11 is positioned at 139 u, and is assigned the fragment  $C_{11}H_7^+$ .  $C_2$  loss in group 12 suggests the occurrence of hydrogen rearrangement, and peaks present at 153 u and 155 u in this group also suggest this.

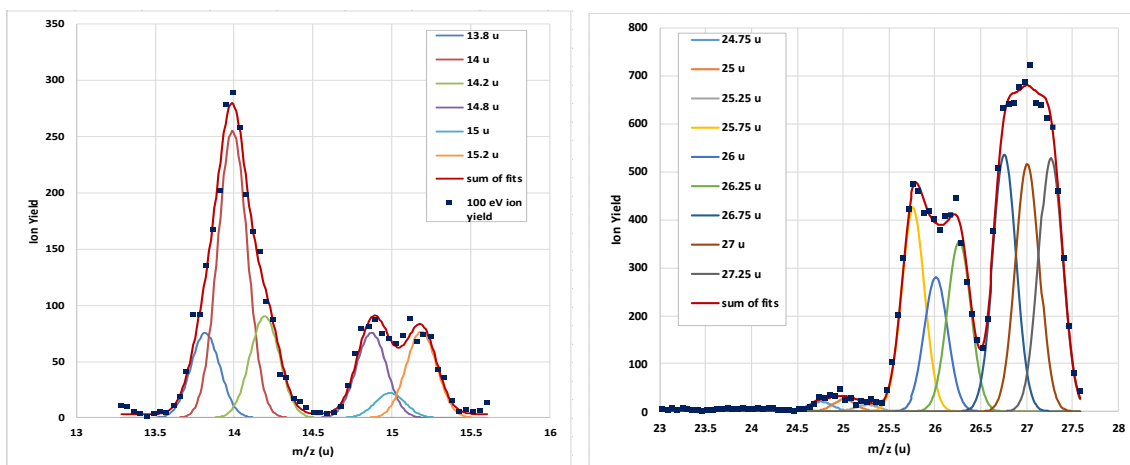
In Group 13, the possible fragments are attributed to CH, H and 2H loss. The peak with the highest yield in this group is at 163 u, and could be due to CH + 2H loss. Group 14 is the parent ion group, containing the masses 172 u to 181 u, and is the group with the highest ion abundance. In figure 5.1. the section of the mass spectrum containing group 14 has been multiplied by a factor of 0.16 to allow for visual comparison with peaks of much lesser yield. The 179 u peak, and the much weaker 180 u peak, are due to isotopes of anthracene.

### **5.3 Gaussian Peak Fitting and Ion Yield Curves**

Taking the mass range of the peaks, the corresponding bin range, the location of the largest peak in each group and the number of identified peaks from our calibrated mass spectrum, we have obtained ion yield curves for each fragment. This was done using the Gaussian fitting procedure described in Chapter 4. Each ion yield curve measures the peak area of a single fragment as a function of electron incident energy.

#### **5.3.1 Groups 1 and 2**

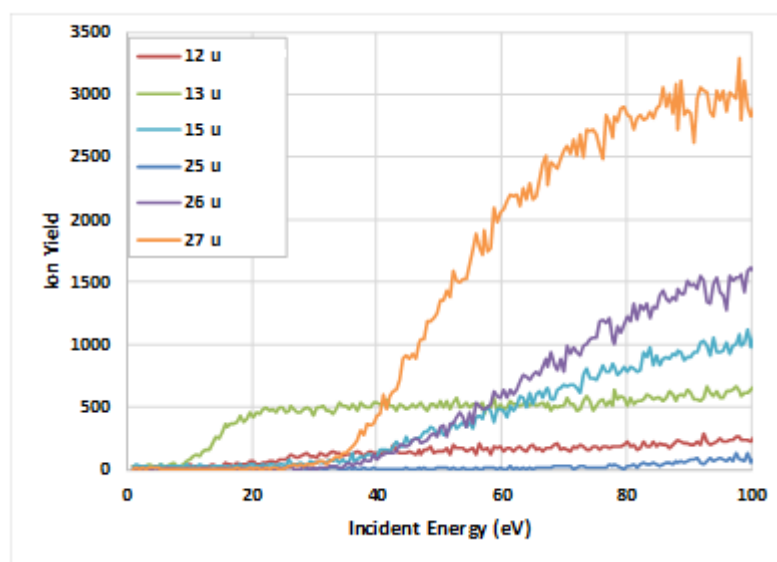
Figure 5.3 compares the Gaussian peak fitting results and the individual peak yields at 100 eV for Groups 1 and 2, the lowest mass groups in our mass spectrum. In both groups, we see clearly broadened peaks. The groups were fitted with fourth and fifth integer masses, respectively, in an attempt to model the broadening of the peaks, but these fit results were not used.



**Figure 5.3** Comparison between the Gaussian peak fitting results and the individual peak yields at 100 eV for Group 1 (left) and Group 2 (right).

In Group 1, the most abundant peak is present at 14 u, corresponding to  $N^+$ . Comparison of mass spectra with the oven on and with the oven off shows that the peaks at 14 u, 16 – 18 u, 28 u and 32 u are due to remnants of water and air in the vacuum chamber. The largest peak in Group 2 is found at 27 u, the fragment  $C_2H_3^+$ . Extensive broadening can be seen in this group. However, the broadening is quite symmetric, suggesting a large kinetic energy spread likely due to singly charged fragments acquiring kinetic energy during fragmentation.

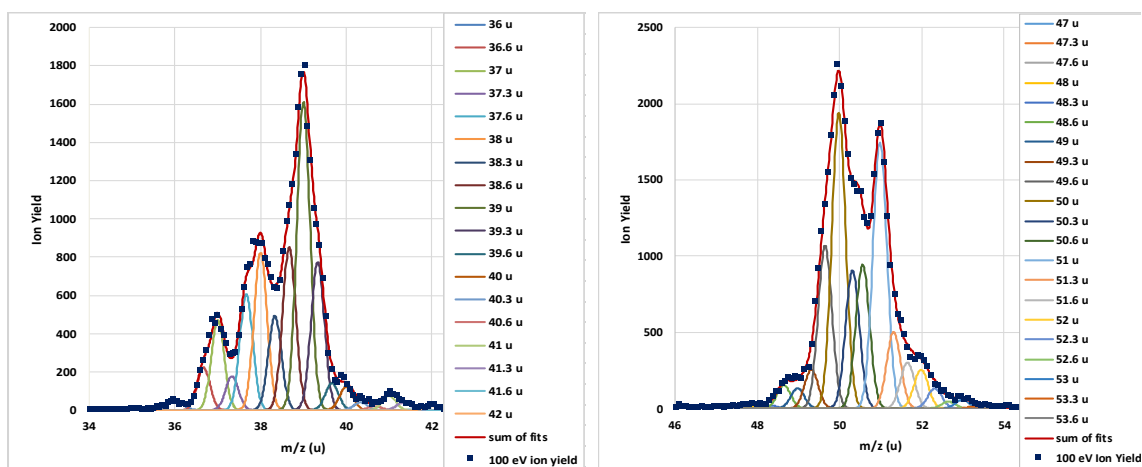
The ion yield curves (in counts) for Groups 1 and 2 are shown in Figure 5.4. All these ion yield curves were determined by summing counts over appropriate bin ranges.



**Figure 5.4** Ion yield curves from groups 1 and 2.

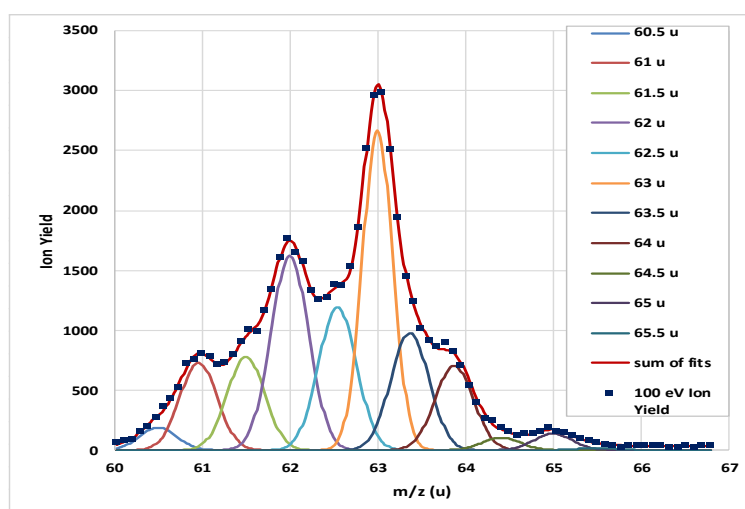
### 5.3.2 Groups 3, 4 and 5

Figures 5.5 and 5.6 compare the Gaussian peak fitting results and the individual peak yields at 100 eV for Groups 3, 4 and 5.



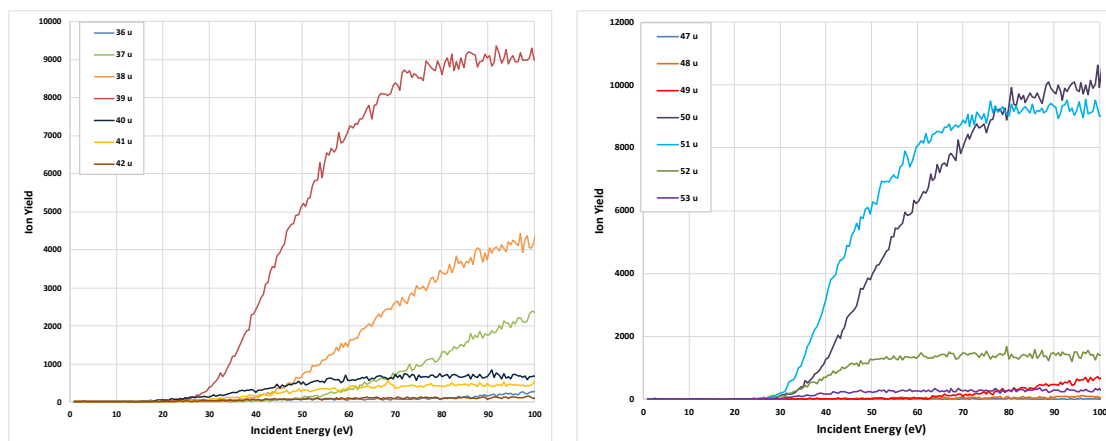
**Figure 5.5** Comparison between the Gaussian peak fitting results and the individual peak yields at 100 eV for Group 3 (left) and Group 4 (right).

The peak of highest yield in Group 3 is present at 39 u, indicating the fragment  $C_3H_3^+$ , and in Group 4 is present at 50 u, suggesting  $C_4H_2^+$ . Both of these groups, though fitted with Gaussians at third-integer masses, are not believed to have any contribution from triply charged fragments. The yields of both groups are too high to suggest this, and the energies required to produce triply charged ions are not represented in the appearance energies determined for the fragments in these groups. The Gaussians at third-integer masses were instead used to account for the broadening of the peaks due to fragments with higher kinetic energies. The most abundant peak in Group 5 is at 63 u, suggesting  $C_5H_3^+$ .



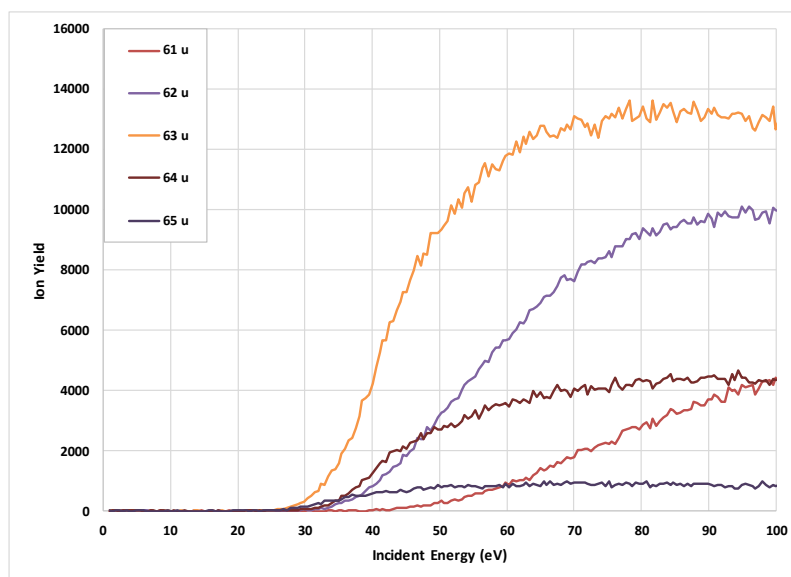
**Figure 5.6** Comparison between the Gaussian peak fitting results and the individual peak yields at 100 eV for Group 5.

The ion yield curves for Groups 3 and 4 are displayed in Figures 5.7. In Group 3, most of the ion yield curves exhibit the same shape, indicating the same fragmentation process. The curve associated with 39 u, however, has a slightly more curved shape, an earlier onset and a higher yield than the other fragments in the group, suggesting its fragmentation process is energetically more favourable than the processes of the other fragments. In Group 4, the ion yield curves mostly exhibit the same shape, although the yield of the 52 u curve levels out earlier than the other curves.



**Figure 5.7** Ion yield curves for Group 3 (left) and Group 4 (right).

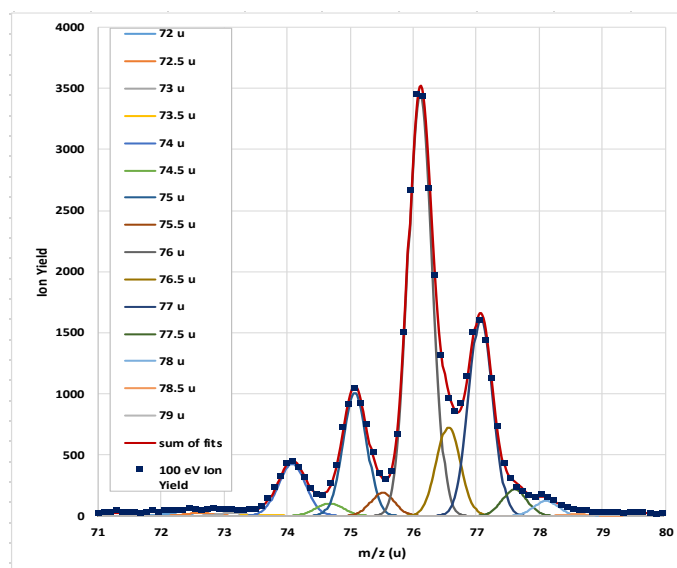
The ion yield curves for Group 5 are displayed in Figures 5.8 below. The appearance energies for the fragments in this group are similar, and most of the curves exhibit approximately the same shape, although the shape of the 64 u curve may indicate the occurrence of another fragmentation process.



**Figure 5.8** Ion yield curves for Group 5.

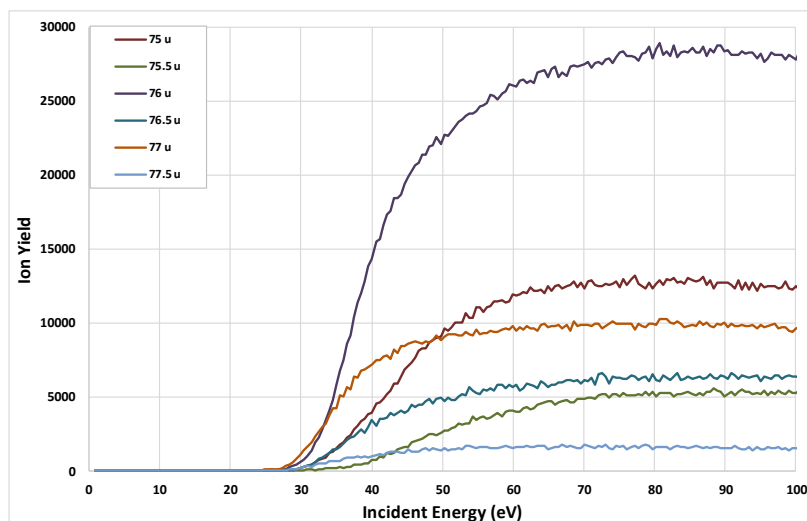
### 5.3.3 Groups 6 and 7

Figure 5.9 compares the Gaussian peak fitting results and the individual peak yields at 100 eV for Group 6. This group was fitted using Gaussian peaks at half-integer masses. The most abundant peak in this group is present at 76 u, which could have contributions from the fragment  $C_6H_4^+$  and/or the fragment  $C_{12}H_8^{2+}$  ( $m/z = 152/2$ ), suggesting double ionisation.



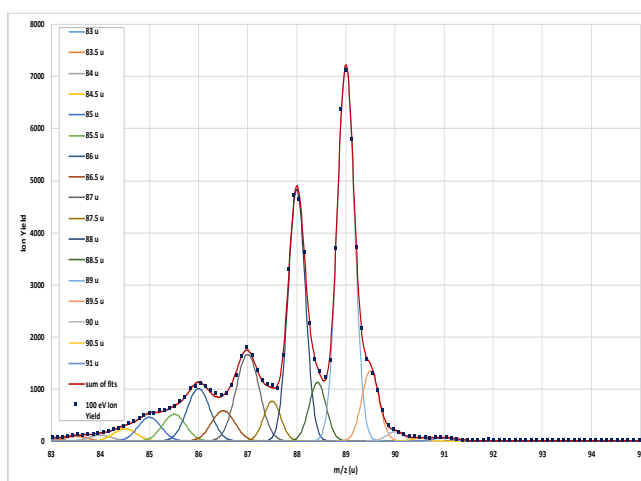
**Figure 5.9** Comparison between the Gaussian peak fitting results and the individual peak yields at 100 eV for Group 6.

Figure 5.10 displays the groups ion yield curves. 76 u has the highest yield, as can be seen in the fit, and 77 u has the earliest onset. The fragments at 72 u, 72.5 u, 78.5 u and 79 u have very low yields and have primarily been included to aid the accuracy of the fit. There is some variation in the onsets and the shapes of the curves in this group, suggesting different fragmentation processes are occurring.



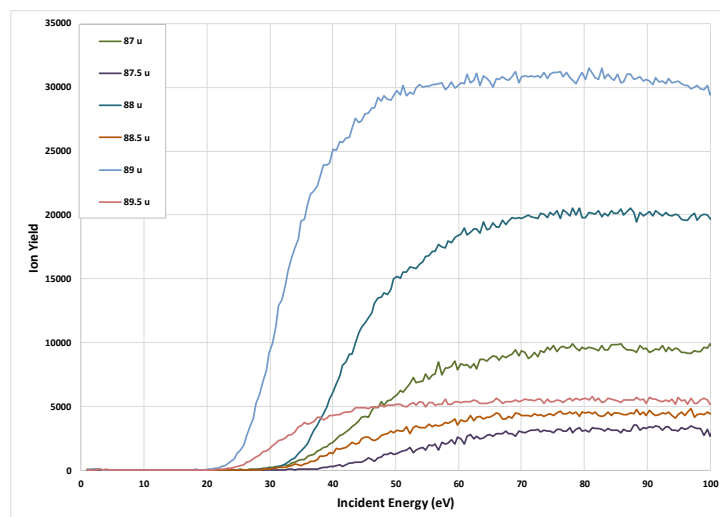
**Figure 5.10** Ion yield curves for Group 6.

Figure 5.11 compares the Gaussian peak fitting results and the individual peak yields at 100 eV for Group 7. The shoulder peaks are more evident in this group and the fit was done using Gaussian peaks at half-integer masses. The most abundant peak in this group is present at 89 u. Using femtosecond laser mass spectrometry, Robson et al. [35] have observed that the ratio of 89.5 u to 89 u is equal to the isotope ratio  $179 \text{ u} / 178 \text{ u}$ . Because the only possible configuration for 89.5 u is  $\text{C}_{13}^{13}\text{CH}_{10}^{2+}$ , 89 u must be predominantly the doubly-charged parent. In our case,  $179 \text{ u} / 178 \text{ u} = 0.18 \pm 0.01$ ,  $89.5 \text{ u} / 89 \text{ u} = 0.18 \pm 0.01$ , and  $77.5 \text{ u} / 77 \text{ u} = 0.16 \pm 0.01$ . The only possible configuration for 77.5 u is  $\text{C}_{11}^{13}\text{CH}_{10}^{2+}$ , so, both group 6 and 7 may have large contributions from doubly-charged fragments.



**Figure 5.11** Comparison between the Gaussian peak fitting results and the individual peak yields at 100 eV for Group 7.

The ion yield curves for Group 7 can be seen in Figure 5.12. The 89 u has the largest abundance and earliest onset.



**Figure 5.12** Ion yield curves for Group 7.

### 5.3.4 Groups 8, 9, 10 and 12

Figure 5.13 compares the Gaussian peak fitting results and the individual peak yields at 100 eV for Groups 8, 9, 10 and 12. Figures 5.15 and 5.16 displays the ion yield curves for groups 8, 9, 10 and 12.

In Group 8, the breaking of two C – C bonds in the central ring could lead to  $C_6H_4$  loss, producing  $C_8H_6^+$ . This is the fragment with the lowest appearance energy in group 8. The peak found at 98 u has the highest yield at 100 eV and could be produced by  $C_6H_4 + 4H$  loss.

In group 9, the loss of a fragment with 5 carbon atoms requires the breakage of three C-C bonds in both the central ring and one of the terminal rings. Without hydrogen rearrangement,  $C_5H_4$  loss would then be the most likely, producing  $C_9H_6^+$  (114 u). However,  $C_9H_7^+$  (115 u) has a lower appearance energy, and a higher abundance below 40 eV, indicating that the formation of 115 u involves the rearrangement of one hydrogen atom. Kingston et al. [30], Becker et al. [122] and Dyakov et al. [123] have discussed the occurrence of hydrogen shifting in PAHs, which is likely to occur with electron ionisation, and also the isomerisation that can occur in the fragment ions.

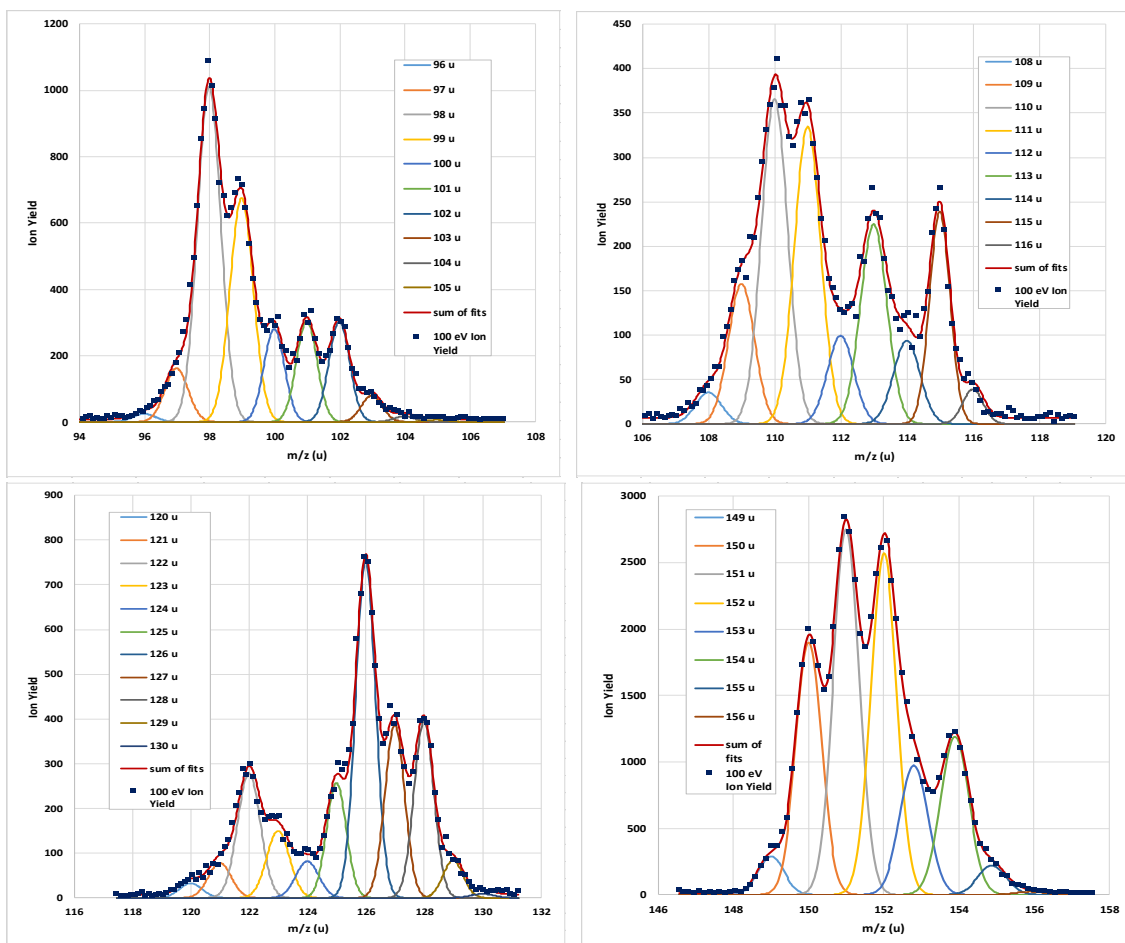


**Figure 5.13** Comparison between the Gaussian peak fitting results and the individual peak yields at 100 eV for Group 8 (top left), Group 9 (top right), Group 10 (bottom left) and Group 12 (bottom right).

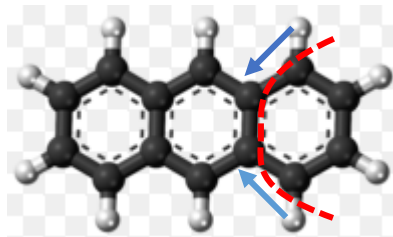


**Figure 5.14** Possible occurrence of  $C_4H_2$  loss after hydrogen shifting [124].

In group 9, there is some variation in the shapes of the curves. The yield of 115 u begins to decrease after 60 eV, unlike the other curves in this group, which continue to rise or level off.

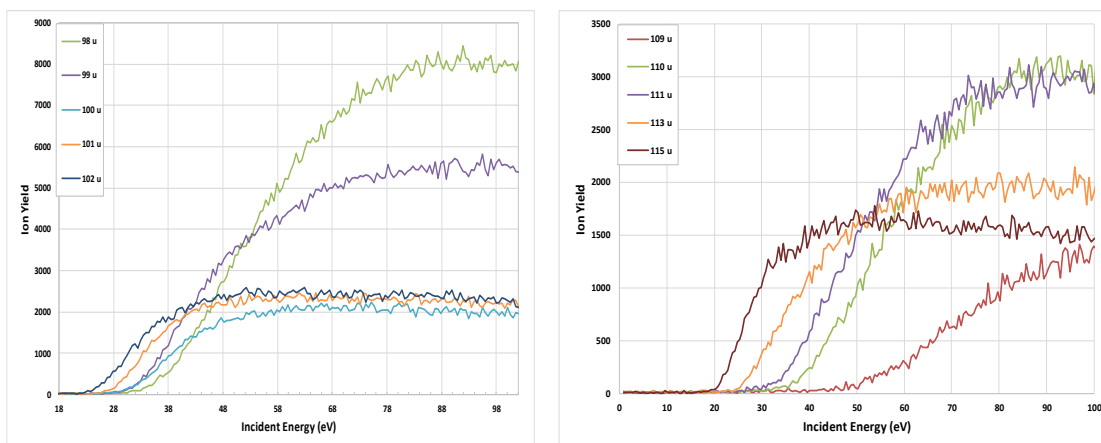


**Figure 5.15** Ion yield curves for Group 8 and 9.

In group 10, the peaks with the earliest onsets are for 128 u and 129 u, also indicating that hydrogen shifting is favourable for 128 u. This is illustrated in figure 5.16. The largest peak in group 10 is at 126 u, indicating the fragment  $C_{10}H_6^+$ , but its yield begins to decrease after 50 eV. There is also some variation in the shape of the curves in this group.

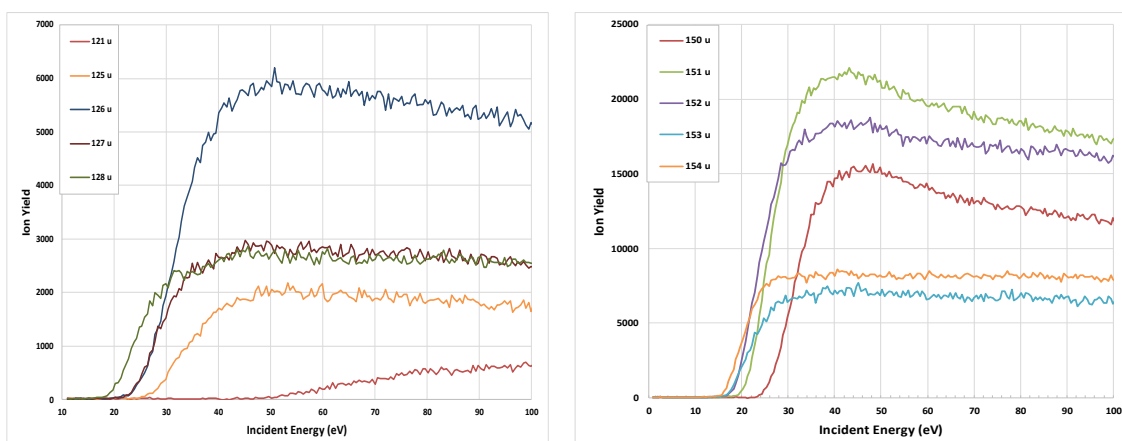


**Figure 5.16** Ion yield curves for Group 10 (left) and Group 12 (right).

In group 12, the earliest onsets are for 154 u, 155 u, and 153 u respectively, again suggesting it is energetically favourable that fragments in which one or two hydrogen atoms shift to other carbon atoms during the fragmentation are produced. The 154 u fragment is formed by  $C_2$  loss. If one would assume that the most abundant fragment in this group would be formed by the breakage of two C – C bonds in one of the terminal rings, one would expect that 152 u ( $C_{12}H_8^+$  formed by  $C_2H_2$  loss) would have the lowest appearance energy. The peaks with the highest yields group 12 are positioned at 151 u, 152 u and 150 u, and the yields of all three peaks begin to decrease above 50 eV. At higher electron energies 152 u and 151 u are the fragments with the highest abundance in this group. However, 154 u has the lowest appearance energy of  $15.5 \pm 0.2$  eV, indicating

that the transfer of two hydrogen atoms during the fragmentation, resulting in C<sub>2</sub> loss, is energetically favourable at low electron energies.

### 5.3.5 Groups 11 and 13

Figures 5.17 and 5.18 compare the Gaussian peak fitting results and the individual peak yields at 100 eV for groups 11 and 13. Most of the possible fragments associated with group 11, including the most abundant fragment at 139 u, indicate C<sub>3</sub>H<sub>3</sub> loss, C<sub>2</sub>H<sub>2</sub> loss and CH loss, accompanied by H, 2H and H<sub>2</sub> loss. The peaks in group 13 are likely formed due to CH loss, along with H, 2H and H<sub>2</sub> loss.

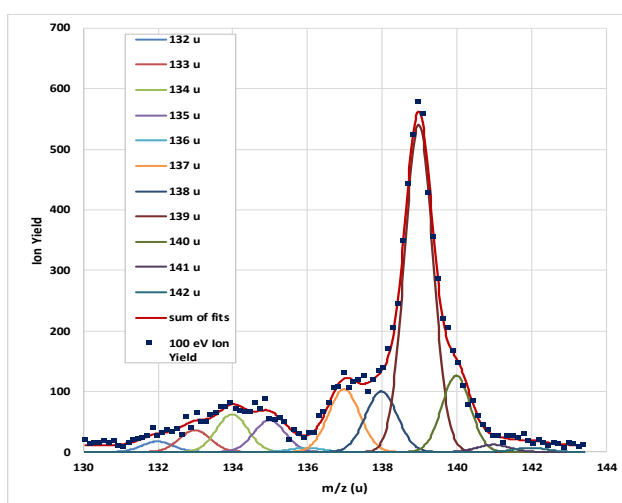


**Figure 5.17** Comparison between the Gaussian peak fitting result and the individual peak yields at 100 eV for Group 11.

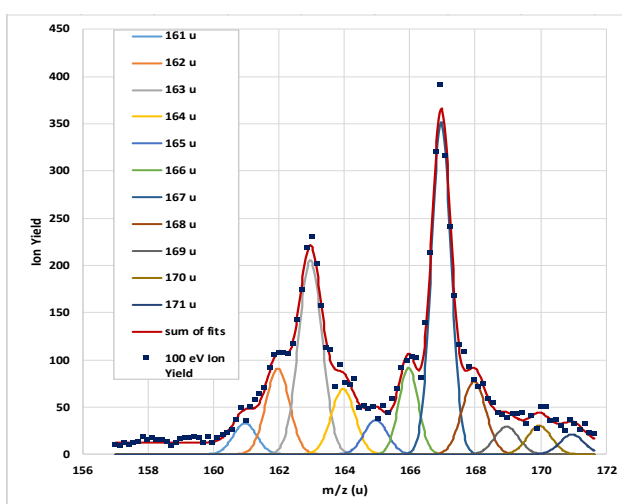


**Figure 5.18** Comparison between the Gaussian peak fitting results and the individual peak yields at 100 eV for Group 13.

The largest peak in group 13 is at 167 u, but this cannot be an anthracene fragment with only carbon and hydrogen atoms. We compared group 13 to the same group of peaks in

a mass spectrum we recorded for phenanthrene, an isomer of anthracene. The peak was not found in the mass spectrum for phenanthrene, see Figure 5.20, and it was concluded that this peak was due to a small contamination in anthracene. Comparison of the full mass spectra of anthracene and phenanthrene does not reveal any other significant spurious peaks.

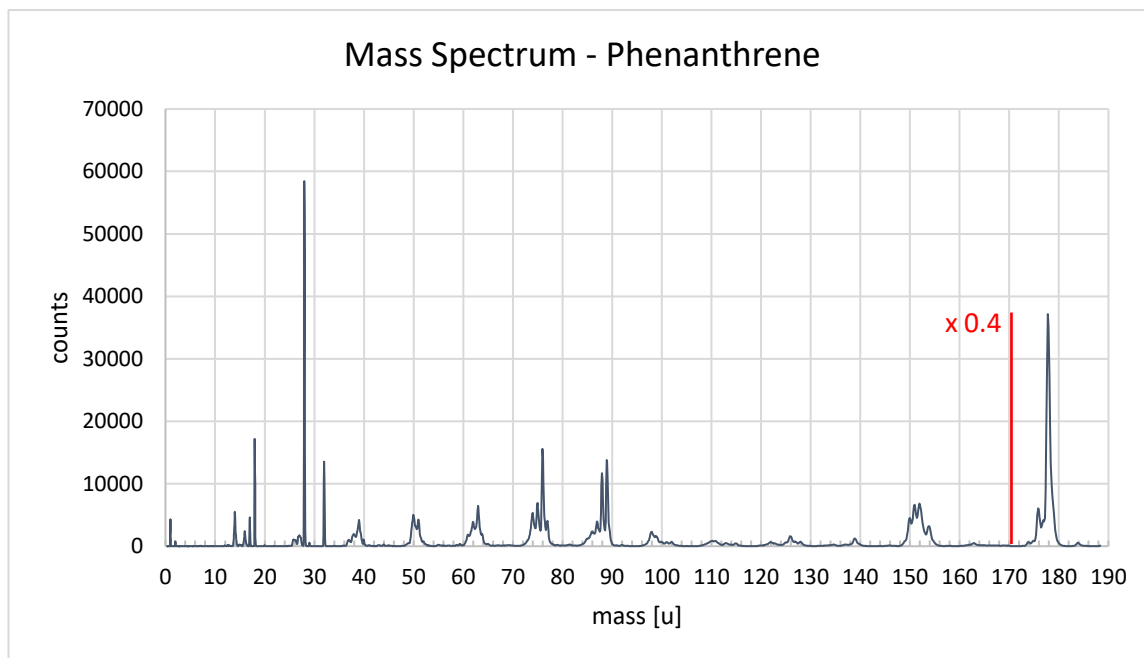


**Figure 5.19** Our mass spectrum for phenanthrene.

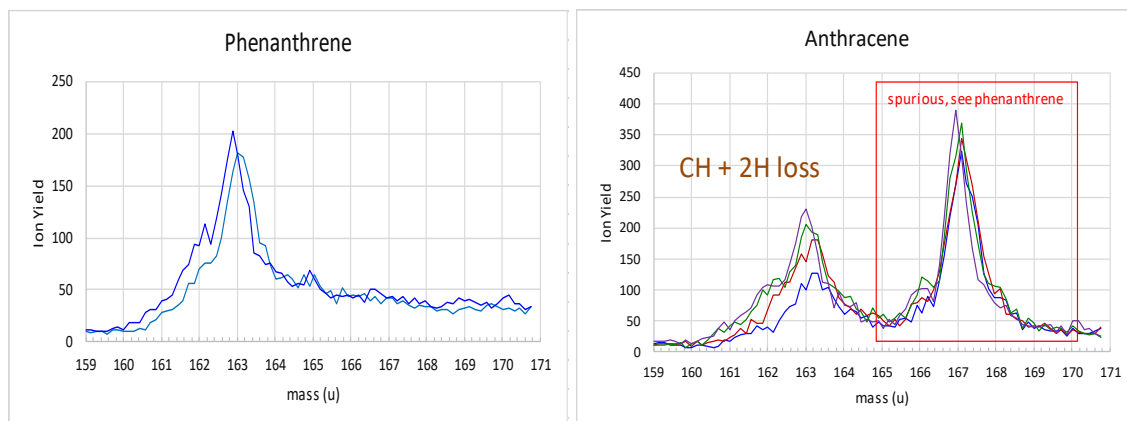
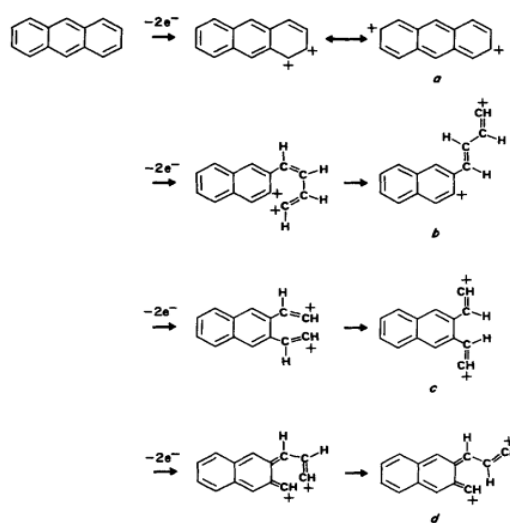


**Figure 5.20** Comparison between a phenanthrene and an anthracene mass spectrum to inspect the validity of the 167 u peak.

Kingston et al. [30] have observed that the main charge separation processes that occur when compounds such as benzene, naphthalene and anthracene undergo ionisation due to 70 eV electrons involve the products  $\text{CH}_3^+$ ,  $\text{C}_2\text{H}_2^+$  and  $\text{C}_3\text{H}_3^+$ , suggesting that there are preferred structures amongst the metastable parent ions. This is also relevant for groups 2 and 3. Kingston et al. argue that the large energy values involved in electron ionisation

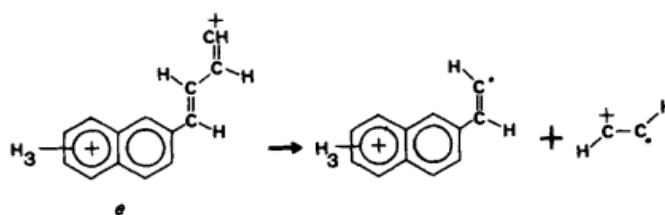
will result in some ions having sufficient energy to undergo isomerisation, and that this excess internal energy can be enough to allow the ions to further react via a transition state and charge separation. They also indicate that the preference for doubly and triply charged parent molecules to dissociate via the pathways leading to  $\text{CH}_3^+$ ,  $\text{C}_2\text{H}_2^+$  and  $\text{C}_3\text{H}_3^+$  products suggests there are common mechanisms occurring. Figure 5.21 displays the double ionisation of anthracene via the ejection of two electrons localised in one bond, and involves a ring opening. This is an arrangement proposed by Kingston et al. to possibly precede the processes by which anthracene could undergo  $\text{CH}_3^+$  loss.



**Scheme 1.**

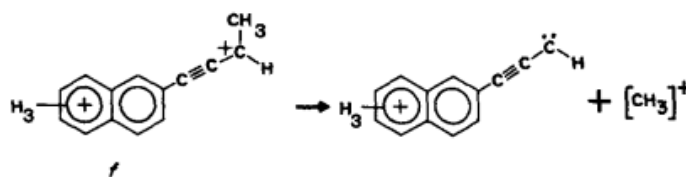
**Figure 5.21** Scheme 1 from Kingston et al. [30]

Kingston et al. state that the rearrangement of H atoms on the side chains of ions such as those shown in *b*, *c* and *d* is a process for which low energy barriers have been predicted. As such,  $\text{CH}_3^+$  could occur via the migration of hydrogen atoms to the ends of side chains. This may also cause the charge remaining on the cyclic part of the dication to shift away from the site of ring opening. They go on to discuss their use of the coulombic repulsion model to further analyse the charge separation reactions of the anthracene dication. This is represented in Scheme 2 and 3 below.



**Scheme 2.**

**Figure 5.22** Scheme 2 from Kingston et al showing a transition state in which one charge is centred on the end C atom of the chain.

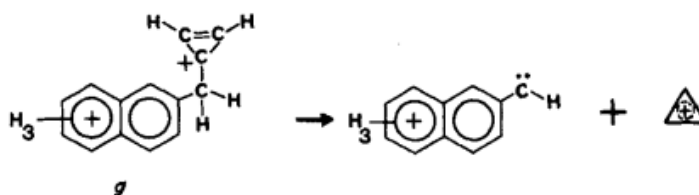


**Scheme 3.**

**Figure 5.23** Scheme 3 from Kingston et al showing a transition state in which the charge is centred on the adjacent C atom.

These schemes propose an explanation for why the  $M^{2+}$  species of anthracene undergo charge separation to yield a relatively high abundance of  $CH_3^+$  and  $C_2H_2^+$  ions, and why the effective interchange distance in the transition state is greater for the loss of two carbon atoms than for one.

Scheme 4 is also put forward to suggest that the rearrangement of the end carbon atoms could then induce  $C_3H_3^+$  loss. Here, a charge is situated on the second carbon atom from the ring.



**Scheme 4.**

**Figure 5.24** Scheme 4 from Kingston et al.

In 2014, Postma et al. [125] published a study in which they employed a molecular dynamics simulation based on analytical interaction potentials to model the interaction of low energy hydrogen and helium projectiles with isolated anthracene molecules. They have observed that in collisions with 1 keV He projectiles, a collision with a C atom in the molecule will cause the C atom to be knocked out with a substantial amount of energy, while the hydrogen that was attached to it is more or less stationary and stays in the vicinity of the molecule. However, they have stated that direct C knock out is not the main pathway leading to PAH destruction, but that destruction proceeds mainly through  $C_2H_2$  loss from the periphery of the PAH, and that if the PAH is not fully destroyed,  $C_2H_2$  loss can initiate isomerization and cage formation.

They identify H,  $H_2$  and  $C_2H_2$  loss from singly charged PAH cations as important channels here, which they recognised are also important channels for low energy electron impact, photoionisation and collision induced dissociation studies.

Reitsma et al. (2012) [126] have studied the fragmentation of anthracene after double electron transfer to a 5 keV proton, and use the collision induced dissociation under energy control method to directly investigate the energetics of fragmentation processes in PAH dications experimentally. They present experimental evidence for a dominance of fission into  $C_{11}H_7^+ - C_3H_3^+$ , over  $C_2H_2^+$  loss. Their coincidence map of the TOFs of pairs of cationic reaction products formed after collisions with 5 keV protons show islands due to  $C_2H_x^+$ ,  $C_3H_x^+$ ,  $C_4H_x^+$  and  $C_5H_x^+$  in coincidence with heavier anthracene fragments such as  $C_{12}H_y^+$ . The most prominent fission channel is  $C_{11}H_x^+ - C_3H_x^+$ .

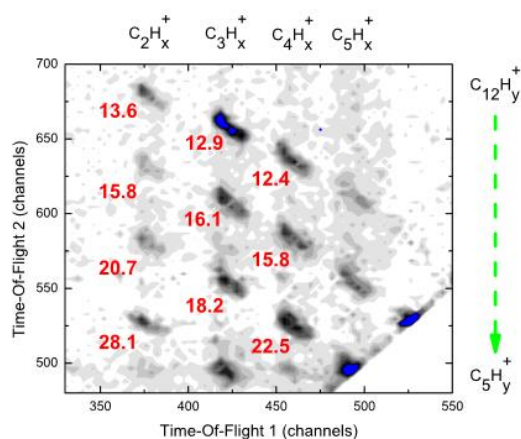


**Figure 5.25** Coincidence map from Reitsma et al.

In their single TOF spectrum, the strongest peak is  $C_{12}H_8^{2+}$ , indicating  $C_2H_2$  loss is the dominant fragmentation channel for anthracene dications formed here.  $C_2H_2$  loss-related processes are prominent in their correlation diagrams, with  $C_2H_2$  loss from the anthracene dication being a competing channel found experimentally to dominate the dissociation dynamics. The fragmentation of  $C_{14}H_{10}^{2+}$  is dominated by emission of  $C_2H_2$  here. Additional important channels in their single TOF spectrum are H and  $H_2$  loss.

The below figure shows that the emission of  $C_3H_3^+$  occurs via an outer ring opening, and an analysis of the transition state confirms that it is energetically more favourable to emit  $C_3H_3^+$  than  $C_3H_3$ .

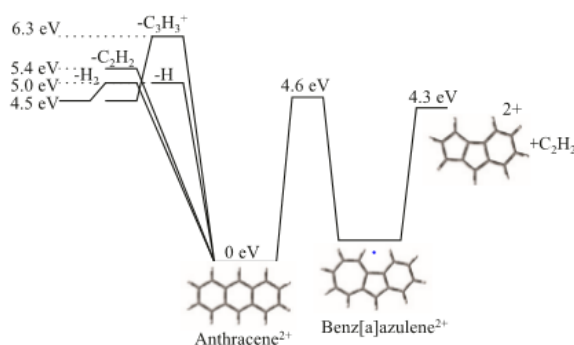


**Figure 5.26** Graphical summary of the DFT structure calculations from Reitsma et al.

The ion yield curves for groups 11 and 13 can be seen in Figure 5.27 below.

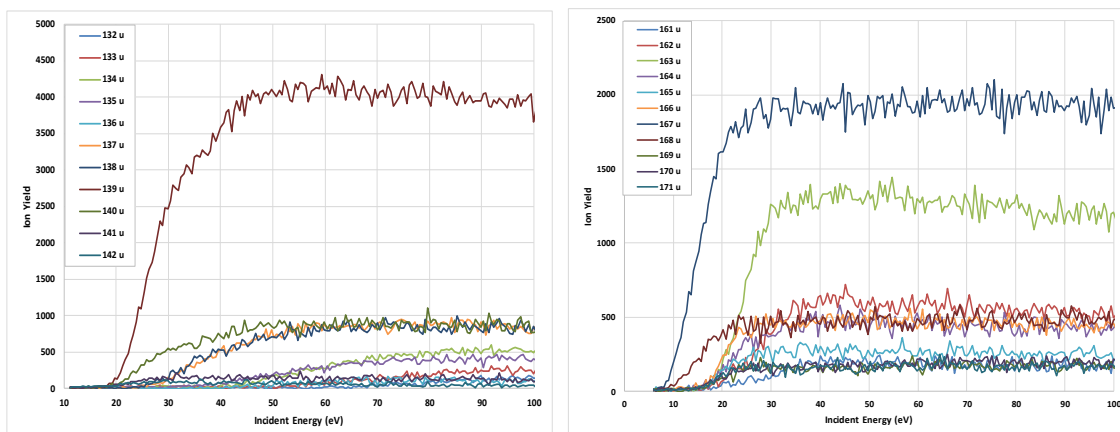


Figure 5.27 Ion yield curves for Group 11 (left) and Group 13 (right).

### 5.3.6 Group 14

Figure 5.28 compares the Gaussian peak fitting results and the individual peak yields at 100 eV, and Figure 5.29 shows ion yields curves for Group 14.

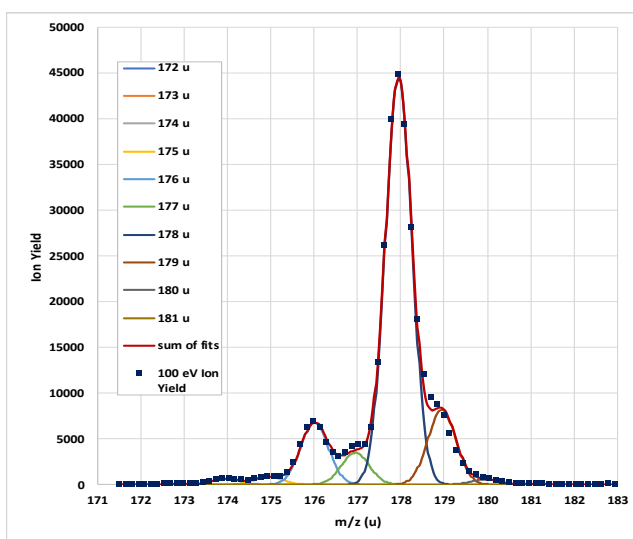
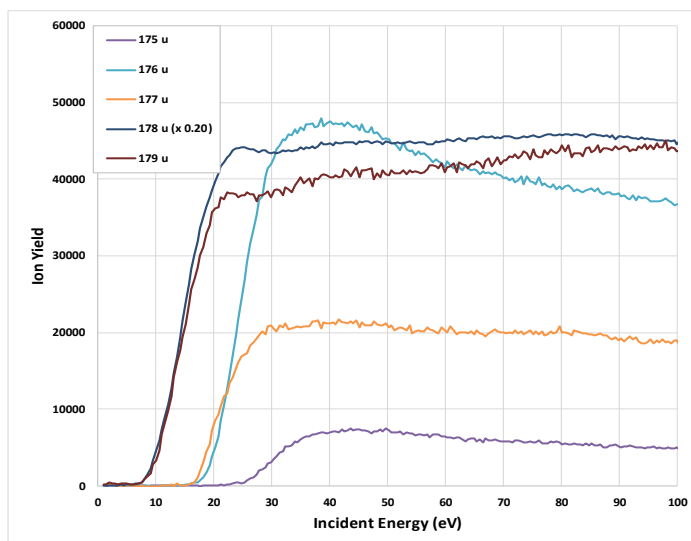


Figure 5.28 Comparison between the Gaussian peak fitting results and the individual peak yields at 100 eV for Group 14.



**Figure 5.29** Ion yield curves for Group 14.

Group 14 contains the parent ion peak at 178 u, the peak in the mass spectrum with the highest abundance. The losses associated with the fragments in this group are H loss and 2H loss. The ion yield curves in this group exhibit approximately the same shape. The 176 u fragment has a higher onset than the 177 u fragment, as the additional hydrogen loss involved in forming the 176 u fragment requires more energy.

## 5.4 Appearance Energies

The appearance energies of all the fragments with sufficient yields in our mass spectrum for anthracene are displayed in Table 5.6 – 5.8. These are the minimum energies that must be supplied to the anthracene molecule to produce the fragments we see in our mass spectrum, and they allow us to view the fragmentation sequence of the compound as a function of impact energy. We have determined our appearance energy values from the ion yield curves presented in this chapter. Some appearance energies were difficult to determine accurately due to the low yield of certain fragments. There is little data published with regards to the appearance energies of anthracene fragments for EI, bar that of the parent ion. The value obtained in this research is in good agreement with this data.

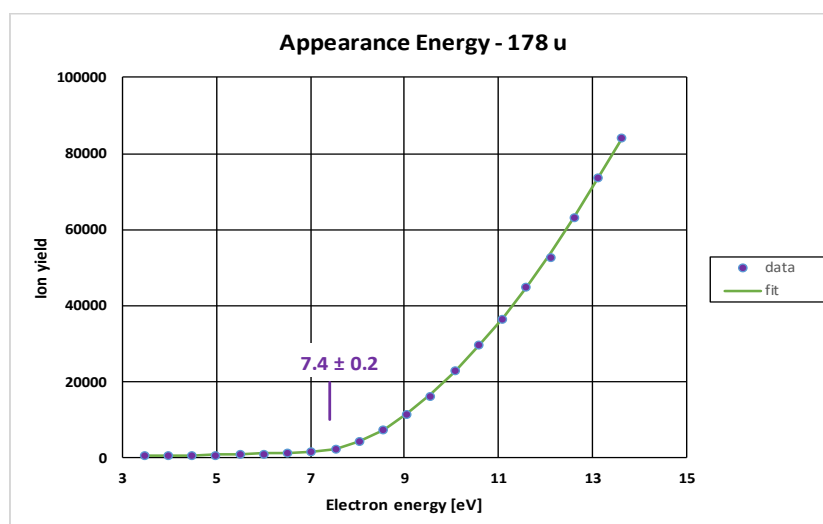


**Figure 5.30** Data and best fit model from the fitting procedure for the anthracene parent ion.

The lowest appearance energy recorded in this research is  $7.4 \pm 0.2$  eV for parent ion at 178 u. As expected, the appearance energy for the anthracene isotope  $C_{13}^{13}CH_{10}^+$  is the same (within the estimated error):  $7.3 \pm 0.4$  eV. In general, the appearance energies for the fragments in groups 8 to 13 are progressively higher for smaller groups, and within each group appearance energies tend to be higher for fragments with fewer hydrogen atoms. This indicates that at higher electron impact energies excess excitation energy is lost by the release of additional hydrogen atoms.

Single-Ionisation Potential of the Anthracene Parent Ion (eV)	
Kuroda (1964) [26]	7.55
Stahl and Maquin (1984) [127]	7.47
Jochims et al. (1999) [31]	7.45
Mallocci et al. (2011) [128]	$7.439 \pm 0.006$
Maynooth Research (2017)	$7.4 \pm 0.2$

**Table 5.4** Published values for the appearance energy of the anthracene parent ion.

The appearance energy we recorded for the 89 u is  $20.2 \pm 0.7$  eV. Based on the discussion in section 5.3.3, this value can be considered as our measurement for the double-ionisation potential of anthracene. Our value is in good agreement with other determinations of the double ionization energy, see table 5.5.

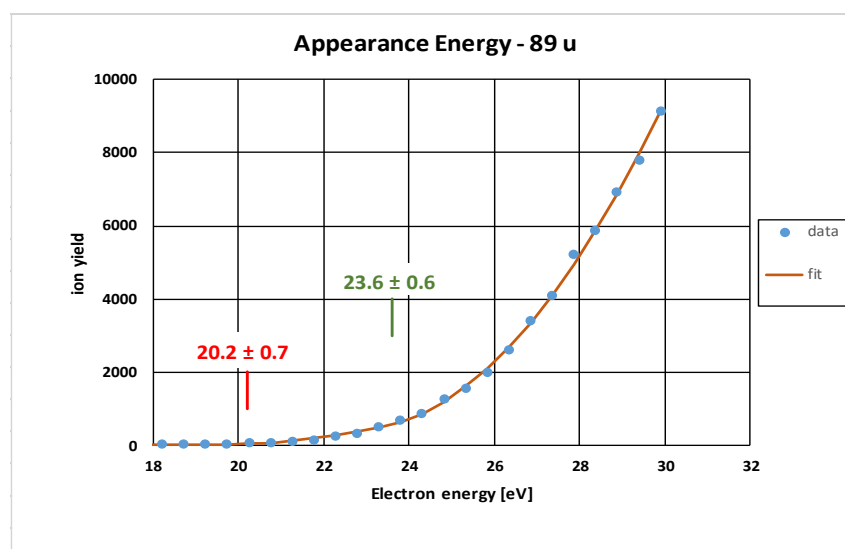


**Figure 5.31** Data and best fit model from the fitting procedure for the anthracene parent ion.

ion	$m/q$	present work	Mathur et al [29]
$C_{12}H_6^{2+}$	75 u	$29.1 \pm 0.5$ eV	$31.8 \pm 0.5$ eV
$C_{12}H_8^{2+}$	76	$27.2 \pm 1.2$	$29.9 \pm 0.5$
$C_{14}H_8^{2+}$	88	$27.9 \pm 1.0$	$21.2 \pm 0.5$
$C_{14}H_{10}^{2+}$	89	$20.2 \pm 0.7$	$21.1 \pm 0.5$

**Table 5.5** The appearance energies for some fragments from anthracene mass spectra.

Directly to the left of the 60 u peak in group 5 is a small but distinct peak at 59.33 u. This is attributed to the triply-charged parent molecule. Figure 5.28 shows the ion yield curve, and the fitted onset function for the triply-charged parent. The appearance energy is  $45.5 \pm 0.5$  eV. This is the first direct determination of the triple ionization energy. Our value is significantly higher than the measurement of 38.2 eV by Kingston et al [30], who determined the double and triple ionization energies from energy defects in the charge stripping reactions of multiply-charged parent ions in  $N_2$  gas.

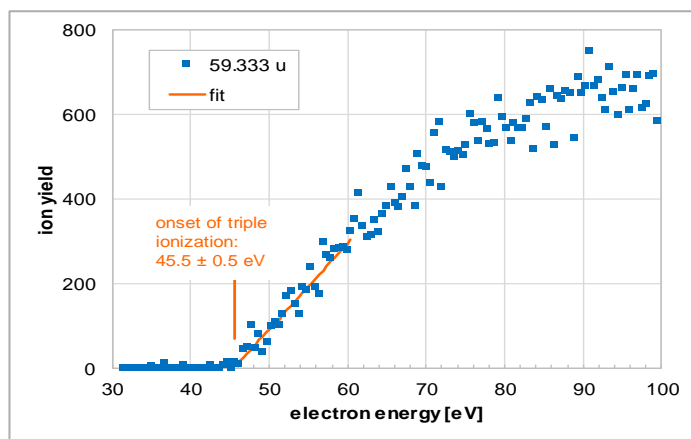


**Figure 5.32** Data and best fit model from the fitting procedure for the anthracene parent ion.

<b>Group No.</b>	<b>Mass (u)</b>	<b>AE 1 (eV)</b>	<b>Uncert. (eV)</b>	<b>AE 2 (eV)</b>	<b>Uncert. (eV)</b>
Group 2	26	31.0	0.6	-	-
	27	32.0	0.8	-	-
Group 3	37	44.1	1.8	58.3	1.4
	38	34.9	0.6	-	-
	39	21.0	1.0	29.4	1.3
	40	16.1	0.8	32.9	0.9
	41	23.1	0.8	-	-
Group 4	49	33.5	0.9	60.3	1.2
	50	25.7	1.1	31.7	1.5
	51	26.4	1.4	30.9	0.5
	52	24.9	1.1	30.8	0.8
	53	26.2	1.0	-	-
Group 5	59.333	45.5	0.5	-	-
	61	39.5	0.7	48.7	1.2
	61.5	44.9	0.8	-	-
	62	33.0	0.6	37.9	0.7
	62.5	41.2	0.7	-	-
	63	26.0	0.9	-	-
	63.5	35.0	0.7	-	-
	64	28.9	1.0	33.7	0.7
	64.5	30.0	0.6	-	-
	65	26.9	0.5	-	-
Group 6	73	51.7	1.3	-	-
	74	28.5	0.9	34.1	0.8
	74.5	31.3	0.7	-	-
	75	29.1	0.5	-	-
	75.5	28.6	0.6	37.6	0.5
	76	27.2	1.2	30.5	0.5
	76.5	29.2	0.3	-	-
	77	26.8	0.3	-	-
	77.5	27.4	0.3	-	-
	78	26.2	0.6	-	-

**Table 5.6** The appearance energies of the anthracene fragments from groups 2 – 6.

<b>Group No.</b>	<b>Mass (u)</b>	<b>AE 1 (eV)</b>	<b>Uncert. (eV)</b>	<b>AE 2 (eV)</b>	<b>Uncert. (eV)</b>
Group 7	84.5	58.1	1.7	-	-
	85	30.0	1.2	44.8	1.2
	85.5	47.6	1.5	-	-
	86	30.1	0.8	35.3	0.8
	86.5	47.2	1.0	-	-
	87	26.2	0.7	32.3	0.6
	87.5	36.8	0.7	-	-
	88	27.9	1.0	30.9	0.7
	88.5	28.7	0.7	35.3	0.6
	89	20.2	0.7	23.6	0.6
	89.5	21.1	0.5	24.3	0.6
90	24.9	0.4	-	-	
Group 8	97	46.9	1.0	-	-
	98	29.9	0.7	-	-
	99	27.4	0.6	-	-
	100	29.8	0.7	-	-
	101	26.4	0.6	-	-
	102	22.9	0.3	-	-
	103	22.0	0.5	-	-
Group 9	109	47.9	0.8	-	-
	110	34.8	0.6	-	-
	111	33.3	0.6	-	-
	112	30.8	0.8	-	-
	113	24.3	0.3	-	-
	114	24.5	0.5	-	-
	115	20.4	0.2	-	-
	116	21.3	0.6	-	-
Group 10	120	56.3	0.6	-	-
	121	48.4	0.6	-	-
	122	40.1	0.7	-	-
	123	31.0	0.7	-	-
	124	32.1	0.6	-	-
	125	25.1	0.5	-	-
	126	23.2	0.2	26.3	0.4
	127	22.1	0.3	-	-
	128	18.4	0.3	-	-
	129	17.7	0.5	-	-

**Table 5.7** The appearance energies of the anthracene fragments from groups 7 – 10.

Group No.	Mass (u)	AE 1 (eV)	Uncert. (eV)	AE 2 (eV)	Uncert. (eV)
Group 11	133	52.2	1.4	-	-
	134	39.9	0.7	-	-
	135	40.6	0.9	-	-
	137	25.3	0.4	-	-
	138	24.3	0.3	-	-
	139	17.8	0.4	-	-
	140	20.1	0.3	-	-
Group 12	149	27.2	0.6	-	-
	150	23.0	0.2	-	-
	151	18.6	0.2	-	-
	152	17.0	0.2	-	-
	153	16.9	0.2	-	-
	154	15.5	0.2	-	-
	155	16.4	0.2	-	-
Group 13	161	16.9	1.0	-	-
	162	16.8	0.5	-	-
	163	15.3	0.6	-	-
	164	17.0	0.9	-	-
	165	16.0	0.3	-	-
Group 14	174	28.2	0.4	-	-
	175	25.7	0.5	-	-
	176	17.3	0.3	-	-
	177	16.5	0.4	-	-
	178	7.4	0.2	-	-
	179	7.3	0.4	-	-
	180	9.2	0.3	-	-

**Table 5.8** The appearance energies of the anthracene fragments from groups 11 – 14.

Figure 5.33 is a graph containing all the appearance energies we have determined the anthracene via low-energy electron impact. From group 14, we can see that the appearance energies of 174 u, 175 u, 176 u and 177 u are higher than that of 178 u. 174 u is formed by  $H_2 + H_2$  loss and 176 u is formed by  $H_2$  loss. Figure 5.29 would also indicate that  $C_nH_{n-2}$  loss is more energetically favourable than  $C_nH_n$  loss. The high appearance energies we see for groups 2 – 4 could be due to energetic charge-separation fragmentations of doubly-charged anthracene.

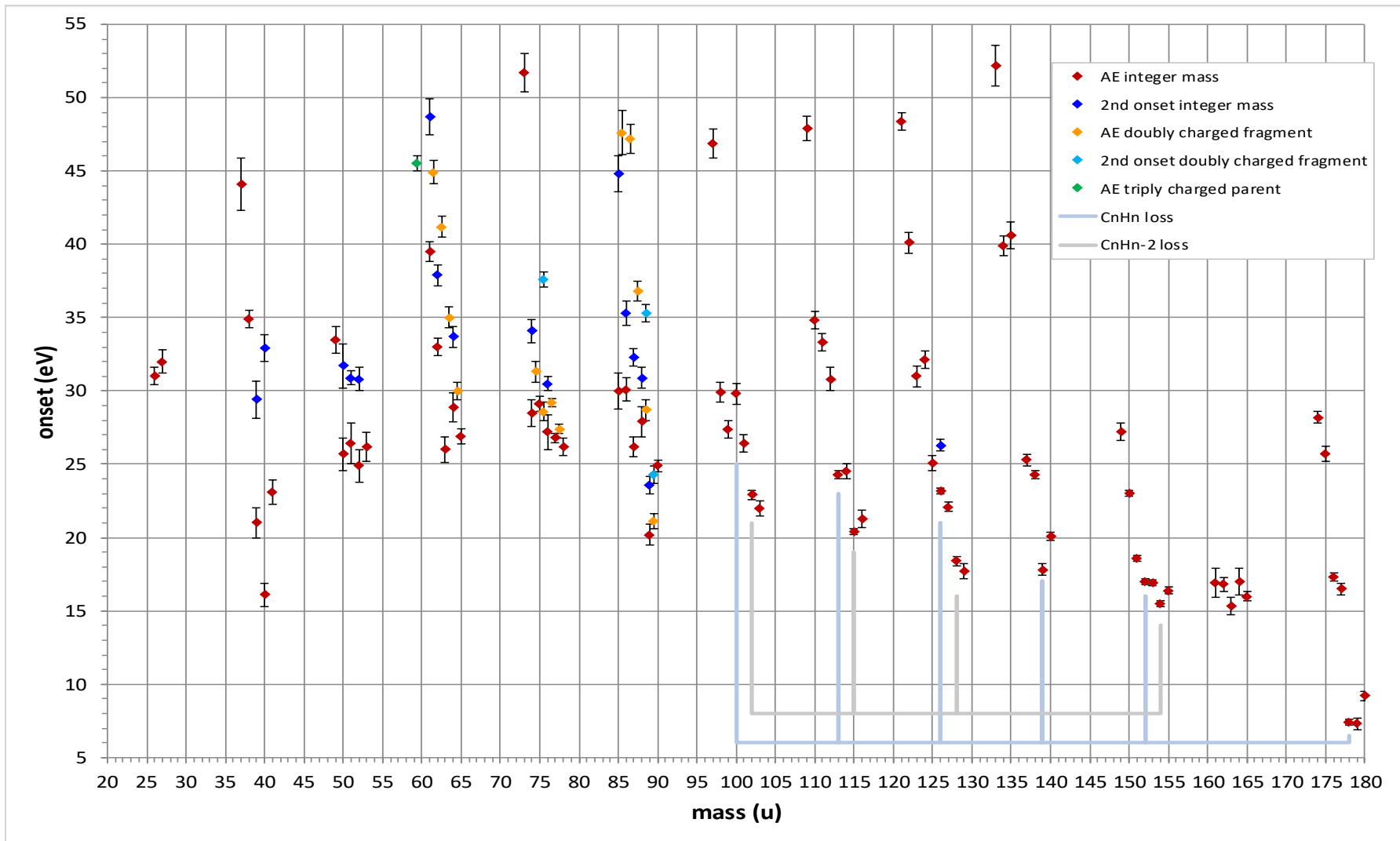


**Figure 5.33** Graph displaying the appearance energies of the fragments in our mass spectrum for anthracene.

## 6 Conclusion

The aim of this research was to study low-energy electron-impact fragmentation of anthracene. We have measured mass spectra for positive ions produced by low-energy electron impact on anthracene using a reflectron time-of-flight mass spectrometer. The electron impact energy has been varied from 0 to 100 eV in steps of 0.5 eV. By fitting groups of adjacent peaks in the mass spectra with sequences of normalized Gaussians, we have obtained ion yield curves, and have determined appearance energies for positive fragments of anthracene. We have also made the first direct determination of the triple-ionization energy of anthracene.

The groups of fragments containing 8 to 13 carbon atoms provide evidence for hydrogen rearrangements during the fragmentation, involving retention or loss of one or two additional hydrogen atoms. Groups of fragments with 6 and 7 carbon atoms clearly show the presence of doubly-charged fragments. The smaller fragments with 1 to 4 carbon atoms all show broadened peaks, and these fragments may be partly or mostly due to energetic charge-separation fragmentations of doubly-charged anthracene.

After we took the measurements for anthracene, we also obtained a data set of 200 mass spectra for phenanthrene. Comparison of the mass spectra of phenanthrene and anthracene by stepping through all electron energies does not reveal any clear systematic difference, and we suspect that there are no substantial differences in the electron-induced fragmentation pathways between anthracene and phenanthrene.

Our data is in agreement with other data available for anthracene, and the appearance energies we have determined allow us insight into the fragmentation processes of anthracene induced by low-energy electron-impact. Many molecular species in the interstellar medium are assumed to be formed by chemical reactions within the ice mantles on interstellar dust grains caused by irradiation of ultraviolet light and cosmic rays. This irradiation releases many secondary electrons which may themselves induce chemical reactions. Study of electron-impact induced processes is of relevance in this context. There are future plans in Maynooth to examine more PAHs through electron-impact fragmentation.

## References

- [1] Atkins, P.; De Paula, J.; *Physical Chemistry*, 8th edition, Oxford University Press (2006).
- [2] Samanta, S.K.; Singh, O.V.; Jain, R.K.; *Polycyclic aromatic hydrocarbons: Environmental pollution and bioremediation*, Trends in Biotechnology, Volume 20, Issue 6, p. 243 – 248, June (2002).
- [3] Prentice Hall Texts, *Molecular Geometry and Bonding Theories, Chapter 9: Multiple Bonds*, Pearson Education.
- [4] Tamakawa, K., *Polycyclic Aromatic Hydrocarbon*, Volume 51, pp. 599 – 601, Comprehensive Analytical Chemistry: Food Contaminants and Residual Analysis, Wilson & Wilson, Elsevier (2008).
- [5] Tielens, A. G. G. M., *Interstellar Polycyclic Aromatic Hydrocarbon Molecules*, Volume 46, pp. 289 – 337, Annual Review of Astronomy and Astrophysics, September (2008).
- [6] Tielens, A.G.G.M., *A molecular universe*, Volume 85, pp. 1021 – 1081, Reviews of Modern Physics, July – September (2013).
- [7] van der Naald, W.G.H.; Tamis, W.; van der Berg, M.M.H.E., *Polycyclic Aromatic, Hydrocarbons in the Dutch Environment*, CCRX Report, Leidschendam, The Netherlands: Coordinating Committee for the Monitoring of Radioactivity and Xenoviotic Substances (1988).
- [8] Freudenthal, R.I., Jones, P.W. (Eds.) *Polynuclear Aromatic Hydrocarbons, Chemistry, Metabolism and Carcinogenesis*, Raven Press New York (1976).
- [9] Freeman, D.J.; Catteil, F.C.R., *Woodburning as a source of atmospheric polycyclic aromatic hydrocarbons*, Volume 24, Issue 10, pp. 1581 – 1585, Environmental Science and Technology, October (1990).
- [10] Amuda, O.S.; Adelowo-Imeokparia, F.E., *Polycyclic Aromatic Hydrocarbons in Municipal Waste Ashes from Three Waste Dumps in Lagos, Nigeria*, Volume 21, Issue 1, pp. 141 – 144, Bulletin of the Chemical Society of Ethiopia, April (2007).

- [11] Gülnihal K.; Mehmet Emin Aydin, *Development of an Analytical Method for the Quantification of 26 Polycyclic Aromatic Hydrocarbons from Ambient Air Particle Matter*, Journal of Selçuk University Natural and Applied Science Digital Proceeding Of The ICOEST May 14 – 17 (2014).
- [12] Dzepina, K.; Arey, J.; Marr L.C.; Worsnop, D.R.; Salcedo, D.; Zhang, Q.; Onasch, T.B.; Molina, L.T.; Molina M.J.; Jimenez J.L., *Detection of particle-phase polycyclic aromatic hydrocarbons in Mexico City using an aerosol mass spectrometer*, Volume 263, Issue 2-3, pp.152 – 170, International Journal of Mass Spectrometry, June (2007).
- [13] Xing, X.; Zheng, H.; Zhang, Y.; Yang, D.; and Qi, S.; *Temporal and Spatial Variety of Polycyclic Aromatic Hydrocarbons (PAHs) Atmospheric Deposition in Chengdu Economic Region, China*, Proceedings of the 14th International Conference on Environmental Science and Technology Rhodes, Greece, September (2015).
- [14] Duley, W.W.; Williams, D.A., *The infrared spectrum of interstellar dust: Surface functional groups on carbon*, Volume 196, Issue 2, pp. 269 – 274, Monthly Notices of the Royal Astronomical Society, September (1981).
- [15] Allamandola, L.J.; Tielens, A.G.G.M.; Barker, J.R., *Polycyclic Aromatic Hydrocarbons and the Unidentified Infrared Emission Bands: Auto Exhaust Along the Milky Way!*, Volume 290, L25 - L28, The Astrophysical Journal Part 2 Letters to the Editor (1985).
- [16] Ehrenfreund, P.; Cami, J., *Cosmic Carbon Chemistry: From the Interstellar Medium to the Early Earth*, Volume 2, Issue 12, pp. 232 – 245, Cold Spring Harbor Perspectives in Biology, December (2010).
- [17] Bernstein, M.P.; Sandford, S.A.; Allamandola, L.J.; Gillette, J.S.; Clemett, S.J.; Zare, R.N., *UV Irradiation of Polycyclic Aromatic Hydrocarbons in Ices: Production of Alcohols, Quinones, and Ethers*, Volume 283, pp. 1135 – 1138, Science, February (1999).
- [18] Bernstein, M.P.; Sandford, S.A.; Allamandola, L.J., *Hydrogenated Polycyclic Aromatic Hydrocarbons and the 2940 and 2850 Wavenumber (3.40 and 3.51 Micron) Infrared Emission Features*, Volume 472, L127 - L130, The Astrophysical Journal, The American Astronomical Society, December (1996).

- [19] Peeters, E.; Spoon, H.W.; Tielens, A.G.G.M., *Polycyclic Aromatic Hydrocarbons as a tracer of star formation?* Volume 613, pp. 986 – 1003, *The Astrophysical Journal*, The American Astronomical Society, October (2004).
- [20] Bakes, E.L.O.; Tielens, A.G.G.M., *Observational Aspects of Polycyclic Aromatic Hydrocarbon Charging in the Interstellar Medium*, Volume 73, pp.59 – 62, *Airborne Astronomy Symposium on the Galactic Ecosystem*, ASP Conference Series (1995).
- [21] Rauls, E.; Hornekaer, L., *Catalyzed Routes to Molecular Hydrogen Formation and Hydrogen Addition Reactions on Neutral Polycyclic Aromatic Hydrocarbons under Interstellar Conditions*, Volume 679, pp. 531 – 536, *The Astrophysical Journal*, The American Astronomical Society, May (2008).
- [22] Iglesias-Groth, S.; Manchado, A.; Rebolo, R.; González- Hernández, J.I.; García-Hernández, D.A.; Lambert, D.L., *A search for interstellar anthracene toward the Perseus anomalous microwave emission region*, Volume 407, Issue 4, pp. 2157 – 2165, *Monthly Notices of the Royal Astronomical Society*, October (2010).
- [23] Mason, N.J.; Nair, B.; Jheeta, S.; Szymańska, E., *Electron induced chemistry: a new frontier in astrochemistry*, Volume 168, pp. 235 – 247, *Faraday Discuss*, The Royal Society of Chemistry, February (2014).
- [24] The Thomas/Penfold Group, *Magnetic Resonance*. Retrieved from <http://rkt.chem.ox.ac.uk/tutorials/optionTwo/opt2Nmr.html>. [Accessed 17<sup>th</sup> August 2017].
- [25] Wacks, M.E.; Dibeler, V.H., *Electron Impact Studies of Aromatic Hydrocarbons. I. Benzene, Naphthalene, Anthracene, and Phenanthrene*, Volume 31, Issue 6, pp. 1557 – 1562, *The Journal of Chemical Physics*, December (1959).
- [26] Kuroda, H., *Ionization Potentials of Polycyclic Aromatic Hydrocarbons*, Volume 201, pp. 1214 – 1215, *Nature*, March (1964).
- [27] Dougherty, R.C.; Weisenberger, C.R., *Negative Ion Mass Spectra of Benzene, Naphthalene, and Anthracene. A New Technique for Obtaining Relatively Intense and Reproducible Negative Ion Mass Spectra*, Volume 90, Issue 23, pp. 6570 – 6571, *Journal of the American Chemical Society*, November (1968).

- [28] Shushan, B.; Boyd, R.K., *Unimolecular and Collision Induced Fragmentations of Molecular Ions of Polycyclic Aromatic Hydrocarbons*, Volume 15, Issue 9, pp. 445 – 453, *Organic Mass Spectrometry*, June (1980).
- [29] Mathur, B.P.; Burgess, E.M.; Bostwick, D.E.; Moran, T.F., *Doubly Charged Ion Mass Spectra*, Volume 16, Issue 2, pp. 92 – 98, *Organic Mass Spectrometry*, February (1981).
- [30] Kingston, R.G.; Guilbaus, M.; Brenton, A.G.; Beynon, J.H., *Multiple Ionization, Charge Separation and Charge Stripping Reactions Involving Polycyclic Aromatic Compounds*, Volume 20, Issue 6, pp. 406 – 412, *Organic Mass Spectrometry*, June (1985).
- [31] Hagan, D.A.; Eland, J.H.D., *Formation and Decay of Doubly Charged Ions from Polycyclic Aromatic Hydrocarbons and Related Compounds*, Volume 5, pp. 512 – 517, *Rapid Communications in Mass Spectrometry*, November (1991).
- [32] Jochims, H.W.; Rühl, E.; Baumgärtel, H.; Tobita, S.; Leach, S., *Size Effects on Dissociation Rates of Polycyclic Aromatic Hydrocarbon Cations: Laboratory Studies and Astrophysical Implications*, Volume 420, Issue 1, pp. 307 – 317, *The Astrophysical Journal*, January (1994).
- [33] Jochims, H.W.; Baumgärtel, H.; Leach, S., *Structure-Dependent Photostability of Polycyclic Aromatic Hydrocarbon Cations: Laboratory Studies and Astrophysical Implications*, Volume 512, Issue 1, pp. 500 – 510, *The Astrophysical Journal*, February (1999).
- [34] Tobita, S.; Leach, S.; Jochims, H.W.; Rühl, E.; Illenberger, E.; Baumgärtel, H., *Single and Double ionisation potentials of polycyclic aromatic hydrocarbons and fullerenes by photon and electron impact*, Volume 72, Issue 11-12, p. 1060, *Canadian Journal of Physics*, November (1994).
- [35] Robson, L.; Tasker, A.D.; Ledingham, K.W.D.; McKenna, P.; McCanny, T.; Kosmidis, C.; Tzallas, P.; Jaroszynski, D.A.; Jones, D.R., *Ionisation and fragmentation dynamics of laser desorbed polycyclic aromatic hydrocarbons using femtosecond and nanosecond post-ionisation*, Volume 220, Issue 1, pp. 69 – 85, *International Journal of Mass Spectrometry*, September (2002).

- [36] Reitsma, G.; Zettergren, H.; Martin, S.; Bredy, R.; Chen, L.; Bernard, J.; Hoekstra, R.; Schlatholter, T., *Activation energies for fragmentation channels of anthracene dications—experiment and theory*, Journal of Physics B: Atomic, Molecular and Optical Physics, Volume 45, Issue 21, p. 6, November (2012).
- [37] Brédy, R.; Ortéga, M.J.; Bernard, J.; Chen, L.; Montagne, G.; Martin, S., *Fragmentation of anthracene induced by collisions with 40 keV Ar<sup>8+</sup> ions*, Volume 156, pp. 1 – 3, Physica Scripta, September (2013).
- [38] Postma, J.; Bari, S.; Hoekstra, R.; Tielens, A.G.G.M.; Schlathölter, T., *Ionization and Fragmentation of Anthracene Upon Interaction with keV Protons and  $\alpha$  Particles*, Volume 708, Issue 1, pp. 435 – 444, The Astrophysical Journal, December (2009).
- [39] Yerlekar, A.; Kshirsagar, M.M., “*A Review on Mass Spectrometry: Technique and Tools*”, p. 17, Volume 4, Issue 4 (Version 4), International Journal of Engineering Research and Applications, April (2014).
- [40] Dillard, J.G., “*Negative Ion Mass Spectrometry*”, p. 589, Department of Chemistry, Virginia Polytechnic Institute and State University, Blacksburg, 25 April 1973.
- [41] Johnstone, R.A.W.; Rose, M.E., “*Mass Spectrometry for Chemists and Biochemists*”, Second Edition, p. 9, Cambridge University Press (1996).
- [42] Smith, R.M., “*Understanding Mass Spectra: A Basic Approach*”, Second Edition, p.2, John Wiley & Sons, Inc. (2004).
- [43] de Hoffman, E.; Stroobant, V., “*Mass Spectrometry: Principles and Applications*”, Third Edition, pp. 10 – 11, John Wiley & Sons Ltd. (2007).
- [44] de Hoffman, E.; Stroobant, V., “*Mass Spectrometry: Principles and Applications*”, Third Edition, p. 15, John Wiley & Sons Ltd. (2007).
- [45] Rosenthal, N.; Harvey, R.P., “*Heart Regeneration and Development*”, Volume 1, p. 812, Academic Press (2012).
- [46] Clark, J., “*The Mass Spectrometer: An Outline of What Happens in a Mass Spectrometer*”, Chemguide (2000). Retrieved from:

- <http://www.chemguide.co.uk/analysis/masspec/howitworks.html>. [Accessed 25 January 2017].
- [47] McLafferty, F.W.; Tureček, F., *“Interpretation of Mass Spectra”*, Fourth Edition, pp. 35 – 36, University Science Books California (1993).
- [48] de Hoffman, E.; Stroobant, V., *“Mass Spectrometry: Principles and Applications”*, Third Edition, p. 16, John Wiley & Sons Ltd. (2007).
- [49] Smith, R.M., *“Understanding Mass Spectra: A Basic Approach”*, Second Edition, p. 8, John Wiley & Sons, Inc. (2004).
- [50] Atkinson, J.; Hibbert, C., *“Advanced Level Chemistry”*, pp. 8 – 9, Heinemann Educational Publishers, Oxford (2000).
- [51] Telle, H.H.; Ureña, Á.G.; Donovan, R.J., *“Laser Chemistry: Spectroscopy, Dynamics and Applications”*, p. 198, John Wiley and Sons Ltd, West Sussex (2007).
- [52] de Hoffman, E.; Stroobant, V., *“Mass Spectrometry: Principles and Applications”*, Third Edition, p. 175, John Wiley & Sons Ltd. (2007).
- [53] Shrader, S., *“Introductory Mass Spectrometry”*, Second Edition, p. 1, CRC Press, Florida (2013).
- [54] Herbert, C.G.; Johnstone, R.A.W., *“Mass Spectrometry Basics”*, pp. 183 – 186, CRC Press, Florida (2003).
- [55] Gates, P., *Quadrupole Mass Analysis*, University of Bristol, June 2014.  
Retrieved from:  
<http://www.chm.bris.ac.uk/ms/quadrupole.xhtml> [Accessed 25 January 2017].
- [56] Yost, R.A.; Enke, C.G., *“Triple Quadrupole Mass Spectrometry for Direct Mixture Analysis and Structure Elucidation”*, Volume 51, Issue 12, pp. 1251 – 1264, Analytical Chemistry, ACS Publications (1979).
- [57] Syed, S.U.A.H.; Maher, S.; Taylor, S., *“Quadrupole Mass Filter Operation Under the Influence of Magnetic Field”*, Volume 48, Issue 12, p. 1325, Journal of Mass Spectrometry (2013).

- [58] University of Kentucky Mass Spectrometer Facility, “*Summary of the characteristics of different mass analysers*”, pp. 3 – 6, University of Kentucky. [Accessed 25 January 2017]. Retrieved from:  
<http://www.research.uky.edu/core/massspec/jeolanalyzers.pdf>.
- [59] Trivedi, V.; Chaudhary, N., “*Spectroscopic Techniques: Magnetic Sector*”, p. 2, Bioanalytical Techniques and Bioinformatics, National Programme on Technology Enhanced Learning (NPTEL). Retrieved from:  
<http://nptel.ac.in/courses/102103044/module2/lec12/2.html>. [Accessed 25 January 2017].
- [60] EPA Clean-Up Information Site. Retrieved from:  
<https://clu.in.org/characterization/technologies/windows/msector.htm>. [Accessed 23 June 2017].
- [61] Van Bramer, S., “*An Introduction to Mass Spectrometry: Magnetic Sector*”, Department of Chemistry, Widener University (1997). Retrieved from:  
[http://science.widener.edu/svb/massspec/intro\\_to\\_ms/magnet.html](http://science.widener.edu/svb/massspec/intro_to_ms/magnet.html). [Accessed 25 January 2017].
- [62] Haven, M.C.; Tetrault, G.A.; Schenken, J.R., “*Laboratory Instrumentation*”, Fourth Edition, pp. 300 – 301, John Wiley & Sons Ltd, USA (1995).
- [63] Shimadzu Analytical and Measuring Instruments “*Introduction to LC-MS: Magnetic Sector MS*”. Retrieved from:  
<http://www.shimadzu.com/an/hplc/support/lib/lctalk/60/60intro.html>. [Accessed 25 January 2017].
- [64] de Hoffman, E.; Stroobant, V., “*Mass Spectrometry: Principles and Applications*”, Third Edition, p. 88, John Wiley & Sons Ltd. (2007).
- [65] Syka, J.E.P.; Bai, D.L., *et al.* *A Linear Quadrupole Ion Trap Fourier Transform Mass Spectrometer, A New Tool for Proteomics* 49th ASMS Conference on Mass Spectrometry and Allied Topics (2001) Chicago, Illinois.
- [66] March, R.E., “*Quadrupole Ion Traps*”, Volume 26, Issue 6, pp. 961-989, Mass Spectrometry Reviews, November/December (2009).

- [67] Newtonian Labs, “*Newtonian Labs Teaching Guides: The Physics of Electrodynamic Ion Traps*”, p. 2, Newtonian Labs, California. Retrieved from: <http://newtonianlabs.com/eit/IonTrapPhysics.pdf>. [Accessed 26 January 2017].
- [68] March, R.E., *Quadrupole Ion Traps*, Volume 26, Issue 6, p. 966, Mass Spectrometry Reviews, November/December 2009.
- [69] de Hoffman, E.; Stroobant, V., “*Mass Spectrometry: Principles and Applications*”, Third Edition, p. 100, John Wiley & Sons Ltd. (2007).
- [70] March, R.E., “*An Introduction to Quadrupole Ion Trap Mass Spectrometry*”, Volume 32, Issue 4, p.351, Journal of Mass Spectrometry (1997).
- [71] Gillaspay, J., “*Trapping Highly Charged Ions: Fundamentals and Applications*”, p. 200, Nova Science Publishers Inc. (2001).
- [72] March, R.E.; Todd, J.F.J., “*Practical Aspects of Ion Trap Mass Spectrometry: Volume 2, Ion Trap Instrumentation*”, p. 239, CRC Press LLC, Florida (1995).
- [73] Blaum, K.; Novikov, Y.M.; Werth, G., *Penning traps as a versatile tool for precise experiments in fundamental physics*, Volume 51, Issue 2, p. 151, Contemporary Physics, March/April 2010.
- [74] Blaum, K.; Sturm, S., “*Penning Traps: Precision Measurements on Single Ions*”, Max Planck Institute for Nuclear Physics, n.d. [Accessed 26 January 2017].
- [75] Brown, L.S.; Gabrielse, G., “*Geonium theory: Physics of a single electron or ion in a Penning trap*”, Volume 58, Issue 1, p. 235, Reviews of Modern Physics (1986).
- [76] Seccombe, D.P.; Reddish, T.J., *Theoretical study of space focusing in linear time-of-flight mass spectrometers*, Volume 72, Issue 2, p. 1330, Review of Scientific Instruments, February 2001.
- [77] Wiley, W.C.; McLaren, I.H., “*Time-of-Flight Mass Spectrometer with Improved Resolution*”, Volume 26, Issue 12, pp. 1150 – 1151, The Review of Scientific Instruments, December (1955).
- [78] Yale Johnson Lab, “*Photofragmentation Mass Spectrometry*”, May (2012). Retrieved from: <http://jlab.chem.yale.edu/research/techniques/photofragmentation-mass>

spectrometry. [Accessed 10 February 2017].

- [79] de Hoffman, E.; Stroobant, V., “*Mass Spectrometry: Principles and Applications*”, Third Edition, pp. 126 – 131, John Wiley & Sons Ltd. (2007).
- [80] Mamyryn, B.A.; Karataev, V.I.; Shmikk, D.V.; Zagulin, V.A., “*The mass reflectron, a new nonmagnetic time-of-flight mass spectrometer with high resolution*”, Volume 37, Issue 1, pp. 45 – 48, Journal of Experimental and Theoretical Physics, July (1973).
- [81] Mamyryn, B.A., “*Time-of-flight mass spectrometry (concepts, achievements, and prospects)*”, Volume 206, Issue 3, p. 251 – 266, International Journal of Mass Spectrometry, March (2001).
- [82] Lebedev, A., “*Comprehensive Environmental Mass Spectrometry*”, p. 5, ILM Publications, Hertfordshire (2012).
- [83] Barber, M.; Bordoli, R.S.; Elliott, G.J.; Sedgwick, R.D.; Tyle, A.N., *Fast Atom Bombardment Mass Spectrometry*, Volume 54, Issue 4, pp. 645 – 657, Analytical Chemistry, April (1982).
- [84] Koel, M., “*Analytical Chemistry: Ionic Liquids in Chemical Analysis*”, p. 376, CRC Press, Florida (2009).
- [85] Pavia, D.L.; Lampman, G.M.; Kriz, G.S.; Vyvyan, J.A., “*Introduction to Spectroscopy*”, Fifth Edition, p. 115, Cengage Learning, Stamford (2014).
- [86] Ham, B.M.; MaHam, A., “*Analytical Chemistry: A Chemist and Laboratory Technician’s Toolkit*”, p. 486, John Wiley & Sons Ltd, New Jersey (2016).
- [87] Herron, J.N.; Jiskoot, W.; Crommelin, D.J.A., “*Pharmaceutical Biotechnology Volume 7: Physical Methods to Characterize Pharmaceutical Proteins*”, p. 148, Springer Science+Business Media, New York (1995).
- [88] Barner-Kowollik, C.; Gründling, T.; Falkenhagen, J.; Weidner, S., “*Mass Spectrometry in Polymer Chemistry*”, p. 42, Wiley-VCH Verlag and Co., Weinheim (2012).
- [89] Camilleri, P., “*Capillary Electrophoresis: Theory and Practice*”, Second Edition, p. 57, CRC Press, Florida (1998).

- [90] Andrews, D.L., "*Perspectives in Modern Chemical Spectroscopy*", p. 267, Springer-Verlag Berlin Heidelberg (1990).
- [91] de Hoffman, E.; Stroobant, V., "*Mass Spectrometry: Principles and Applications*", Third Edition, p. 30, John Wiley & Sons Ltd. (2007).
- [92] Smith, R.E., "*Medicinal Chemistry - Fusion of Traditional and Western Medicine*", p. 220, Bentham Science Publishers (2013).
- [93] Tanaka, K.; Waki, H.; Ido, Y.; Akita, S.; Yoshida, Y.; Yoshida, T., *Protein and polymer analyses up to m/z 100 000 by laser ionization time-of-flight mass spectrometry*, Volume 2, Issue 8, pp. 151-153, Rapid Communications in Mass Spectrometry, August 1988.
- [94] El-Aneed, A.; Cohen, A.; Banoub, J., *Mass Spectrometry, Review of the Basics: Electrospray, MALDI, and Commonly Used Mass Analyzers*, Volume 44, Issue 3, pp. 215 – 218, Applied Spectroscopy Reviews, 2009.
- [95] Dreisewerd, K., *Recent methodological advances in MALDI mass spectrometry*, Volume 406, Issue 9-10, pp. 2261 – 2278, Analytical and Bioanalytical Chemistry, April 2014.
- [96] Knochenmuss, R., *MALDI and Related Methods: A solved problem or still a mystery?* Volume 2, Special Issue S0006, Mass Spectrometry Tokyo, April 2013.
- [97] Ho, C.S.; Lam, C.W.K.; Chan, M.H.M.; Cheung, R.C.K.; Law, L.K.; Lit, L.C.W.; Ng, K.F.; Suen, M.W.M.; Tai, H.L., *Electrospray Ionisation Mass Spectrometry: Principles and Clinical Applications*, Volume 24, issue 1, pp. 3 – 12, Clinical Biochemist Review, 2003.
- [98] Cole, R.B., *Some tenets pertaining to Electrospray Ionisation Mass Spectrometry*, Volume 35, Issue 7, pp. 763 – 772, Journal of Mass Spectrometry, July 2000.
- [99] Wang, G.; Cole, R.B., *Electrospray Ionisation Mass Spectrometry: Fundamentals, Instrumentation and Applications*, pp. 137 – 174, John Wiley & Sons, New York, 1997.
- [100] de Hoffman, E.; Stroobant, V., *Mass Spectrometry: Principles and Applications*, Third Edition, p. 15 – 17, John Wiley & Sons Ltd. (2007).

- [101] Ashcroft, A.E., *Ionisation Methods in Organic Mass Spectrometry*, p. 61, The Royal Society of Chemistry (1997).
- [102] Gross, J.H., *Mass Spectrometry: A Textbook*, pp. 196 – 201, Springer-Verlag Berlin Heidelberg (2004).
- [103] Weissler, G.L.; Carlson, R.W., *Vacuum Physics and Technology*, Volume 14, 1<sup>st</sup> Edition, pp. 247 – 253, Academic Press, New York (1979).
- [104] Weissler, G.L.; Carlson, R.W., *Vacuum Physics and Technology*, Volume 14, 1<sup>st</sup> Edition, pp. 114 – 117, Academic Press, New York (1979).
- [105] Osaka Vacuum Ltd., *Turbo Molecular Pump Exhaust Theory*, (2010).  
Retrieved from:  
[http://www.osakavacuum.co.jp/en/products/pump\\_turbo/tgf/tg1100f/tg1100f.html](http://www.osakavacuum.co.jp/en/products/pump_turbo/tgf/tg1100f/tg1100f.html). [Accessed 29 November 2016].
- [106] Herring, D., *Oil Sealed Rotary Vane Pumps Part 1*, Vac Aero International Inc., February (2016). Retrieved from: <https://vacaero.com/information-resources/practical-vacuum-pump-practice-with-dan-herring/1477-oil-sealed-rotary-vane-pumps-part-1.html>. [Accessed 29 November 2016].
- [107] Vacuum Gauges and Control Instrumentation, *BA600 Series Principle of Operation*, Instrutech (n.d.). Retrieved from: <http://www.instrutechinc.com/nude-glass-ig-faq/>. [Accessed 3 July 2017].
- [108] Alpert, D.; Buritz, R.S., *UltraHigh Vacuum. II. Limiting Factors on the Attainment of Very Low Pressures*, Volume 25, Issue 202, Journal of Applied Physics (1953).
- [109] Kurt J. Lesker Company, *Pressure Measurement Technical Notes*, (2016).  
Retrieved from:  
[http://www.lesker.com/newweb/gauges/gauges\\_technicalmnotes\\_1.cfm](http://www.lesker.com/newweb/gauges/gauges_technicalmnotes_1.cfm).  
[Accessed 29 November 2016].
- [110] O' Hanlon, J.F., *A User's Guide to Vacuum Technology*, Third Edition, pp. 88 – 89, John Wiley & Sons Inc., New Jersey (2003).
- [111] Wiza, J.L., *Microchannel Plate Detectors*, Vol. 162 (Issue 1-3), p. 1, Nuclear Instruments and Methods (1979).

- [112] Safvan, C.P., *Micro Channel Plate Detector*, Inter-University Accelerator Centre (IUAC), August (2014). Retrieved from: <http://www.iuac.res.in/atmol/~safvan/mridulathesis/node21.html>. [Accessed 29 November 2016].
- [113] Seyfert, P., *Photon Detector Development for the PANDA RICH*, University of Heidelberg, Germany (n.d.). Retrieved from: <https://mathphys.fsk.uni-heidelberg.de/~pseyfert/gsireport.pdf>. [Accessed 11 July 2017].
- [114] Adams, J.; Manley, B.W., *The Mechanism of Channel Electron Multiplication*, Vol. 13 (Issue 3), p. 88, IEEE Transactions on Nuclear Science, June (1966).
- [115] Hamamatsu Photonics, *Photomultiplier Tube: Basics and Applications: Chapter 10 MCP-PMT*, Third Edition (Edition 3a), p. 196, Hamamatsu Photonics K. K. (2007). Retrieved from: [https://www.hamamatsu.com/resources/pdf/etd/PMT\\_handbook\\_v3aE-Chapter10.pdf](https://www.hamamatsu.com/resources/pdf/etd/PMT_handbook_v3aE-Chapter10.pdf). [Accessed 29 November 2016].
- [116] Bolton, P.R.; Borghesi, M.; Brenner, C.; Carroll, D.C.; De Martinis, C.; Fiorini, F.; Flacco, A.; Floquet, V.; Fuchs, J.; Gallegos, P.; Giove, D.; Green, J.S.; Green, S.; Jones, B.; Kirby, D.; McKenna, P.; Neely, D.; Nuesslin, F.; Prasad, R.; Reinhardt, S.; Rothl, M.; Schramm, U.; Scott, G.G.; Ter-Avetisyan, S.; Tolley, M.; Turchetti, G.; Wilkens, J.J., *Instrumentation for Diagnostics and Control of Laser-Accelerated Proton (Ion) Beams*, Volume 30, p. 261, Physica Medica, May (2014).
- [117] Stanford Research Systems, *DG535 Digital Delay Pulse Generator Features*, Scientific Instruments. Retrieved from: <http://www.thinksrs.com/products/DG535.htm>. [Accessed 16<sup>th</sup> February 2017].
- [118] Ortec (Ametek), *9327 1-GHz Amplifier and Timing Discriminator*, User Manual. Retrieved from: <http://www.ortec-online.com//media/ametekortec/brochures/9327.pdf>. [Accessed 17<sup>th</sup> August 2017]
- [119] Hoagland, T., *A Brief Description of Discriminators*, NSCLdocs, December (2004). Retrieved from: <http://docs.nscl.msu.edu/daq/samples/Discriminators.pdf>. [Accessed 14<sup>th</sup> August 2017].
- [120] FAST ComTEC, *Model 7886 2 GHz Multiscaler User Manual*, 2.1, September (1998).

- [121] Barrett, G.T., *Development of an Apparatus for the Study of Electron Impact Fragmentation of Molecular Clusters*, MSc Thesis, National University of Ireland Maynooth, October (2008).
- [122] Becker, J.; Wentrup, C.; Katz, E.; Zeller, K.P., *Azulene-naphthalene rearrangement. Involvement of 1-phenylbuten-3-ynes and 4-phenyl-1,3-butadienylidene*, Volume 102, Issue 15, pp. 5110 – 5112, Journal of the American Chemical Society (1980).
- [123] Dyakov, Y.A.; Ni, C.K.; Lin, S.H.; Lee, Y.T.; Mebel, A.M., *Ab initio and RRKM study of photodissociation of azulene cation*, Volume 8, Issue 12, pp. 1349 – 1464, Physical Chemistry Chemical Physics (2006).
- [124] Jynto, *Picture of Anthracene*, Wikipedia Commons. Retrieved from: [https://commons.wikimedia.org/wiki/File:Anthracene\\_molecule\\_ball.png](https://commons.wikimedia.org/wiki/File:Anthracene_molecule_ball.png). Made using Accelrys Discovery Studio Visualizer. [Accessed 6<sup>th</sup> September 2017].
- [125] Postma, J.; Hoekstra, R.; Tielens, A.G.G.; Schlathölter, T., *A Molecular Dynamics Study on Slow Ion Interactions with the Polycyclic Aromatic Hydrocarbon Molecule Anthracene*, Volume 783, Issue 1, The Astrophysical Journal (2014).
- [126] Reitsma, G.; Zettergren, H.; Martin, S.; Brédy, R.; Chen, L.; Bernard, J.; Hoekstra, R.; Schlathölter, T., *Activation energies for fragment channels of anthracene dications – experiment and theory*, Volume 45, Issue 21, Journal of Physics B: Atomic, Molecular and Optical Physics (2012).
- [127] Stahl, D.; Maquin, F., *Charge-stripping mass spectrometry of molecular ions from polyacenes and molecular orbital theory*, Volume 108, Issue 6, pp. 613 – 617, Chemical Physical Letters, July (1984).
- [128] Mallocci, G.; Cappellini, G.; Mulas, G.; Mattoni, A., *Electronic and optical properties of families of polycyclic aromatic hydrocarbons: A systematic (time dependent) density functional theory study*, Volume 384, Issues 1-3, pp. 19 – 27, Chemical Physics, June (2011).

## Appendix

Peter J.M. van der Burgt, Melissa Dunne, and Marcin L. Gradziel, *Hydrogen rearrangements in the fragmentation of anthracene by low-energy electron impact*, Eur. Phys. J. D (2018) 72: 31.

# Hydrogen rearrangements in the fragmentation of anthracene by low-energy electron impact<sup>\*</sup>

Peter J.M. van der Burgt<sup>a</sup>, Melissa Dunne, and Marcin L. Gradziel

Department of Experimental Physics, National University of Ireland Maynooth, Maynooth, Co. Kildare, Ireland

Received 29 September 2017 / Received in final form 24 November 2017

Published online 6 February 2018 – © EDP Sciences, Società Italiana di Fisica, Springer-Verlag 2018

**Abstract.** We have measured mass spectra for positive ions produced by low-energy electron impact on anthracene using a reflectron time-of-flight mass spectrometer. The electron impact energy has been varied from 0 to 100 eV in steps of 0.5 eV. Ion yield curves of most of the fragment ions have been determined by fitting groups of adjacent peaks in the mass spectra with sequences of normalized Gaussians. Appearance energies for all these ions have been determined, and we report the first direct measurement of the triple ionization energy of anthracene at  $45.5 \pm 0.5$  eV. The groups of fragments containing 8–13 carbon atoms provide evidence for hydrogen rearrangements during the fragmentation, involving retention or loss of one or two additional hydrogen atoms. Groups of fragments with 6 and 7 carbon atoms clearly show the presence of doubly-charged fragments. The smaller fragments with 1–4 carbon atoms all show broadened peaks, and these fragments may be partly or mostly due to energetic charge-separation fragmentations of doubly-charged anthracene.

## 1 Introduction

Polycyclic aromatic hydrocarbons (PAHs) have been studied extensively in recent years, because of their relevance in astrophysical processes and in environmental chemistry. The infrared spectra of most interstellar objects are dominated by emission bands that are commonly attributed to PAH molecules [1]. PAHs are susceptible to hydrogen attachment and are considered to play a key role as catalysts in the formation of molecular hydrogen in the interstellar medium [2,3]. PAHs are also considered as essential components in the pathway to the origin of life [4]. In the Earth's environment, PAHs are widespread pollutants generated by the combustion of organic materials, and are of concern because many PAHs have toxic, mutagenic and/or carcinogenic properties [5,6].

The topic of this paper is the fragmentation of the PAH anthracene ( $C_{14}H_{10}$ ) induced by low-energy electron impact. Electron induced processes are of high relevance in a number of different areas. Many molecular species in the interstellar medium are assumed to be formed by chemical reactions within the ice mantles on interstellar dust grains caused by irradiation of ultraviolet light and cosmic rays. This irradiation releases many secondary electrons which may themselves induce chemical reactions [7]. Low-energy collisions of electrons with molecules are important elementary processes in gaseous environments

such as discharges, gas lasers and the Earth's atmosphere [8], and in focused electron beam induced deposition [9].

Collision induced fragmentation of anthracene and other PAHs has been the focus of extensive research. Several groups have published mass spectra of anthracene at 70 eV electron energy [10–13] and have determined the ionization energy of anthracene [10,14]. Man et al. [15] have studied excitation of anthracene by electron impact. The mass spectra of singly-charged ions produced by doubly- and triply-charged anthracene molecules have been obtained at 70 eV [13] and at 100 eV [16] electron impact. At 70 eV the preferred routes for charge separation of doubly-charged anthracene ions lead to the singly-charged fragments  $CH_3^+$ ,  $C_2H_2^+$  and  $C_3H_3^+$  [13], and this has also been observed with 40.8 eV photon impact [17].

Tobita et al. [18] have studied both electron and photon impact and have determined single and double ionization energies. Photoionization studies with synchrotron radiation and other light sources have been performed by Hagan and Eland [17], Jochims et al. [19,20], Ling and Lifshitz [21] and Mayer et al. [22]. A detailed fragmentation study of laser desorbed anthracene in intense laser fields was performed by Robson et al. [23], showing the presence of doubly and triply charged fragments in the mass spectra. Murakami et al. [24] have performed measurements with fs circularly polarized laser light. Using synchrotron radiation, Hartman et al. [25,26] have measured the ratios of doubly to singly-charged molecular parent ions for anthracene and other aromatic hydrocarbons. Wehlitz [27] has reviewed double photoionization of hydrocarbons and aromatic molecules.

<sup>\*</sup> Contribution to the Topical Issue “Low Energy Positron and Electron Interactions”, edited by James Sullivan, Ron White, Michael Bromley, Ilya Fabrikant, and David Cassidy.

<sup>a</sup> e-mail: [peter.vanderburgt@nu.ie](mailto:peter.vanderburgt@nu.ie)

Ion collisions with PAHs have been studied recently by several groups and we refer to the review paper by Gatchell and Zettergren [28] for a comprehensive discussion. Postma et al. [29] report anthracene mass spectra obtained by impact with keV  $\text{H}^+$  and  $\text{He}^{2+}$  ions. Brédy et al. [30] have studied fragmentation of anthracene induced by collisions with 40 keV  $\text{Ar}^{8+}$  ions. Using a coincident detection technique they measured mass spectra of anthracene ions differentiated by the charge  $r$  ( $1 \geq r \geq 4$ ) of the parent ion  $\text{C}_{14}\text{H}_{10}^{r+}$ . The mass spectra in both these papers show the clear presence of doubly-charged fragments.

The fragmentation of doubly-charged anthracene formed in double-charge-transfer reactions of singly-charged ions with neutral anthracene has been studied by Martin et al. [31] and Reitsma et al. [32]. Johansson et al. [33] have performed collision induced dissociation experiments of 50 keV anthracene cations colliding with xenon atoms and have performed density functional calculations on possible fragmentation pathways for the loss of  $\text{C}_2\text{H}_2$ . Holm et al. [34] and Rousseau et al. [35] have measured mass spectra produced by low-energy ions interacting with anthracene clusters.

Calculated ionization and dissociation energies are reported by Zakrzewski et al. [36], Kukhta et al. [37] and Holm et al. [38]. Sanz et al. [39] have calculated electron scattering cross sections from anthracene over the energy range 0.00001–10 000 eV. Postma et al. [40] have performed a molecular dynamics simulation of slow ion collisions with anthracene.

The focus of this article is on electron induced fragmentation processes in anthracene. In the following sections we give an overview of the experiment, the data acquisition and the data analysis. We then present our results and compare these with other research. The two main focal points of the discussion are the evidence for hydrogen rearrangements, and the identification of multiply charged fragments.

## 2 Experiment

The experimental set-up consists of a resistively heated oven producing an effusive beam of anthracene molecules, a pulsed electron beam, and a reflectron time-of-flight mass spectrometer, housed in three inter-connected and differentially pumped vacuum chambers. The set-up has been used before for the study of nucleobases [41–43].

The molecular beam of anthracene is generated by heating the oven containing anthracene powder (99% purity from Sigma–Aldrich) to a temperature of 100 °C. Molecules are effusing from a capillary (0.5 mm diameter and 4.5 mm length) in the oven and pass through a skimmer (1.2 mm diameter) into the collision chamber where they are collided with electrons.

The electron gun is pulsed at a rate of 8 kHz with a 0.3  $\mu\text{s}$  pulse width. The energy resolution of the electron beam is about 0.8 eV FWHM. The electron gun has been optimised in pulsed mode by maximizing the current on the Faraday cup and ensuring that the current was independent of electron impact energy. In this way an electron

beam has been obtained with a total current that was constant down to 15 eV and dropped to 60% at 8 eV.

Positively charged fragments are extracted into the mass spectrometer 0.05  $\mu\text{s}$  after the electron pulse. A delay generator (Stanford Research Systems DG535) is used to synchronise the pulsing of the electron gun, the ion extraction voltage, and the start of the multichannel scaler (FastComtec 7886S).

Data acquisition is controlled by LabVIEW code, which ramps the electron impact energy in 0.5 eV steps, acquires mass spectra as a function of electron impact energy, and adds each mass spectrum to the data already accumulated. The full data set consists of a two-dimensional array of ion yield as a function of time-of-flight and of electron impact energy. After each scan of the electron impact energy, which takes about two hours, the full data set is written to a file. The data set used for this paper consists of 23 scans of the electron impact energy. Comparison of mass spectra taken before, during and after the data acquisition shows no sign of thermal decomposition or other undesired effects.

## 3 Data analysis

The data analysis is essentially the same as described in earlier papers [41–43]. The mass resolution in the mass spectra is  $\Delta m/m = 0.004$  at 178 u at 100 eV. Above 34 u adjacent peaks in the mass spectra are not fully resolved, and ion yield curves have been extracted from the full data set by fitting groups of adjacent peaks with sequences of normalized Gaussians.

A remnant of water vapour in the vacuum system produces peaks at 16–18 u in the mass spectra. The 17 u and 18 u ion yield curves have been used for calibration of the incident electron energy by comparison with the recommended ionization cross sections for the production of  $\text{H}_2\text{O}^+$  and  $\text{OH}^+$  in Itikawa and Mason [44] (Tab. 11) in the range 10–40 eV. The estimated error in the calibration is  $\pm 0.2$  eV.

Appearance energies (first onsets) have been determined by fitting an onset function  $f(E) = c(E - E_0)^p$  convoluted with a Gaussian to each of the ion yield curves. For second onsets an additional term was included in the onset function.

## 4 Results and discussion

### 4.1 Mass spectra

In the remainder of this article we will identify groups of peaks in our mass spectra by the number of carbon atoms contained in the fragments. Group 14 is the parent ion group, containing the masses 174 u to 180 u. Group 7 contains half-integer masses, and this group contains singly-charged fragments with 7 carbon atoms and doubly-charged fragments with 14 carbon atoms. Figure 1 shows the mass spectrum of anthracene at 70 eV electron impact energy. The ions in group 14 have the highest abundance, followed by the ions in groups 7 and 6. The

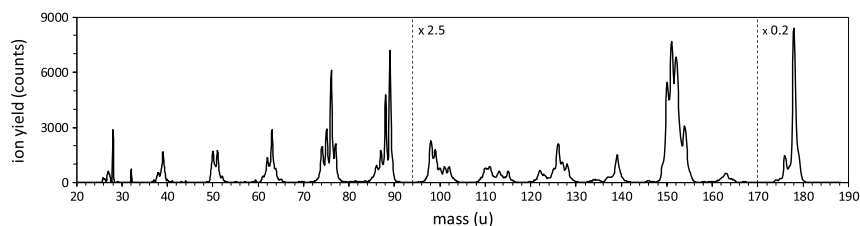


**Fig. 1.** The mass spectrum of anthracene at 70 eV electron impact energy. The peaks at 28 u and 32 u are due to a remnant of air in the vacuum chamber. For clarity, the ion yield between 94 u and 170 u is multiplied by 2.5, and the ion yield above 170 u is multiplied by 0.2. At 70 eV the yield in the parent ion group (172–180 u) is 45% of the total ion yield.

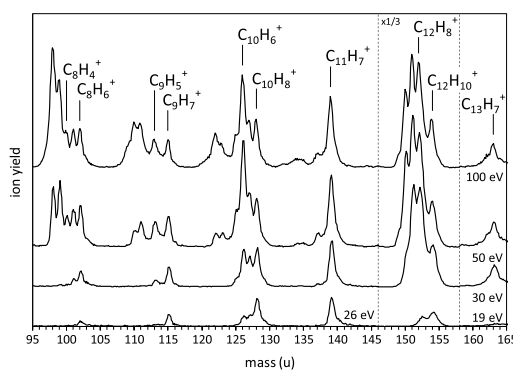


**Fig. 2.** Mass spectra of anthracene for the mass range 95–165 u, showing evidence for hydrogen rearrangements in the formation of fragments with 8–13 carbon atoms. The ion yield between 146 u and 158 u is scaled with a factor 1/3.

relative yields of ions in our mass spectrum at 70 eV compare reasonably well with those in Table 1 of Wacks and Dibeler [10], but for 39 u, 50–51 u, 74–75 u and 77 u we observe yields that are about 30% higher.

Evidence for hydrogen rearrangements is provided by some of the fragments in groups 8–13. Figure 2 shows the mass spectra for groups 8–13 at different electron impact energies. Fragmentation processes in relation to these groups are discussed in Section 4.3.

Evidence for the presence of doubly-ionized fragments is provided by peaks at half-integer masses in groups 6 and 7. 89 u and 77 u are mostly due to doubly-charged fragments. Groups 1 and 2 clearly show broadened peaks at integer masses, indicating that these are due to singly-charged fragments formed with a range of kinetic energies. Groups 3–5 feature broadened peaks of singly-charged fragments or peaks at non-integer masses due to multiply-charged fragments, or a combination of both. All these groups are discussed in Section 4.4.

Using femtosecond laser mass spectrometry, Robson et al. [23] have observed that the ratio of 89.5 u to 89 u is equal to the isotope ratio 179 u/178 u. Because the only possible configuration for 89.5 u is  $C_{13}^{13}CH_{10}^{++}$ , 89 u must be predominantly the doubly-charged parent. Postma et al. [29] have observed the same in ion-impact mass spectrometry. We observe that

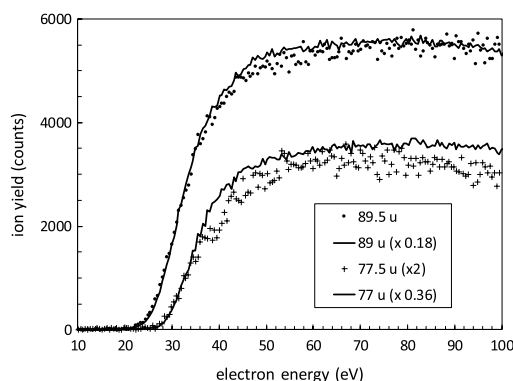


**Fig. 3.** Ion yield curves for 89.5 u, 89 u, 77.5 u, and 77 u. The only possible configurations for 89.5 u and 77.5 u are  $C_{13}^{13}CH_{10}^{++}$  and  $C_{11}^{13}CH_{10}^{++}$ , respectively. The measured isotope ratio 179/178 u is  $0.18 \pm 0.01$ , which implies that 89 u is almost entirely  $C_{14}H_{10}^{++}$ , and 77 u is mostly  $C_{12}H_{10}^{++}$ . For further discussion see Section 4.1.

the 89.5 u/89 u and 179 u/178 u ratios are both equal to  $0.18 \pm 0.01$ , and are constant from 100 eV down to about 30 eV (below this energy statistical fluctuations in the 89.5 u ion yield affect the ratio). In Figure 3 the ion yield curves of 89 u and 89.5 u are compared, showing that both ion yield curves have the same shape within statistical error.

Wacks and Dibeler [10] observed that the 76.5 u/76 u ratio at 70 eV is equal to the isotope ratio, and deduced that the peaks in group 6 are primarily due to multiply charged ions. However, in our mass spectra the 76.5 u/76 u ratio = 0.22. The 77.5 u/77 u ratio is more relevant, because the only possible configuration for 77.5 u is  $C_{11}^{13}CH_{10}^{++}$ . We observe the 77.5 u/77 u ratio to be slightly lower than the isotope ratio and approximately constant between 30 and 100 eV. Figure 3 shows that the ion yield curves of 77 u and 77.5 u have nearly the same shape within statistical error.

## 4.2 Appearance energies

We have determined the appearance energies for most of the fragments of anthracene, and the results are listed in Table 1. The errors stated in Table 1 have been obtained

**Table 1.** Appearance energies and second onsets for anthracene fragments determined in this work.

Group	m/q (u)	Assignment	Appearance energy (eV)	Second onset (eV)
1	15	CH <sub>3</sub> <sup>+</sup>	17.7 ± 3.2	37.7 ± 1.0
2	26	C <sub>2</sub> H <sub>2</sub> <sup>+</sup>	31.0 ± 0.6	
	27	C <sub>2</sub> H <sub>3</sub> <sup>+</sup>	32.0 ± 0.8	
3	37	C <sub>3</sub> H <sup>+</sup>	44.1 ± 1.8	58.3 ± 1.4
	38	C <sub>3</sub> H <sub>2</sub> <sup>+</sup>	34.9 ± 0.6	
	39	C <sub>3</sub> H <sub>3</sub> <sup>+</sup>	21.0 ± 1.0	29.4 ± 1.3
	40	C <sub>3</sub> H <sub>4</sub> <sup>+</sup>	32.9 ± 0.9	
4	49	C <sub>4</sub> H <sup>+</sup>	33.5 ± 0.9	60.3 ± 1.2
	50	C <sub>4</sub> H <sub>2</sub> <sup>+</sup>	25.7 ± 1.1	31.7 ± 1.5
	51	C <sub>4</sub> H <sub>3</sub> <sup>+</sup>	26.4 ± 1.4	30.9 ± 0.5
	52	C <sub>4</sub> H <sub>4</sub> <sup>+</sup>	24.9 ± 1.1	30.8 ± 0.8
	53	C <sub>4</sub> H <sub>5</sub> <sup>+</sup>	26.2 ± 1.0	
5	59.333	C <sub>14</sub> H <sub>10</sub> <sup>+++</sup>	45.5 ± 0.5	
	61	C <sub>5</sub> H <sup>+</sup> /C <sub>10</sub> H <sub>2</sub> <sup>++</sup>	39.5 ± 0.7	48.7 ± 1.2
	61.5	C <sub>10</sub> H <sub>3</sub> <sup>++</sup>	44.9 ± 0.8	
	62	C <sub>5</sub> H <sub>2</sub> <sup>+</sup> /C <sub>10</sub> H <sub>4</sub> <sup>++</sup>	33.0 ± 0.6	37.9 ± 0.7
	62.5	C <sub>10</sub> H <sub>5</sub> <sup>++</sup>	41.2 ± 0.7	
	63	C <sub>5</sub> H <sub>3</sub> <sup>+</sup> /C <sub>10</sub> H <sub>6</sub> <sup>++</sup>	26.0 ± 0.9	
	63.5	C <sub>10</sub> H <sub>7</sub> <sup>++</sup>	35.0 ± 0.7	
	64	C <sub>5</sub> H <sub>4</sub> <sup>+</sup> /C <sub>10</sub> H <sub>8</sub> <sup>++</sup>	28.9 ± 1.0	33.7 ± 0.7
	64.5	C <sub>10</sub> H <sub>9</sub> <sup>++</sup>	30.0 ± 0.6	
	65	C <sub>5</sub> H <sub>5</sub> <sup>+</sup> /C <sub>10</sub> H <sub>10</sub> <sup>++</sup>	26.9 ± 0.5	
6	73	C <sub>6</sub> H <sup>+</sup>	51.7 ± 1.3	
	74	C <sub>6</sub> H <sub>2</sub> <sup>+</sup> /C <sub>12</sub> H <sub>6</sub> <sup>++</sup>	28.5 ± 0.9	34.1 ± 0.8
	74.5	C <sub>12</sub> H <sub>5</sub> <sup>++</sup>	31.3 ± 0.7	
	75	C <sub>6</sub> H <sub>3</sub> <sup>+</sup> /C <sub>12</sub> H <sub>6</sub> <sup>++</sup>	29.1 ± 0.5	
	75.5	C <sub>12</sub> H <sub>7</sub> <sup>++</sup>	28.6 ± 0.6	37.6 ± 0.5
	76	C <sub>6</sub> H <sub>4</sub> <sup>+</sup> /C <sub>12</sub> H <sub>8</sub> <sup>++</sup>	27.2 ± 1.2	30.5 ± 0.5
	76.5	C <sub>12</sub> H <sub>9</sub> <sup>++</sup>	29.2 ± 0.3	
	77	C <sub>12</sub> H <sub>10</sub> <sup>++</sup> /C <sub>6</sub> H <sub>5</sub> <sup>+</sup>	26.8 ± 0.3	
	77.5	C <sub>11</sub> <sup>13</sup> CH <sub>10</sub> <sup>++</sup>	27.4 ± 0.3	
	78	C <sub>6</sub> H <sub>6</sub> <sup>+</sup>	26.2 ± 0.6	
7	84.5	C <sub>14</sub> H <sup>++</sup>	58.1 ± 1.7	
	85	C <sub>7</sub> H <sup>+</sup> /C <sub>14</sub> H <sub>2</sub> <sup>++</sup>	30.0 ± 1.2	44.8 ± 1.2
	85.5	C <sub>14</sub> H <sub>3</sub> <sup>++</sup>	47.6 ± 1.5	
	86	C <sub>7</sub> H <sub>2</sub> <sup>+</sup> /C <sub>14</sub> H <sub>4</sub> <sup>++</sup>	30.1 ± 0.8	35.3 ± 0.8
	86.5	C <sub>14</sub> H <sub>5</sub> <sup>++</sup>	47.2 ± 1.0	
	87	C <sub>7</sub> H <sub>3</sub> <sup>+</sup> /C <sub>14</sub> H <sub>6</sub> <sup>++</sup>	26.2 ± 0.7	32.3 ± 0.6
	87.5	C <sub>14</sub> H <sub>7</sub> <sup>++</sup>	36.8 ± 0.7	
	88	C <sub>7</sub> H <sub>4</sub> <sup>+</sup> /C <sub>14</sub> H <sub>8</sub> <sup>++</sup>	27.9 ± 1.0	30.9 ± 0.7
	88.5	C <sub>14</sub> H <sub>9</sub> <sup>++</sup>	28.7 ± 0.7	35.3 ± 0.6
	89	C <sub>14</sub> H <sub>10</sub> <sup>++</sup> /C <sub>7</sub> H <sub>5</sub> <sup>+</sup>	20.2 ± 0.7	23.6 ± 0.6
89.5	C <sub>13</sub> <sup>13</sup> CH <sub>10</sub> <sup>++</sup>	21.1 ± 0.5	24.3 ± 0.6	
90	C <sub>7</sub> H <sub>6</sub> <sup>+</sup>	24.9 ± 0.4		
8	97	C <sub>8</sub> H <sup>+</sup>	46.9 ± 1.0	
	98	C <sub>8</sub> H <sub>2</sub> <sup>+</sup>	29.9 ± 0.7	
	99	C <sub>8</sub> H <sub>3</sub> <sup>+</sup>	27.4 ± 0.6	
	100	C <sub>8</sub> H <sub>4</sub> <sup>+</sup>	29.8 ± 0.7	
	101	C <sub>8</sub> H <sub>5</sub> <sup>+</sup>	26.4 ± 0.6	
	102	C <sub>8</sub> H <sub>6</sub> <sup>+</sup>	22.9 ± 0.3	
	103	C <sub>8</sub> H <sub>7</sub> <sup>+</sup>	22.0 ± 0.5	

*(continued...)*

**Table 1.** (*continued...*)

Group	m/q (u)	Assignment	Appearance energy (eV)	Second onset (eV)
9	109	C <sub>9</sub> H <sup>+</sup>	47.9 ± 0.8	
	110	C <sub>9</sub> H <sub>2</sub> <sup>+</sup>	34.8 ± 0.6	
	111	C <sub>9</sub> H <sub>3</sub> <sup>+</sup>	33.3 ± 0.6	
	112	C <sub>9</sub> H <sub>4</sub> <sup>+</sup>	30.8 ± 0.8	
	113	C <sub>9</sub> H <sub>5</sub> <sup>+</sup>	24.3 ± 0.3	
	114	C <sub>9</sub> H <sub>6</sub> <sup>+</sup>	24.5 ± 0.5	
	115	C <sub>9</sub> H <sub>7</sub> <sup>+</sup>	20.4 ± 0.2	
	116	C <sub>9</sub> H <sub>8</sub> <sup>+</sup>	21.3 ± 0.6	
10	120	C <sub>10</sub> <sup>+</sup>	56.3 ± 0.6	
	121	C <sub>10</sub> H <sup>+</sup>	48.4 ± 0.6	
	122	C <sub>10</sub> H <sub>2</sub> <sup>+</sup>	40.1 ± 0.7	
	123	C <sub>10</sub> H <sub>3</sub> <sup>+</sup>	31.0 ± 0.7	
	124	C <sub>10</sub> H <sub>4</sub> <sup>+</sup>	32.1 ± 0.6	
	125	C <sub>10</sub> H <sub>5</sub> <sup>+</sup>	25.1 ± 0.5	
	126	C <sub>10</sub> H <sub>6</sub> <sup>+</sup>	23.2 ± 0.2	26.3 ± 0.4
	127	C <sub>10</sub> H <sub>7</sub> <sup>+</sup>	22.1 ± 0.3	
	128	C <sub>10</sub> H <sub>8</sub> <sup>+</sup>	18.4 ± 0.3	
	129	C <sub>10</sub> H <sub>9</sub> <sup>+</sup>	17.7 ± 0.5	
11	133	C <sub>11</sub> H <sup>+</sup>	52.2 ± 1.4	
	134	C <sub>11</sub> H <sub>2</sub> <sup>+</sup>	39.9 ± 0.7	
	135	C <sub>11</sub> H <sub>3</sub> <sup>+</sup>	40.6 ± 0.9	
	136	C <sub>11</sub> H <sub>4</sub> <sup>+</sup>	(44 ± 4)	
	137	C <sub>11</sub> H <sub>5</sub> <sup>+</sup>	25.3 ± 0.4	
	138	C <sub>11</sub> H <sub>6</sub> <sup>+</sup>	24.3 ± 0.3	
	139	C <sub>11</sub> H <sub>7</sub> <sup>+</sup>	17.8 ± 0.4	
	140	C <sub>11</sub> H <sub>8</sub> <sup>+</sup>	20.1 ± 0.3	
12	149	C <sub>12</sub> H <sub>5</sub> <sup>+</sup>	27.2 ± 0.6	
	150	C <sub>12</sub> H <sub>6</sub> <sup>+</sup>	23.0 ± 0.2	
	151	C <sub>12</sub> H <sub>7</sub> <sup>+</sup>	18.6 ± 0.2	
	152	C <sub>12</sub> H <sub>8</sub> <sup>+</sup>	17.0 ± 0.2	
	153	C <sub>12</sub> H <sub>9</sub> <sup>+</sup>	16.9 ± 0.2	
	154	C <sub>12</sub> H <sub>10</sub> <sup>+</sup>	15.5 ± 0.2	
	155	C <sub>11</sub> <sup>13</sup> CH <sub>10</sub> <sup>+</sup>	16.4 ± 0.2	
13	161	C <sub>13</sub> H <sub>5</sub> <sup>+</sup>	16.9 ± 1.0	
	162	C <sub>13</sub> H <sub>6</sub> <sup>+</sup>	16.8 ± 0.5	
	163	C <sub>13</sub> H <sub>7</sub> <sup>+</sup>	15.3 ± 0.6	
	164	C <sub>13</sub> H <sub>8</sub> <sup>+</sup>	17.0 ± 0.9	
	165	C <sub>13</sub> H <sub>9</sub> <sup>+</sup>	16.0 ± 0.3	
14	174	C <sub>14</sub> H <sub>6</sub> <sup>+</sup>	28.2 ± 0.4	
	175	C <sub>14</sub> H <sub>7</sub> <sup>+</sup>	25.7 ± 0.5	
	176	C <sub>14</sub> H <sub>8</sub> <sup>+</sup>	17.3 ± 0.3	
	177	C <sub>14</sub> H <sub>9</sub> <sup>+</sup>	16.5 ± 0.4	
	178	C <sub>14</sub> H <sub>10</sub> <sup>+</sup>	7.4 ± 0.2	
	179	C <sub>13</sub> <sup>13</sup> CH <sub>10</sub> <sup>+</sup>	7.3 ± 0.4	
	180	C <sub>12</sub> <sup>13</sup> C <sub>2</sub> H <sub>10</sub> <sup>+</sup>	9.2 ± 0.3	

directly from the Levenberg–Marquardt algorithm used for the fitting of the onset function; the uncertainty in the calibration of the incident electron energy is not included in these errors.

The energy intervals used in the fitting range from about 10 eV to about 30 eV, in each case depending on the range of upward curvature of the ion yield curve. Figure 4

shows the fitted onset functions for six anthracene fragments that are relevant for the discussion in Section 4.3.

The appearance energy of the parent ion at 178 u is  $7.4 \pm 0.2$  eV, in good agreement with earlier results [18, 19, 36–38, 45].

The appearance energies of 89 u and of 89.5 u are  $20.2 \pm 0.7$  eV and  $21.1 \pm 0.5$  eV, respectively. Taking

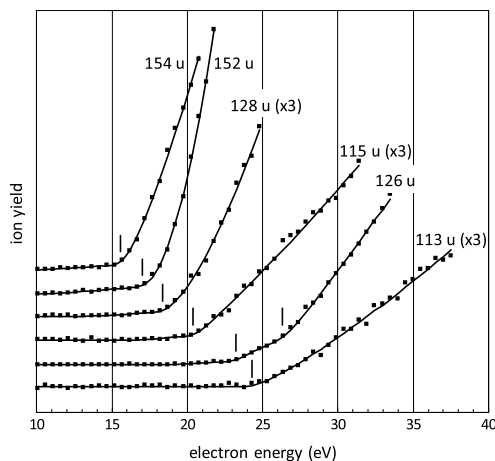


**Fig. 4.** Ion yield curves for six anthracene fragments. The locations of the appearance energies, the second onset for 126 u, and the fitted onset functions are also shown.

the weighted average, the double-ionization energy for anthracene is determined to be  $20.8 \pm 0.4$  eV. Table 2 shows that this value compares well with several other determinations, but the photon impact values and the density functional theory (DFT) calculation are significantly lower. This has been noted and commented on earlier by Tobita et al. [18]. The 89 u and 89.5 u ion yield curves both have a second onset, at  $23.6 \pm 0.6$  eV and  $24.3 \pm 0.6$  eV, respectively, indicating the existence of a second fragmentation process with an onset at  $24.0 \pm 0.4$  eV.

Directly to the left of the 60 u peak in group 5 is a small but distinct peak at 59.33 u. This is attributed to the triply-charged parent molecule. Figure 5 shows a small part of the mass spectrum, the ion yield curve, and the fitted onset function for the triply-charged parent. The appearance energy is  $45.5 \pm 0.5$  eV. This is the first direct determination of the triple ionization energy. Our value is significantly higher than the measurement of 38.2 eV by Kingston et al. [13], see Table 2, who determined the double and triple ionization energies from energy defects in the charge stripping reactions of multiply-charged parent ions in  $N_2$  gas. Our value is also much higher than the DFT value from Holm et al. [38].

Table 3 compares the appearance energies for six fragments obtained by H,  $H_2$ ,  $C_2H_2$ ,  $C_2H_3$ ,  $C_3H_3$  and  $C_4H_2$  losses. Our values are systematically higher than those of Ling and Lifshitz [21], but reasonable agreement is obtained with the values for Jochims et al. [19]. The values for 177 u and 176 u show that H loss and  $H_2$  loss require substantial amounts of energy, and this has also been observed for other small PAHs [46,47]. Notably, the appearance energies for 177 u and 176 u are very similar, and are  $16.5 \pm 0.4$  eV and  $17.3 \pm 0.3$  eV, respectively.

The 175 u and 174 u fragments have very low yields, and have appearance energies of  $25.7 \pm 0.5$  eV and

$28.2 \pm 0.4$  eV, respectively (see Tab. 1), showing that the loss of three and four hydrogen atoms requires even more energy. The appearance energies for 177 u to 174 u indicate a pairing effect, and suggest that 176 u is formed by  $H_2$  loss, 175 u is formed by  $H_2 + H$  loss, and 174 u is formed by  $H_2 + H_2$  loss. This may be of interest in relation to the contribution of PAHs to the formation of cosmic  $H_2$  [2].

In general, the appearance energies for the fragments in groups 8–13 are progressively higher for smaller groups, and within each group appearance energies tend to be higher for fragments with fewer hydrogen atoms. This indicates that at higher electron impact energies excess excitation energy is lost by the release of additional hydrogen atoms. In the groups 9, 10 and 12 the lowest appearance energies are observed for 115 u ( $C_5H_3$  loss), 128 u ( $C_4H_2$  loss) and 154 u ( $C_2$  loss), indicating that transfer of one or two hydrogens atoms during the fragmentation is energetically favorable. This is discussed in more detail in Section 4.3. Between 15 and 20 eV, several of the fragments in groups 10–13 have appearance energies below the double ionization energy, showing that these fragments are produced by singly-charged anthracene.

With the exception of 89 u and 89.5 u, in groups 4–7 all appearance energies are 24.9 eV or higher, well above the double ionization energy of anthracene. Within each group appearance energies tend to be higher for fragments with fewer hydrogen atoms. This raises the question to what extent the ions in these groups originate from double ionization of anthracene (see discussion in Sect. 4.4).

Assuming that the 89 u, 88 u, 76 u and 75 u fragments in our mass spectra are largely due to doubly charged ions, we can compare our appearance energies with those obtained by Mathur et al. [16] from doubly-charged ion mass spectrometry. Table 4 lists the values. There is some similarity in the values for three of the ions, but the appearance energy for  $C_{14}H_8^{2+}$  from [16] is surprisingly low given the large difference in appearance energy between 178 u and 176 u.

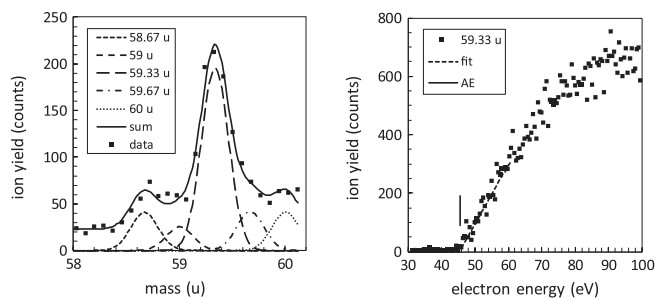
In groups 1–3 the fragments with the highest yields at 100 eV are 39 u, 38 u, 27 u, 26 u, 37 u, and 15 u. These fragments have been identified as singly-charged products of charge separation processes in multiply charged ions [13,17,30]. All these fragments are appearing as broadened peaks in our mass spectra at energies above about 35 eV. At 100 eV, the sum of the yields of all ions in groups 1–3 is only 6.6% of the total ion yield.

The appearance energy for 39 u is  $21.0 \pm 1.0$  eV, which is equal to the double ionization energy of anthracene. A second onset is observed at  $29.4 \pm 1.3$  eV. Possibly the first onset at 21.0 eV is due to fragmentation of singly-charged anthracene, whereas the second onset is due to fragmentation of doubly-charged anthracene. The appearance energies for the other ions in group 3 are much higher.

The appearance energies for 26 u and 27 u in group 2 are higher than for most other fragments. The fragments in group 1 have very low yields; we only obtained an appearance energy for 15 u at  $17.7 \pm 3.2$  eV.

**Table 2.** Comparison of double and triple ionization energies.

Reference	Method	Double ionization	Triple ionization
Present work	Electron impact	$20.8 \pm 0.4$ eV	$45.5 \pm 0.5$ eV
Wacks and Dibeler [10]	Electron impact	$21.1 \pm 0.5$	
Kingston et al. [13]	Mass spectrometry <sup>1</sup>	21.2	38.2
Mathur et al. [16]	Electron impact	$21.1 \pm 0.5$	
Tobita et al. [18]	Electron impact <sup>2</sup>	$21.1 \pm 0.2$	
Hartman et al. [26]	Photon impact	$20.07 \pm 0.17$	
Tobita et al. [18]	Photon impact <sup>2</sup>	$19.6 \pm 0.2$	
Wacks and Dibeler [10]	Group equiv. method	20.4	
Holm et al. [38]	DFT calculation <sup>3</sup>	19.04	36.22

<sup>1</sup> Values obtained from Table 4.<sup>2</sup> On anthracene-d10.<sup>3</sup> Vertical ionization energies obtained from Table 2.**Fig. 5.** Left: 58–60 u mass spectrum at 100 eV, showing a fit with third-integer peaks. Right: ion yield curve for 59.33 u and determination of the appearance energy at  $AE = 45.5 \pm 0.5$  eV.**Table 3.** Comparison of appearance energies of singly-ionized fragments.

Ion	$m/q$	Present work Electron impact	Jochims et al. [19] Synchr. rad. <sup>1</sup>	Ling and Lifshitz [21] UV photo ion <sup>2</sup>	Holm et al. [38] DFT calculation <sup>3</sup>
$C_{10}H_8^+$	128 u	$18.4 \pm 0.3$ eV		$15.4 \pm 0.2$ eV	
$C_{11}H_7^+$	139	$17.8 \pm 0.4$		$14.8 \pm 0.3$	
$C_{12}H_7^+$	151	$18.6 \pm 0.2$		$17.4 \pm 0.2$	
$C_{12}H_8^+$	152	$17.0 \pm 0.2$	$16.00 \pm 0.15$ eV	$15.2 \pm 0.2$	10.44 eV
$C_{14}H_8^+$	176	$17.3 \pm 0.3$	$17.31 \pm 0.10$	$15.8 \pm 0.2$	
$C_{14}H_9^+$	177	$16.5 \pm 0.4$	$15.79 \pm 0.10$	$15.0 \pm 0.2$	12.44

<sup>1</sup> On anthracene-d10.<sup>2</sup> Values from Table 1, for 24  $\mu$ s ion trap storage time.<sup>3</sup> Values obtained from Tables 2 and 5.

### 4.3 Groups 8–13: evidence for hydrogen rearrangements

#### 4.3.1 Groups 11 and 13

The peaks in group 13 have low yields and appearance energies around 16 eV. The most abundant fragment is 163 u, with an appearance energy of  $15.3 \pm 0.6$  eV, attributed to  $CH_3$  loss. 165 u ( $CH$  loss) has a slightly higher appearance energy of  $16.0 \pm 0.3$  eV, and a lower ion yield compared to 163 u, indicating that  $CH_3$  loss is favoured to  $CH$  loss.

Kingston et al. [13] have proposed several reaction schemes for the formation of charge separation products from doubly-charged anthracene. Their Scheme 3 involves

the opening of one of the terminal rings resulting in a side chain with three carbon atoms. Migration of two hydrogen atoms to the end of the side chain is then followed by charge separation producing  $C_{13}H_7^+ + CH_3^+$ . A similar mechanism may well be responsible for the fragmentation  $C_{13}H_7^+ + CH_3$ . In our mass spectra the 15 u fragment ( $CH_3^+$ ) has a very low yield with an appearance energy of  $17.7 \pm 3.2$  eV, indicating that the same fragmentation with charge localization on the smaller fragment may also be a possibility.

The most abundant fragment in group 11 is 139 u, with an appearance energy of  $17.8 \pm 0.4$  eV. This fragment is attributed to  $C_3H_3$  loss by the breaking of two C–C bonds. Scheme 4 of Kingston et al. [13] involving the opening of a terminal ring, the rearrangement of end three carbon

**Table 4.** Comparison of appearance energies of doubly-ionized fragments.

Ion	$m/q$	Present work	Mathur et al. [16]
$C_{12}H_6^{++}$	75 u	$29.1 \pm 0.5$ eV	$31.8 \pm 0.5$ eV
$C_{12}H_8^{++}$	76	$27.2 \pm 1.2$	$29.9 \pm 0.5$
$C_{14}H_8^{++}$	88	$27.9 \pm 1.0$	$21.2 \pm 0.5$
$C_{14}H_{10}^{++}$	89	$20.2 \pm 0.7$	$21.1 \pm 0.5$

atoms, and the formation of cyclopropenyl may well apply here.

The other fragments in group 11 have low yields and higher appearance energies. The lowest mass fragment in this group is 132 u, attributed to  $C_{11}^+$ . Noticeably, the peak at 136 u is almost absent, indicating that  $C_3H_3 + 3H$  loss is unlikely.

#### 4.3.2 Groups 8, 9, 10 and 12

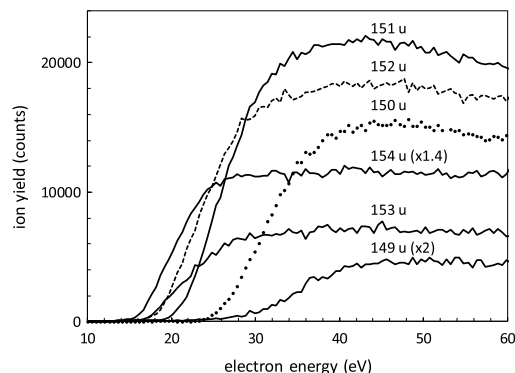
If one would assume that the most abundant fragment in group 12 would be formed by the breakage of two C–C bonds in one of the terminal rings, one would expect that 152 u ( $C_{12}H_8^+$  formed by  $C_2H_2$  loss) would have the highest yield and the lowest appearance energy. At higher electron energies 152 u and 151 u are the fragments with the highest abundance in this group, but 154 u has the lowest appearance energy of  $15.5 \pm 0.2$  eV, indicating that the transfer of two hydrogen atoms during the fragmentation resulting in  $C_2$  loss is energetically favorable at low electron energies.

The fitted onset functions for 154 u and 152 u are shown in Figure 4. Ion yield curves for the ions in group 12 are shown in Figure 6, clearly showing that between 16 and 24 eV,  $C_2$  loss is the most likely fragmentation. The ratio 155 u/154 u is approximately equal to the isotope ratio 179 u/178 u, and 155 u is attributed to  $C_2$  loss from the anthracene isotope.  $C_2H_2$  loss is a prominent fragmentation of naphthalene, but  $C_2$  loss has not been reported [10,47].

A mechanism similar to Scheme 2 of Kingston et al. [13] may be responsible for  $C_2H_2$  loss with the formation of 152 u. This involves the opening of a terminal ring with a side chain containing four carbon atoms, followed by breakage of the C–C bond in the centre of the side chain, yielding singly-charged 2-ethynynaphthalene. Possibly hydrogen migration from the side chain towards the main fragment could then explain the formation of 154 u with  $C_2$  loss.

Johansson et al. [33] have performed DFT calculations for the loss of  $C_2H_2$  from singly-charged anthracene, and have identified three fragmentation pathways proceeding via several intermediate configurations. One of these pathways yields singly-charged 2-ethynynaphthalene. Reitsma et al. [32] show the result of a DFT calculation for the loss of  $C_2H_2$  from doubly-charged anthracene, where  $C_2H_2$  emission occurs after isomerization to benz[a]azulene.

In group 10, one would expect that 126 u ( $C_{10}H_6^+$  formed by  $C_4H_4$  loss from one of the terminal rings at an

**Fig. 6.** Ion yield curves for the fragments of group 12.  $C_{12}H_{10}^+$  (154 u) has a lower appearance energy than  $C_{12}H_8^+$  (152 u),  $C_2$  loss is more likely than  $C_2H_2$  loss.

appearance energy of  $23.2 \pm 0.2$  eV) would have the highest yield and the lowest appearance energy. This is indeed the fragment with the highest abundance at higher electron energies, but 128 u has an appearance energy that is 4.8 eV lower ( $18.4 \pm 0.3$  eV), indicating that the transfer of two hydrogen atoms during the fragmentation is energetically favorable at low electron energies. The ion yield curves are shown in Figure 7. 127 u has an appearance energy at  $22.1 \pm 0.3$  eV, slightly lower than 126 u. 129 u, with an appearance energy at  $17.7 \pm 0.5$  eV, is attributed to  $C_4H_2$  loss from the anthracene isotope. We note that in the mass spectrum of phenanthrene at 21.21 eV photon energy 128 u is present, but 126 u is absent (Fig. 2 in [21]).

Jochims et al. [47] have proposed that  $C_4H_2$  loss from naphthalene proceeds by the formation of a biradical form of  $C_{10}H_8^+$  followed by fragmentation into the benzene cation and  $C_4H_2$  as diacetylene. Similarly,  $C_4H_2$  loss from anthracene could lead to the formation of the naphthalene cation. This has also been proposed by Ling and Lifshitz [21].

In group 9, the loss of a fragment with 5 carbon atoms requires the breakage of three C–C bonds in both the central ring and one of the terminal rings. Without hydrogen rearrangement,  $C_5H_4$  loss would then be the most likely, producing  $C_9H_6^+$  (114 u). However,  $C_9H_7^+$  (115 u) has a lower appearance energy, and a higher abundance below 40 eV, indicating that the formation of 115 u involves the rearrangement of one hydrogen atom. At higher energies, the 112 u and 114 u fragments have lower abundances than 109, 110, 111, 113 and 115 u. Figure 8 shows the ion yield curves for this group (for clarity the 112 u ion yield curve is not included).

Breakage of two C–C bonds in the central ring could lead to  $C_6H_4$  loss, producing  $C_8H_6^+$  (102 u). This is indeed the fragment with the lowest appearance energy in group 8. At higher energies loss of additional hydrogen atoms become increasingly more likely. 103 u is attributed to  $C_6H_4$  loss from the anthracene isotope.

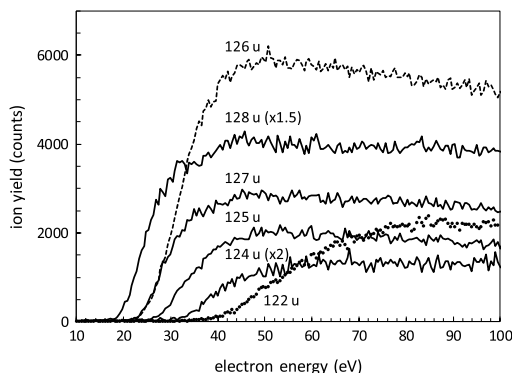


**Fig. 7.** Ion yield curves for the fragments of group 10.  $C_{10}H_8^+$  (128 u) has a lower appearance energy than  $C_{10}H_6^+$  (126 u), indicating that near threshold  $C_4H_2$  loss is more likely than  $C_4H_4$  loss.

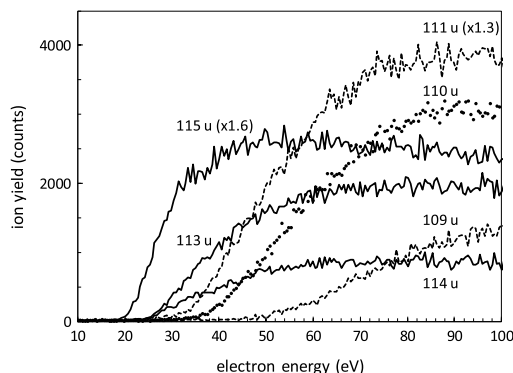


**Fig. 8.** Ion yield curves for the fragments of group 9.  $C_9H_7^+$  (115 u) has a lower appearance energy than  $C_9H_5^+$  (113 u), indicating that near threshold  $C_5H_3$  loss is more likely than  $C_5H_5$  loss.

#### 4.4 Groups 1–7: evidence for multiple ionization

Examining the mass spectra of anthracene at different electron energies clearly shows evidence for multiple ionization. Groups 6 and 7 clearly show evidence for double ionization (see discussion in Sect. 4.1), and good fits were obtained by including half-integer peaks in the modelling of these groups with normalized Gaussians. We have also used half-integer peaks for the fitting of group 5.

Groups 3 and 4 feature broadened peaks of singly-charged fragments or peaks at non-integer masses due to multiply-charged fragments, or a combination of both. We found that good fits were obtained by using third-integer peaks, but these peaks are appearing well below 45.5 eV, so they cannot be due to triply-charged fragments. Groups 3 and 4 are therefore attributed to singly-charged fragments formed with a range of kinetic energies. The ion yield curves for the masses in groups 3 and 4 were obtained by adding the third-integer yields to the yield of the nearest integer peak (for example, the 38.67 u, 39 u and 39.33 u yields were added to obtain the ion yield curve for 39 u).

Groups 1 and 2 only clearly show the presence of peaks at 15 u, 26 u and 27 u. Very small peaks occur at 12 u, 13 u and 25 u. At higher electron energies all these peaks are broadened and there are no indications of half-integer peaks. (Peaks at 14 u and 28 u are due to a remnant of nitrogen in the vacuum chamber.) Ion yield curves for these peaks were determined by summing counts over appropriate bin ranges.

In groups 1–5, with the exception of 15 u and 39 u, all appearance energies are over 5 eV higher than the double ionization energy of anthracene. This raises the question to what extent the masses in these groups are due to doubly-ionized fragments.

Brédy et al. [30] have studied fragmentation of anthracene in collisions with 40 keV  $Ar^{8+}$  ions. They used a coincident detection technique to measure mass spectra of anthracene ions differentiated by the charge  $r$  ( $1 \geq r \geq 4$ ) of the parent ion  $C_{14}H_{10}^{r+}$ . In the mass spectrum for the  $C_{14}H_{10}^{2+}$  parent, the ions in groups 6 and 7

are predominant, but the groups 2–5 have low abundance. In the mass spectrum for the  $C_{14}H_{10}^{3+}$  parent, the peak corresponding to the parent is the largest.

In our mass spectra the triply-charged parent has a very low abundance, indicating that the doubly-charged fragments must be coming mostly from the doubly-charged parent, and that groups 6 and 7 are mostly doubly-charged fragments, but singly-charged fragments contribute to the groups with the smaller masses. Groups 1–4 feature broadened peaks of singly-charged fragments produced in part by charge separation of doubly-charged anthracene. Group 5 may be a mixture of singly- and doubly-charged fragments.

## 5 Conclusions

We have determined the appearance energies for most fragments of anthracene, produced by low-energy electron impact, and this includes the first direct determination of the triple-ionization energy of anthracene.

The appearance energies of 177 u to 174 u are substantially higher than the single ionization energy of anthracene, and indicate a pairing effect suggesting that 176 u is formed by  $H_2$  loss and 174 u is formed by  $H_2 + H_2$  loss.

The groups of fragments containing 8–13 carbon atoms provide evidence for hydrogen rearrangements during the fragmentation. We have found several indications for retention or loss of one or two additional hydrogen atoms. Several of the fragments in groups 10–13 have appearance energies below the double ionization energy of anthracene, and there is no substantial broadening of the peaks at higher electron energies. These fragments are mostly or entirely produced by singly-charged anthracene, but at higher electron energies there may be some contribution from the fragmentation of doubly-charged anthracene.

The groups of fragments with 1–7 carbon atoms provide evidence for multiple ionization. Groups 6 and 7 clearly show the presence of doubly-charged fragments.

Based on the isotope ratio we have concluded that 89 u is almost entirely  $C_{14}H_{10}^{++}$ , and 77 u is mostly  $C_{12}H_{10}^{++}$ . Group 5 is possibly partly attributable to doubly-charged fragments and partly to singly-charged fragments from charge separation reactions of doubly-charged anthracene. Groups 1–4 all show broadened peaks. The high appearance energies and relatively low abundances indicate that these fragments may be partly or mostly due to energetic charge-separation fragmentations of doubly-charged anthracene.

Following the measurements on anthracene, we acquired a full dataset of 200 mass spectra for phenanthrene. Comparison of the mass spectra of phenanthrene and anthracene by stepping through all electron energies does not reveal any clear systematic difference, and we suspect that there are no substantial differences in the electron-induced fragmentation pathways between anthracene and phenanthrene.

The authors wish to acknowledge Mr. David Watson for his contributions to the mechanical design of the apparatus, and to Mr. Pat Seery for his contributions to the electronics equipment.

### Author contribution statement

The measurements were performed by PvdB with help from MD. MG provided essential contributions to the data acquisition. The analysis of the data was done by MD and PvdB. PvdB wrote the paper, and all the authors contributed to the discussion of the results.

### References

- A.G.G.M. Tielens, *Rev. Mod. Phys.* **85**, 1021 (2013)
- S. Cazaux, L. Boschman, N. Rougeau, G. Reitsma, R. Hoekstra, D. Teillet-Billy, S. Morisset, M. Spaans, T. Schlathölter, *Sci. Rep.* **6**, 19835 (2016)
- T. Chen, M. Gatchell, M.H. Stockett, R. Delaunay, A. Domaracka, E.R. Micelotta, A.G.G.M. Tielens, P. Rousseau, L. Adoui, B.A. Huber, H.T. Schmidt, H. Cederquist, H. Zettergren, *J. Chem. Phys.* **142**, 144305 (2015)
- J. Groen, D.W. Deamer, A. Kros, P. Ehrenfreund, *Orig. Life Evol. Biosph.* **42**, 295 (2012)
- A.T. Lawal, *Cogent Environ. Sci.* **3**, 1339841 (2017)
- K.-H. Kim, S.A. Jahan, E. Kabir, R.J.C. Brown, *Environ. Int.* **60**, 71 (2013)
- N.J. Mason, B. Nair, S. Jheeta, E. Szymańska, *Faraday Discuss.* **168**, 235 (2014)
- R. Balog, J. Langer, S. Gohlke, M. Stano, H. Abdoul-Carime, E. Illenberger, *Int. J. Mass Spectr.* **233**, 267 (2004)
- R.M. Thorman, T.P. Ragesh Kumar, D.H. Fairbrother, O. Ingólfsson, J. Beilstein, *Nanotechnology* **6**, 1904 (2015)
- M.E. Wacks, V.H. Dibeler, *J. Chem. Phys.* **31**, 1557 (1959)
- R.C. Dougherty, C.R. Weisenberger, *J. Am. Chem. Soc.* **90**, 23 (1968)
- B. Shushan, R.K. Boyd, *Org. Mass Spectrom.* **15**, 445 (1980)
- R.G. Kingston, M. Guilhaus, A.G. Brenton, J.H. Beynon, *Org. Mass Spectrom.* **20**, 406 (1985)
- H. Kuroda, *Nature* **201**, 1214 (1964)
- K.F. Man, S. Trajmar, J.W. McConkey, J.M. Ratliff, M. Khakoo, *J. Phys. B: At. Mol. Opt. Phys.* **25**, 5245 (1992)
- B.P. Mathur, E.M. Burgess, D.E. Bosfwick, T.F. Moran, *Org. Mass Spectrom.* **16**, 92 (1981)
- D.A. Hagan, J.H.D. Eland, *Rapid Commun. Mass Spectrom.* **5**, 512 (1991)
- S. Tobita, S. Leach, H.W. Jochims, E. Rühl, E. Illenberger, H. Baumgärtel, *Can. J. Phys.* **72**, 1060 (1994)
- H.W. Jochims, E. Rühl, H. Baumgärtel, S. Tobita, S. Leach, *Astrophys. J.* **420**, 307 (1994)
- H.W. Jochims, H. Baumgärtel, S. Leach, *Astrophys. J.* **512**, 500 (1999)
- Y. Ling, Ch. Lifschitz, *J. Phys. Chem. A* **102**, 708 (1998)
- P.M. Mayer, V. Blanchet, Ch. Joblin, *J. Chem. Phys.* **134**, 244312 (2011)
- L. Robson, A.D. Tasker, K.W.D. Ledingham, P. McKenna, T. McCanny, C. Kosmidis, P. Tzallas, D.A. Jaroszynski, D.R. Jones, *Int. J. Mass Spectrom.* **220**, 69 (2002)
- M. Murakami, M. Tanaka, T. Yatsuhashi, N. Nakashima, *J. Chem. Phys.* **126**, 104304 (2007)
- T. Hartman, P.N. Juranić, K. Collins, B. Reilly, N. Appathurai, R. Wehlitz, *Phys. Rev. Lett.* **108**, 023001 (2012)
- T. Hartman, P.N. Juranić, K. Collins, B. Reilly, E. Makoutz, N. Appathurai, R. Wehlitz, *Phys. Rev. A* **87**, 063403 (2013)
- R. Wehlitz, *J. Phys. B: At. Mol. Opt. Phys.* **49**, 222004 (2016)
- M. Gatchell, H. Zettergren, *J. Phys. B: At. Mol. Opt. Phys.* **49**, 162001 (2016)
- J. Postma, S. Bari, R. Hoekstra, A.G.G.M. Tielens, T. Schlathölter, *Astrophys. J.* **708**, 435 (2010)
- R. Brédy, C. Ortéga, M. Ji, J. Bernard, L. Chen, G. Montagne, S. Martin, *Phys. Scr.* **T156**, 014042 (2013)
- S. Martin, L. Chen, R. Brédy, G. Montagne, C. Ortega, T. Schlathölter, G. Reitsma, J. Bernard, *Phys. Rev. A* **85**, 052715 (2012)
- G. Reitsma, H. Zettergren, S. Martin, R. Brédy, L. Chen, J. Bernard, R. Hoekstra, T. Schlathölter, *J. Phys. B: At. Mol. Opt. Phys.* **45**, 215201 (2012)
- H.A.B. Johansson, H. Zettergren, A.I.S. Holm, N. Haag, S. Brøndsted Nielsen, J.A. Wyer, M.-B.S. Kirketerp, K. Støchkel, P. Hvelplund, H.T. Schmidt, H. Cederquist, *J. Chem. Phys.* **135**, 084304 (2011)
- A.I.S. Holm, H. Zettergren, H.A.B. Johansson, F. Seitz, S. Rosén, H.T. Schmidt, A. Lawicki, J. Rangama, P. Rousseau, M. Capron, R. Maisonnny, L. Adoui, A. Méry, B. Manil, B.A. Huber, H. Cederquist, *Phys. Rev. Lett.* **105**, 213401 (2010)
- P. Rousseau, A. Lawicki, A.I.S. Holm, M. Capron, R. Maisonnny, S. Maclot, E. Lattouf, H.A.B. Johansson, F. Seitz, A. Méry, J. Rangama, H. Zettergren, S. Rosén, H.T. Schmidt, J.-Y. Chesnel, A. Domaracka, B. Manil, L. Adoui, H. Cederquist, B.A. Huber, *Nucl. Instrum. Meth. Phys. Res. B* **279**, 140 (2012)
- V.G. Zakrzewski, O. Dolgounitcheva, J.V. Ortiz, *J. Chem. Phys.* **105**, 8748 (1996)

37. A.V. Kukhta, I.N. Kukhta, N.A. Kukhta, O.L. Neyra, E. Meza, J. Phys. B: At. Mol. Opt. Phys. **41**, 205701 (2008)
38. A.I.S. Holm, H.A.B. Johansson, H. Cederquist, H. Zettergren, J. Chem. Phys. **134**, 044301 (2011)
39. A.G. Sanz, M.C. Fuss, F. Blanco, F. Carelli, F. Sebastianelli, F.A. Gianturco, G. García, Appl. Rad. Isotopes **83**, 68 (2014)
40. J. Postma, R. Hoekstra, A.G.G.M. Tielens, T. Schlathölter, Astrophys. J. **783**, 61 (2014)
41. P.J.M. van der Burgt, Eur. Phys. J. D **68**, 135 (2014)
42. P.J.M. van der Burgt, F. Mahon, G. Barrett, M.L. Gradziel, Eur. Phys. J. D **68**, 151 (2014)
43. P.J.M. van der Burgt, S. Finnegan, S. Eden, Eur. Phys. J. D **69**, 173 (2015)
44. Y. Itikawa, N. Mason, J. Phys. Chem. Ref. Data **34**, 1 (2005)
45. NIST Chemistry WebBook table of ionization energy determinations for anthracene, <http://webbook.nist.gov/cgi/inchi?ID=C120127&Mask=20>
46. Y. Gotkis, M. Oleinikova, M. Naor, Ch. Lifshitz, J. Chem. Phys. **97**, 12282 (1993)
47. H.W. Jochims, H. Rasekh, E. Rühl, H. Baumgärtel, S. Leach, Chem. Phys. **168**, 159 (1992)